Experimental and Quantum Calculation Studies of Molecular Systems of Biological and Chemical Importance by Raman, Infrared and SERS

A Thesis
Submitted for the Degree of
DOCTOR OF PHILOSOPHY

by

PARTHA P. KUNDU

CHEMISTRY AND PHYSICS OF MATERIALS UNIT
JAWAHARLAL NEHRU CENTRE FOR ADVANCED SCIENTIFIC RESEARCH
(A Deemed University)
Bangalore – 560 064

MAY 2014

DECLARATION

I hereby declare that the matter embodied in the thesis entitled "**Experimental and Quantum Calculation Studies of Molecular Systems of Biological and Chemical Importance by Raman, Infrared and SERS**" is the result of investigations carried out by me at the Chemistry and Physics of Materials Unit, Jawaharlal Nehru Centre for Advanced Scientific Research, Bangalore, India under the supervision of Prof. Chandrabhas Narayana and it has not been submitted elsewhere for the award of any degree or diploma.

In keeping with the general practice in reporting scientific observations, due acknowledgment has been made whenever the work described is based on the findings of other investigators.

Partha P. Kundu

CERTIFICATE

I hereby certify that the matter embodied in this thesis entitled "**Experimental and Quantum Calculation Studies of Molecular Systems of Biological and Chemical Importance by Raman, Infrared and SERS**" has been carried out by Mr. Partha P. Kundu at the Chemistry and Physics of Materials Unit, Jawaharlal Nehru Centre for Advanced Scientific Research, Bangalore, India under my supervision and it has not been submitted elsewhere for the award of any degree or diploma.

Prof. Chandrabhas Narayana
(Research Supervisor)

Acknowledgments

It is my great pleasure to acknowledge people who have supported, motivated, inspired me during my Ph. D. at JNCASR.

Firstly, I sincerely thank Prof. Chandrabhas Narayana for providing an opportunity to work under his guidance. I thank him for providing me a wide variety of research problems and for being supportive in my research as well as personal life.

I thank Prof. Richard P. Van Duyne, Northwestern University, USA and Dr. Randy Bartel, Colorado State University (CSU), USA for giving me an opportunity to work under their supervision and their hospitality during my stay. I also thank Indo-US Science & Technology Forum (IUSSTF) and CSU for providing financial support during my stay in USA.

I sincerely thank to past and present CPMU chairmen, Prof. C. N. R. Rao, Prof. G. U. Kulkarani and Prof. Balasubramanian for providing all the experimental and computational facilities.

I thank my past and present lab mates, Dr. Nashiour, Dr. Kavitha, Dr. Gopal, Dr. Pavan, Sonia, Srinu, Soumik, Ritu, Dr. Diptikanta, Dr. Navneet, Gayatri, Dhanya, Dr. Santosh, Smitha, Dr. Sorb, Rajaji, Jyothi for their help and fruitful atmosphere in the lab.

I thank Prof. Valakunja Nagaraja, Prof. Tapas K. Kundu, Dr. Sridhar Rajaram, Dr. T. Govindaraju, Tuhin, Swapna, Arjun, Debabrata for fruitful collaboration. I specially thank Tuhin for molecular modeling and Swapna for biological experiments.

I thank Prof. Chandrabhas, Prof. Shobhana, Prof. Narayan, Dr. Vidhyadhiraja, Prof. Chandan Dasgupta and Prof. S. Ranganathan for their wonderful courses.

I thank Vasu, Selvi, Usha and Mr. Arakinathan for various technical help in experiments.

My sincere thank to Academic Section and Administration for all the official help. I also thank Complab for computational and printing facilities. I thank JNCASR family for all the support and care in lab as well as students residence.

I greatly acknowledge Council of Scientific & Industrial Research (CSIR) for research fellowship.

I would like to sincerely thank my teachers Pankaj Mandal (MIT, WB), Pradyut Dutta and Manabesh Bhattacharya (K.N. College, WB) Dr. Asoke Prasun Chattopadhyay and Dr. Chirantan Neogi(Kalyani University, WB) for motivating me towards research.

I thank all my friends at JNCASR for their encouragement and inspiration. I also thank all my friends at Kalyani University, Krishnath College and J N Academy for their love and support.

I feel fortunate to have some radiant companions, for example, Sandipan, Bikram, Kallesh, Subir, Udayan and Tony who were always supportive in my good and bad times.

I thank my family members for their love, blessing and support. I am dedicating this thesis to my parents.

Preface

This thesis presents utilization of vibrational spectroscopy to probe molecules which are of biological and chemical interest. Vibrational spectroscopy can be broadly divided into two techniques infrared (IR) and Raman. These two techniques are complementary as the physical mechanism involved in this process are different. In this thesis Raman is mainly used as this technique has negligible interference from water, which facilitates the study of biomolecules in aqueous medium. However, owing to the inherent weakness of the signal, its use is restricted. Surface enhanced Raman spectroscopy (SERS) can resolve this issue, which blends the advantage of the rich information contained in Raman with much higher sensitivity. We made use of this technique not only for biomolecules, but also for chemical sensors. Raman together with its complementary infrared could provide structural information of a complex form of a catalyst. For band assignments of the spectra we relied on the density functional theory (DFT) calculation whenever computationally feasible. Following is the overview of the thesis:

Chapter 1 provides a thorough introduction about the Raman, IR and SERS phenomenon together with DFT.

Chapter 2 describes the experimental details of the working principles of custom-built Raman microscopy. The method of synthesis of plasmonic nanopaticle for SERS study together with their characterization has been presented. Finally, the computational details have been given.

Chapter 3 demonstrates the use of SERS in probing conformational changes of a protein upon Mg^{2+} binding. The changes in the proteins secondary and tertiary structures were monitored using amide and aliphatic/aromatic side chain vibrations. Changes in these bands suggest the stabilization of the secondary and tertiary structure of transcription activator protein C in the presence of metal ion.

Chapter 4 reports the Raman and SERS studies of two potential drug molecules CTB and CTPB. A comprehensive band assignment based on our DFT calculation has been made. Our study reveals small differences in the interaction of these molecules with the metal surface.

Chapter 5 demonstrates a SERS based method to detect Cu^{2+} ion selectively. First part of the chapter reveals the mode of binding of Cu^{2+} with the Schiff base sensor by utilizing Raman both in the free and metal bound form. Assignments of the bands in the two forms have been made based on DFT calculation. Close match of the spectra of the complex form between the experimental and theoretical calculation provides the first insights of the binding of the metal with the ligand. By employing SERS we could selectively detect Cu^{2+} in the micro molar concentration.

Chapter 6 demonstrates the use of the vibrational spectroscopy (both Raman and IR) to elucidate the role of Na^{+} on the activity of a urea catalyst. The observed changes in the spectra upon complex formation together with the DFT calculation could provide the information about the structural changes occurring in the catalyst upon Na^{+} binding leading to its increased activity.

Publications

1. Raman and surface enhanced Raman spectroscopic studies of specific, small molecule activator of histone acetyltransferase p300, **P. P. Kundu**, G.V. Pavan Kumar, K. Mantelingu, T. K Kundu and C. Narayana, *J. Mol. Struct* **999**, 10 – 15 (2011).

2. Capturing Allosteric Transition Induced by Mg $^{2+}$ion in a Transactivator by SERS , **P. P. Kundu**,T. Bhowmick, G. Swapna, G. V. Pavan Kumar, V. Nagaraja, C. Narayana, *Communicated.*

3. Conformational Change in a Urea Catalyst Induced by Sodium Cation and its Effect on Enantioselectivity of a Friedel-Crafts Reaction, A. K. Chittoory, G. Kumari, S. Mohapatra, **P P. Kundu**, T. K. Maji, C. Narayana and S. Rajaram, *Communicated.*

4. A theoretical investigation of Conformational Change in a Urea Catalyst Induced by Sodium Cation, **P P. Kundu**, G. Kumari, A. K. Chittoory, S. Rajaram and C. Narayana *Manuscript under preperation.*

5. A selective detection of Cu$^{2+}bySERS,$**P. P. Kundu**, D. Maity, T. Govindaraju and C. Narayana *Manuscript under preperation.*

Other miscellaneous publications:

1. Raman based imaging in biological application - a perspective, **P. P. Kundu**, C. Narayana *J. Med. All. Sci.* **2**, 41 – 48 (2012).
2. Physical Characterization of Blood Substitues by Carbon-Fluorine Spectroscopy, F. Menna, B. Menna, **P. P. Kundu**, C. Narayana and O. N. Sharts, *Pharma. Anal. Acta* **4**, 2 (2013).
3. Surface Enhanced Raman Spectroscopy of Aurora Kinases : direct, ultrasensitive detection of autophosphorylation, S. Siddhanta, D. Karthigeyan,**P. P. Kundu**, T. K. Kundu and C. Narayana, *RSC Advances* **3**, 4221 (2013).
4. Dielectric and Raman investigation of structural phase transitions in $(C_2H_5NH_3)2CdCl_4$, R. Yadav, D. Swain, **P. P. Kundu**, H. S. Nair, C. Naryana, S. Elizabeth *Manuscript under preperation.*
5. Glycerol-based Sustainable Solid Base Catalyst for the Transesterification of Vegetable Oils to Biodiesel, B.L.A. P. Devi,K. V. Lakshmi, S. Bhaskar, K.N. Gangadhar,R.B.N. Prasad, P.S. Sai Prasad, B. Jagannadh, **P. P. Kundu**, G. Kumari *Manuscript under preperation.*

Contents

CHAPTER 1

Introduction

Study of interaction of light with matter is a subject of molecular spectroscopy. Theories developed by Maxwell, Young and other scientists in the nineteenth century established that light could be thought as an electromagnetic wave propagating in a medium. Interaction of such wave with molecules can provide rich information about their structure as well as physical and chemical properties. The energy of a fixed molecule can be divided into three parts: electronic, vibrational and rotational. Vibrational spectroscopy probes the vibrational energy levels of a molecule. With the advent of modern optical instrumentation, it has become an indispensable characterization technique in natural science today. Infra-red (IR) and Raman are two main techniques in vibrational spectroscopy. Although both techniques probe the vibrational energy level of a molecule, physical mechanism involved in these processes is different as will be described later. Of these two techniques, mainly Raman spectroscopy is employed in this work. Assignments of vibrational modes of a molecule can be made by comparing with the modes of similar structure. However, since vibrational frequencies are very sensitive to the structure and its environment, and since even the spectrum of a simple molecule contains a large number of closely spaced peaks, for reliable assignments of these modes, calculation of vibrational frequency is necessary. Over almost last three decades, quantum mechanical calculation has become a key to aid in the band assignment. In particular, the development of *Density Functional Theory* (DFT) has made the quantum calculation more powerful as it is computationally less demanding and takes into account the effect of electron correlation.

The primary purpose of the thesis is to explore this versatile technique in molecules of biological and chemical interest. In the last chapter we utilized these two complimentary vibrational techniques to reveal the mechanism of complex formation of a catalyst which triggers its activity. Raman, although a powerful technique, is not suitable for investigations of molecules at low concentration owing to its low sensitivity. Discovery of surface enhanced Raman spectroscopy (SERS) has changed the situation and Raman now finds its application in trace analysis. This is especially important for studying proteins where availability of high concentration of pure sample is scarce. SERS is also useful in studying the adsorption mechanism of molecules on silver surface which can serve as an alternative to the biological interface. We exploited these special characteristics of SERS in our study, details of which will be described in the subsequent chapters. In this work, we carried out detailed vibrational analysis with the aid of DFT for assignments of bands, wherever computationally feasible, to complement the experimental study and have a deeper understanding of vibrations of molecules.

In the rest of this chapter we will present a brief theoretical background of Raman, IR, SERS and DFT necessary to understand the work described later in the thesis. For a profound understanding of these topics, readers are directed to Refs. [1–5] .

1.1 Raman Scattering

When monochromatic radiation of wavenumber $\tilde{\nu}_0$ is incident on a system, most of it will be transmitted unaltered. However, some part of it will be scattered. In the scattered radiation, there will be a wavenumber which is same as the incident wavenumber $\tilde{\nu}_0$. Apart from this, there will be in general, two new wavenumbers of the form $\tilde{\nu}' = \tilde{\nu}_0 \pm \tilde{\nu}_M$. For molecules, $\tilde{\nu}_M$ is found to be in the range characteristics of transitions between rotational, vibrational or electronic levels. The scattering of radiation without any change of wavenumber is known to be Rayleigh scattering, whereas that with the change in wavenumber is called Raman scattering, an effect discovered by C.V.Raman along with K.S. Krishnan in 1928 [6]. Within a short period of time Landsberg and Mandelstam [7] independently confirmed the observation. Earlier in 1923 A. Smekal [8] predicted the effect theoretically, however it took five more years for its experimental realization. Since Raman scattering is a weak phenomenon, lack of sophisticated instrumentation restricted its use to the large quantity of samples in earlier days. However, in recent years the advent of state-of-the-art Raman instrument facilitated to study samples with small quantity, thus improving the scope of Raman spectroscopy. It has found its application in diverse fields such as art and archeology, biosciences, analytical chemistry, solid state physics, liquids and liquid interactions, nano-materials, phase transitions, high-pressure physics and chemistry, pharmaceutical studies, forensic science, etc [9].

1.1.1 Classical theory of Raman effect

According to classical electromagnetic theory, scattering of light can be explained by the radiation generated by the induced electric and magnetic multipoles, which is produced by incident radiation. In most cases, the leading contribution is from electric dipole.

Let us now consider that a molecule is in an oscillating electric field **E**(t) with angular frequency ω_L which in complex notation defined by $\underline{\mathbf{E}}(\omega_L)$ (where **E**(t) = Re($\underline{\mathbf{E}}$ $\times$ $e^{-i\omega_L t}$). The dipole induced by such an electric field can be described by $\underline{\mathbf{p}}(\omega_L)$ (complex notation), where within the linear approximation $\underline{\mathbf{p}}(\omega_L)$is given by,

$$\underline{\mathbf{p}}(\omega_L) = \hat{\alpha}_L(\omega_L) \cdot \underline{\mathbf{E}}(\omega_L) \tag{1.1}$$

oscillating at the same frequency ω_L as the external field $\underline{\mathbf{E}}(\omega_L)$. Here, $\hat{\alpha}_L(\omega_L)$ is called *Rayleigh polarizability tensor* and represents the optical response of the molecule to an external electric field. It is to be noted, $\hat{\alpha}_L(\omega_L)$ is the optical polarizability of the molecule when it is at rest. When we consider the vibration of the molecule, it modulates the linear optical polarizability. This results in beating of frequencies between incident frequency ω_L and vibrational frequency ω_k and which is underlying cause of Raman scattering. If the motion of the atoms about equilibrium position is considered, $\hat{\alpha}_L$ will depend upon ω_L as well as atomic position. We can define this dependence in terms of *normal coordinates*. A specific normal mode *k*, (*k*=1 . . . 3N $-$ 6, where N is the number of atoms of a given molecule) corresponds to a vibrational pattern where all the atoms in a molecule oscillate with the same frequency ω_k. Such oscillations can be described by normal coordinate Q_k, a single scalar that expresses the motion of all atoms oscillating at ω_k and $Q_{k'} = 0$ for all $k \neq k'$ if the molecule exactly vibrate according to a given normal mode *k*. So we can write $\hat{\alpha}_L = \hat{\alpha}_L(\omega_L, Q_1, Q_2, \ldots)$. Now we consider the change in polarizability due to a specific normal mode k with corresponding normal coordinate Q_k, then $Q_{k'} = 0$ for $k' \neq k$. We assume the amplitude of vibration perturbing molecular and electronic structure to be small, and hence the change in polarizability to be minute. Thus we can approximate it by Taylor series expansion:

$$\begin{aligned}\hat{\alpha}_L(\omega_L, Q_k) = \hat{\alpha}_L(\omega_L, 0) + \left(\frac{\partial \hat{\alpha}_L(\omega_L)}{\partial Q_k}\right)_{Q_k=0} Q_k \\ + \frac{1}{2}\left(\frac{\partial^2 \hat{\alpha}_L(\omega_L)}{\partial Q_k^2}\right)_{Q_k=0} Q_k^2 + \dots,\end{aligned} \tag{1.2}$$

Neglecting higher order terms (as Q_k is small), we can write

$$\hat{\alpha}_L(\omega_L, Q_k) = \hat{\alpha}_L(\omega_L, 0) + \hat{R}_k(\omega_L) Q_k \tag{1.3}$$

where

$$\hat{R}_k(\omega_L) = \left(\frac{\partial \hat{\alpha}_L(\omega_L)}{\partial Q_k}\right)_{Q_k=0} \tag{1.4}$$

is called Raman tensor.

For k^{th} normal mode,

$$Q_k(t) = Q_k^0 \cos(\omega_k t + \phi)$$

where Q_k^0 is the amplitude of oscillation and ϕ is an arbitrary phase. Thus induced dipole (real) can be written as

$$\begin{aligned}\mathbf{p}(t) &= Re\left[\hat{\alpha}_L(\omega_L, Q_k)\underline{\mathbf{E}}(\omega_L)e^{-i\omega_L t}\right] \\ &= Re\left[\hat{\alpha}_L(\omega_L, 0)\underline{\mathbf{E}}(\omega_L)e^{-i\omega_L t}\right] + Q_k(t) Re\left[\hat{R}_k(\omega_L)\underline{\mathbf{E}}(\omega_L)e^{-i\omega_L t}\right] \\ &= \mathbf{p}_L(t) + \mathbf{p}_S(t) + \mathbf{p}_{aS}(t)\end{aligned} \tag{1.5}$$

where

$$\mathbf{p}_L(t) = Re\left[\hat{\alpha}_L(\omega_L, 0)\underline{\mathbf{E}}(\omega_L)e^{-i\omega_L t}\right], \tag{1.6}$$

is oscillating induced dipole with frequency ω_L representing Rayleigh scattering,

$$\mathbf{p}_S(t) = \frac{Q_k^0}{2} Re\left[\hat{R}_k(\omega_L)\underline{\mathbf{E}}(\omega_L)e^{-i(\omega_L-\omega_k)t+i\phi}\right] \tag{1.7}$$

which oscillates at $\omega_S = \omega_L - \omega_k$ gives rise to Stokes Raman scattering,

$$\mathbf{p}_{aS}(t) = \frac{Q_k^0}{2} Re\left[\hat{R}_k(\omega_L)\underline{\mathbf{E}}(\omega_L)e^{-i(\omega_L+\omega_k)t-i\phi}\right] \tag{1.8}$$

which oscillates at $\omega_{aS} = \omega_L + \omega_k$ and produces anti-Stokes Raman scattering. From Equation (1.4) we see that if $\hat{\alpha}_L(\omega_L)$ does not depend upon Q_k, $\hat{R}_k(\omega_L) = 0$, the corresponding normal mode will be Raman-inactive. This condition depends upon both the symmetry of the molecule and the vibrational pattern and is termed as *Raman selection rules*. We can define *Raman polarizability tensor* for a specific mode

$$\hat{\alpha}_k(\omega_L) = \frac{Q_k^0}{2}\hat{R}_k(\omega_L) \tag{1.9}$$

which is same for Stokes and anti-Stokes Raman scattering. Thus, classical treatment cannot account for the difference in intensity of Stokes and anti-Stokes Raman scattering as observed experimentally. Also classical theory predicts that there should be no Raman scattering when $Q_k^0 = 0$, i.e., when the molecule is initially in its ground vibrational state, which is the simplest form of Stokes scattering. Also it cannot explain resonant Raman scattering which will be discussed later.

1.1.2 Semi-classical treatment of Raman scattering

In quantum picture, when a system makes transition between different discrete energy levels, radiation is emitted or absorbed. Radiation itself is discrete in nature which occurs through the exchange of photons. Thus, both system and radiation should be treated quantum mechanically to describe the scattering process. However, we can avoid such rigorous treatment and proceed *semi-classically* where the molecular system is described quantum mechanically and radiation is treated as a perturbation to the energy level of the quantum mechanical system.

In quantum mechanical treatment scattering is viewed as transition probabilities between initial state $|i\rangle$ of the system to the final state $|f\rangle$, in the presence of perturbation by electromagnetic radiation of frequency ω_L.

It can be shown [1, 3] that for such a transition, a component of the *Raman polarizability* is given by

$$\alpha_{kl} = \frac{1}{\hbar} \sum_{r \neq i,f} \left\{ \frac{\langle f|\, p_k \,|r\rangle \, \langle r|\, p_l \,|i\rangle}{\omega_r - \omega_i - \omega_L - i\Gamma_r} + \frac{\langle f|\, p_l \,|r\rangle \, \langle r|\, p_k \,|i\rangle}{\omega_r - \omega_f + \omega_L + i\Gamma_r} \right\} \tag{1.10}$$

where the sum is over all possible states $|r\rangle$ of the molecule (except $|i\rangle$ or $|f\rangle$), p_k and p_l are quantum dipole moment operators and Γ_r is inversely proportional to the lifetime of the state $|r\rangle$. It can be seen from the Equation (1.10) that numerators of the Raman polarizability components contain product of the two transition moment term $|r\rangle \leftarrow |i\rangle$ and $|f\rangle \leftarrow |r\rangle$. Therefore, in order that the scattering tensor component to be non-zero, there must exist at least one state $|r\rangle$, for which dipole transition moment is non-zero for both $|r\rangle \leftarrow |i\rangle$ and $|f\rangle \leftarrow |r\rangle$. It should be noted that the states $|r\rangle$ can lie above final state $|f\rangle$, below initial state $|i\rangle$ or in between them. A typical transition (Stokes Raman scattering) is shown in Figure 1.1.

We shall now look into the Equation (1.10) in more detail. The denominators of the expression for transition polarizability components contain terms like $(\omega_{ri} - \omega_L)$,

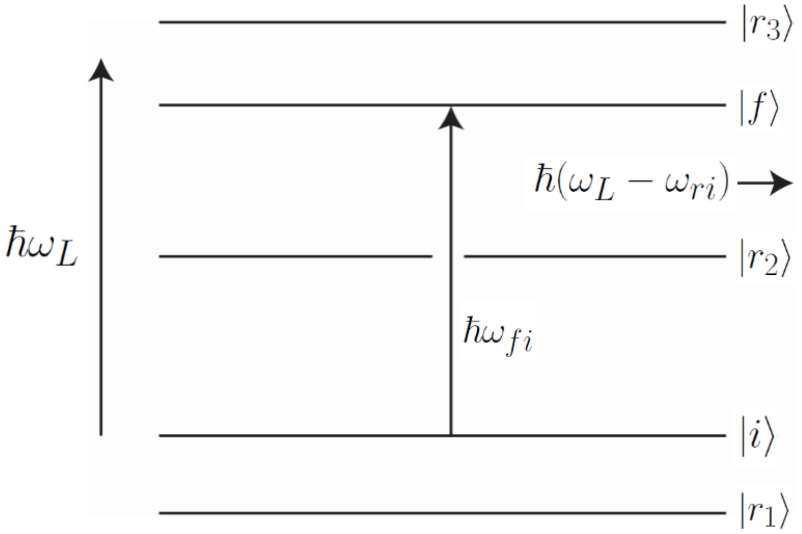

Figure 1.1: Position of states $|r\rangle$ in the energy level diagram for Stokes Raman transition $|f\rangle \leftarrow |i\rangle$

$(\omega_{rf}+\omega_L)$ (where $\omega_{ri} = \omega_r - \omega_i$, $\omega_{rf} = \omega_r - \omega_f$), thus dependent on excitation frequency ω_L. Thus the intensity of radiation will not simply depend on the fourth power of the scattered frequency [1]. When ω_L is much smaller than ω_{ri} or ω_{rf}, scattering intensity follows the fourth power law. In such a case where $\omega_L \ll \omega_{ri}$, the perturbation treatment is depicted by the energy level diagram in Figure 1.2(a). Here, the system is making a transition from initial state $|i\rangle$ to an intermediate *virtual state* (marked as broken line) and afterward to a final state $|f\rangle$. The virtual state is not a stationary state, and it is not a solution of time-independent Schrödinger equation. So the corresponding energy value is not well-defined. In this type of absorption the energy is not conserved and termed as virtual absorption. As ω_L approaches close to the transition frequency, deviation from the fourth power law is seen to arise. This type of scattering process is called pre-resonance Raman scattering and is shown in Figure 1.2(b). Especially when ω_L is

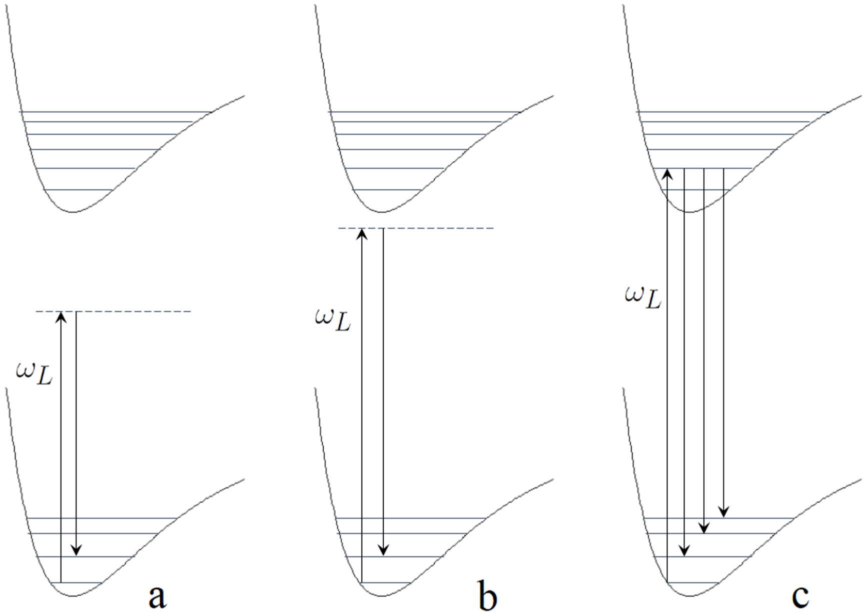

Figure 1.2: Different kind of Raman scattering (a) Normal Raman Scattering ($\omega_L \ll \omega_{ri}$) (b) Pre-resonance Raman scattering ($\omega_L \to \omega_{ri}$), (c) Resonance Raman scattering ($\omega_L \approx \omega_{ri}$)

very close to ω_{ri}, corresponding to the frequency of transition between two real state of the system, the transition polarizability components will be enormously enhanced. This phenomenon is called *resonance Raman scattering* and shown in Figure 1.2(c). This is one of the achievement of the semi-classical treatment which correctly describe the phenomenon. With the use of continuously tunable laser, it is possible to choose a frequency, characteristics of the transition frequency of the system to enhance the signal up to 10^5 times which enables to study samples at very low concentration. In resonance scattering selection rules are different from normal Raman scattering, thus modes which are not Raman active can be observed in resonance Raman scattering. The term Γ_r ensures that at resonance transition polarizability does not become infinity. This arises due to the finite lifetime of the states $|r\rangle$ and Γ_r is related to the broadening of the states $|r\rangle$ [1].

It can be shown [3] that normal vibrational modes can be approximately treated as independent quantum harmonic oscillators. In case of Stokes Raman scattering, the molecule is initially in a state $|\nu\rangle$ and finally in excited state $|\nu+1\rangle$. For anti-Stokes Raman scattering, the process is reversed. For a particular mode k with wavenumber $\bar{\nu}_k$, the classical expression can be generalized to quantum vibration, substituting the classical amplitude of the oscillator $\frac{Q_k^\circ}{2}$ by its quantum counterpart [1, 3]

$$\frac{Q_k^\circ}{2} \rightarrow Q_k^{QM} = \begin{cases} \langle \nu+1| \, Q_k \, |\nu\rangle = (\nu+1)^{\frac{1}{2}} b_k & \text{(Stokes)} \\ \langle \nu| \, Q_k \, |\nu+1\rangle = (\nu)^{\frac{1}{2}} b_k & \text{(anti-Stokes)} \end{cases} \tag{1.11}$$

Here Q_k is *position operator* for the harmonic oscillator and b_k is *zero point amplitude* of the normal vibrational mode and given by

$$b_k = \left(\frac{\hbar}{2\omega_k}\right)^{\frac{1}{2}} = \left(\frac{h}{8\pi^2 c\bar{\nu}_k}\right)^{\frac{1}{2}}$$

Thus quantum mechanics predicts non-zero probability for Stokes Raman transition when the molecule is in its ground vibrational state $|Q_k\rangle$. When a molecule is in equilibrium temperature T, by applying quantum statistical mechanics, it can be shown that for Stokes process, *absolute differential Raman cross-section* at an excitation wavenumber $\bar{\nu}_L$ for normal mode k is given by

$$\frac{d\sigma_k^S}{d\Omega} = C b_k^2 L_M R_k \bar{\nu}_R^4 (1 + n_k^B(T)), \tag{1.12}$$

where $\bar{\nu}_R = \bar{\nu}_L - \bar{\nu}_k$ is the wavenumber of Stokes Raman photon, L_M is the local field correction factor and $n_k^B(T)$ is *Bose factor*. Here R_k is called *Raman activity* which is given by,

$$R_k = 45\bar{\alpha}_k'^2 + 7\bar{\gamma}_k'^2,$$

where $\bar{\alpha}'_k$ and $\bar{\gamma}'_k$ are isotropic and anisotropic invariants of the tensor $\hat{R}_k(\omega_L)$. Similarly for anti-Stokes scattering, the cross-section for k^{th} mode is given by

$$\frac{d\sigma_k^{aS}}{d\Omega} = Cb_k^2 L_M R_k \bar{\nu}_{aS}^4 n_k^B(T). \tag{1.13}$$

Thus comparing Equation (1.12) and (1.13), it can be shown that the ratio between anti-Stokes to Stokes differential Raman cross-section is

$$\rho_k^{aS/S} = \left(\frac{\nu_{aS}}{\nu_S}\right)^4 e^{-\frac{\hbar\omega_k}{k_B T}} \tag{1.14}$$

The exponential term present in the expression provides an explanation for experimental observation of much weaker anti-Stokes Raman spectrum compared to its Stokes counterpart. This expression is also useful to measure the local temperature at the sample in non-contact mode.

We have given an overview of Raman scattering and its explanation from classical and quantum mechanical point of view. As a final note, we will describe about molecular vibration with some more details. Let us now consider a molecule with N atoms. Since the motion of the nucleus is very slow compared to the electronic motion, total Hamiltonian can be split as

$$H_{tot} = H^n + H^{en},$$

where H^n depends only on the nucleus and H^{en} on both nucleus and electrons. If we consider Hamiltonian classically (sufficient to define the concept of normal modes), the kinetic energy of such a molecule due to the nucleus can be written as

$$T^n = \frac{1}{2}\sum_{i=1}^{3N} \dot{q}_i^2, \tag{1.15}$$

where q_i's are called *reduced-mass coordinates*. The potential energy V^n can be expressed in terms of powers of q_i's

$$\begin{aligned} V^n =& V_0^n + \sum_{i=1}^{3N} \left(\frac{\partial V^n}{\partial q_i}\right)_{q_i=0} q_i + \frac{1}{2}\sum_{i,j=1}^{3N} \left(\frac{\partial^2 V^n}{\partial q_i \partial q_j}\right)_{q_i,q_j=0} q_i q_j + \\ & \frac{1}{6}\sum_{i,j,k=1}^{3N} \left(\frac{\partial^3 V^n}{\partial q_i \partial q_j \partial q_k}\right)_{q_i,q_j,q_k=0} q_i q_j q_k + \dots \end{aligned} \tag{1.16}$$

The first term in the expression is just a constant and can be neglected, the second term should be zero at equilibrium. Thus potential energy can be described , in the lowest order of q, by

$$V^n = \frac{1}{2}\sum_{i,j=1}^{3N} f_{i,j} q_i q_j \tag{1.17}$$

where

$$f_{i,j} = \left(\frac{\partial^2 V^n}{\partial q_i \partial q_j}\right)_{q_i,q_j=0}$$

The scalar terms $f_{i,j}$ are called *force constants*, represented as a real symmetric matrix called *Hessian matrix* $\hat{F}$. The dynamics of such system can be written [3] in matrix form

$$\hat{F} \cdot \mathbf{A} = \omega^2 \mathbf{A}$$

where $\mathbf{A} = (\mathrm{A}_i)_{i=1,\dots 3N}$ is a 3N dimensional vector. The eigenvectors (A_k) are called *normal mode* characterized by eigenvalue (ω_k^2), and for a particular mode k, these quantities completely define the dynamics of the system. These 3N normal modes form a *complete* system, so that any arbitrary pattern of the motion of the atoms can be expressed as a combination of more than one frequency. In a molecule, 6 (5 for linear molecule) eigenvectors will have a value zero and represent rotation or translation of the molecule as a whole, rest 3N-6 ((3N-5) for linear molecule) eigenvalue will correspond to the internal deformation of the molecule known as *normal vibrational modes*.

The atomic displacement can also be described by new coordinate Q_k, called *normal coordinates*, defined by

$$q = \sum_{k=1}^{3N} Q_k \mathbf{A}_k \text{ , or } Q_k = \mathbf{A}_k \cdot \mathbf{q}$$

and form orthonormal coordinate system. For a given deformation of a molecule, Q_k represents the contribution of each normal mode. Thus, for a single vibrational mode k, one needs only a single scalar $Q_k(t)$ to express the atomic displacements.

1.2 Infrared (IR) Spectroscopy

IR technique was first used systematically by W. Coblentz [10]. As in the case of Raman spectroscopy, IR spectroscopy involves the interaction of electromagnetic radiation with the system, however the underlying physical mechanism is different. Unlike in the case of Raman spectroscopy, the transition from a state n to m takes place as a result of absorption of a photon, thus the process is mediated through the *electric dipole moment operator* $\hat{\mu}_q$, given by

$$\hat{\mu}_q = \sum_{\alpha} e_\alpha \cdot q_\alpha$$

where e_α is the effective charge on the atom α and q_α is the distance from the center of gravity. It can be shown [11] that the transition probability is given by

$$[\hat{\mu}_q] = \sum_{k=1}^{3N-6} \hat{\mu}_q^k \left\langle \psi_m^* \right| Q_k \left| \psi_n \right\rangle \tag{1.18}$$

where

$$\hat{\mu}_q^k = \left(\frac{\partial \mu_k}{\partial Q_k} \right)_0$$

As can be seen from Equation (1.18) in order that a particular mode k be IR active, both $\hat{\mu}_q^k$ and $\langle \psi_m^* | \, Q_k \, | \psi_n \rangle$ has to be non zero. The first condition requires the change in dipole moment associated with k^{th} normal mode, while the second condition is satisfied only when m and n differ by one.

1.3 Surface Enhanced Raman Scattering (SERS)

The Raman spectrum of a given molecule is distinct and characteristic of that molecule with specificity higher than conventional techniques, such as fluorescence spectroscopy, in terms of the rich information it provides. Thus it can be regarded as 'fingerprint' of the molecule. This distinct feature has been exploited in diverse areas of science and technologies [9, 12–16]. However, the intrinsic low signal from the scatterer hindered its widespread application, especially at lower concentrations of molecules.

Discovery of SERS thus resolves this issue, which takes the advantage of the high specificity of Raman spectroscopy with much higher sensitivity, comparable to or in some cases beating its rival fluorescence [17]. The application of Raman thus has been expanded into the fields which was not possible with traditional Raman. SERS sees its application in the field of analytical chemistry, biochemistry, trace analysis to name a few [18–23]. In addition, SERS quenches background signal from fluorescence molecule through transferring energy to the metal surface, thus making it possible to study those molecules which were problematic otherwise.

The first SERS effect was observed by Fleischmann et al. [24] in 1974. While working with pyridine on the roughened silver electrode, the group observed an anomalously enhanced Raman signal. This phenomenon was attributed to an increase in surface area because of electrode roughening. Later two groups, Jeanmaire and Van Duyne, [25] and Albrecht and Creighton [26] showed that the observed enhancement is too large to be accounted for increased surface area and suggested as a new phenomenon. Since then many related phenomena (e.g. Tip Enhanced Raman Spectroscopy (TERS), Surface Enhanced Infrared Absorption (SEIRA), Surface Enhanced Hyper-Raman Scattering (SEHRS)) have been discovered [2]. Although much research work has been carried out to understand the underlying mechanism of SERS, its origin and extent of enhancement is still debatable. It is accepted that the mechanism can be categorized into two classes, electromagnetic and chemical, with electromagnetic enhancement as a universal and playing the major role, whereas chemical enhancement to act on some analytes adsorbed on the metal surface.

To understand the origin of electromagnetic enhancement one needs some basic concept about plasmon, since plasmon resonance (some specific type) are the leading underlying root of enhancement discussed in SERS.

Plasmons and Plasmonics

The term '*plasmon*' was first coined by Pines in 1956 [27]. A *plasmon* can be described as "a quantum quasi-particle representing the elementary excitations, or modes, of the charge density oscillations in a plasma" [3]. The relationship between plasmon and plasma charge density is similar to photons and the electromagnetic field. When an electromagnetic wave propagates through a medium, it excites the internal degrees of the medium and the energy is shared between the electromagnetic field oscillations and medium's internal excitations. The related quantum particle is called *po-*

lariton. For metals in the visible and infrared region, where optical response is mainly due to interaction of light with the free-electron plasma, these are further classified as *plasmon-polaritons*, which is a specific kind of polariton that refers to charge density wave, associated with an electromagnetic wave. On the other hand, the optical response of a metal depends upon the plasma dynamics. Thus they can be thought of as two sides of the same coin and both can be described by a dielectric function. In case of SERS, '*optical response approach*' is more relevant and in this approach *plasmons* and *plasmon-polaritons* can be regarded as the electromagnetic mode of the system.

In an infinite medium, there exist two kinds of electromagnetic modes. Firstly, transverse electromagnetic mode, which couples the photons with internal excitation of the medium and are called polariton. For these modes there is no net charge density wave. In case of metal, these modes are called *bulk plasmon-polatitons* and arises as a result of interaction with single-electron excitations and has no relation to SERS. In addition, there is a *longitudinal electric wave* associated with the real charge density wave. Since these modes are longitudinal in nature, they cannot couple with transverse electromagnetic wave (photon). For metals these modes are called *bulk plasmons*.

The electromagnetic modes in an infinite medium discussed so far has no consequence in SERS. However in the presence of the interface (usually metal-dielectric), additional modes appear, which is directly relevant to SERS. These modes are called *bound modes* or *surface modes*.

These modes wouldn't exist without the presence of the interface. Theoretically, these modes can exist even in the absence of any incident wave, indicating the infinite optical response. However, this condition is satisfied for complex values of frequency

(ω) or wave-vector (*k*), implying these modes are damped and external source is required to excite and maintain them. For metals, these modes are called *surface plasmon polaritons* (SPPs) and of interest to SERS. SPPs may be propagating (PSPP) or localized (LSPP) depending upon the geometry of the system or frequency.

PSPP exists on a surface where it can be considered as planar over a characteristic length scale (usually the wavelength λ). As mentioned earlier, these modes can sustain only in the presence of external excitation, and a coupling is required between these modes and photon. Since PSPP modes are TM electromagnetic waves, it can be only excited by TM waves, as polarization nature is conserved at planar interface. Further, for PSPP modes be excited, the momentum needs to be matched for both photon and PSPP. As the wave-vector of PSPP is always larger than that of a photon in a dielectric, photon can not directly excite the PSPP modes and missing momentum needs to be imparted by some means [3] to excite the PSPP modes. Once the coupling condition (conservation of momentum and energy) is satisfied, the energy of the incident light is efficiently transferred to the PSPP modes, a phenomenon called *surface plasmon resonance* (SPR). These modes are *non-radiative*. Since the field is strongly confined at the surface and decays exponentially with distance, electromagnetic energy is trapped at the surface and gives rise to a strong local field.

When the size of the metal object is comparable or smaller than the wavelength, the electromagnetic modes will be characterized by discrete values of ω only, and called *localized surface plasmon polaritons* (LSP). For a metallic sphere, using Mie theory, [28, 29] the electromagnetic modes of the sphere can be solved. In addition to the longitudinal and transverse modes, surface modes exist and most important surface mode has the scattered field of electric dipole and therefore correspond to radiative mode. The resonance frequency of the dipolar LSP modes depends on the metal, the environment and also on the size. For non-spherical nano-particle, LSP resonance depends also on the shape. The LSP resonance for these nano-particles can be excited by suitable choice of incident frequency. Since these modes are radiative, the resonance response appears both in absorption and scattering. These resonances are called LSP resonances (LSPR) and depends upon the environment. Similar to the case of PSPP, large local field enhancement results in, both inside and on the surface of the metal, an effect responsible for SERS.

1.3.1 Electromagnetic Enhancement

Now, we are in a position to discuss the electromagnetic (EM) contribution to the SERS effect. EM enhancement is the major contributing factor to the SERS effect and is applied to all analytes, the only requirement is, it needs to be in the vicinity (typically within $\sim$ 10 nm) of the metallic surface.

Here we describe the SERS effect phenomenologically within classical EM theory. As already mentioned, a Raman dipole $\mathbf{p}_R$, excited by a monochromatic light of wavelength ω_L is given by $\mathbf{p}_R = \hat{\alpha}_R \cdot \mathbf{E}_{Inc}$, ($\mathbf{E}_{Inc}$ incident electric field) with oscillation frequency ω_R and the power is proportional to $|\mathbf{p}_R|^2$, which is detected in far-field as a Raman signal. Under SERS condition, the presence of metal surface will affect the process in two ways. Firstly, the EM field at the analyte position is modified (called *local field enhancement*). Moreover, the radiation properties of the Raman dipole ($\mathbf{p}_R$) are modified (known as *radiation enhancement*)

1.3.1.1 Local field enhancement

For metals, when the excitation frequency is close to localized surface plasmon resonance, the electromagnetic field is strongly modified. The *local field* $\mathbf{E}_{Loc}$ generated at the molecular position, has a different magnitude and polarization compared to the incident electric field $\mathbf{E}_{Inc}$. At some positions on the surface, the magnitude of this local field, $|\mathbf{E}_{Loc}|$ is much larger compared to $\mathbf{E}_{Inc}$ and are of interest to SERS. Thus, under SERS condition molecule is in the influence of modified electric field, which induces a Raman dipole $\mathbf{p}_R = \alpha_R \mathbf{E}_{Loc}(\omega_L)$. Since the energy of radiation of the dipole is proportional to $|\mathbf{p}_R|^2$, we can define

$$\mathbf{M}_{Loc}(\omega_L) = \frac{|\mathbf{E}_{Loc}(\omega_L)|^2}{|\mathbf{E}_{Inc}|^2}$$

where $\mathbf{M}_{Loc}(\omega_L)$ is termed as *local field intensity enhancement factor*. This term is correlated with the enhancement of electric field intensity and does not consider any polarization change of the electric field.

1.3.1.2 Radiation enhancement

In the vicinity of metal surface, dipole radiation property changes from that of the free space. The change in dipole emission is due to two reasons:

- Firstly, the radiation in a given direction in the far field per unit solid angle may be modified.
- Secondly, total power radiated by the dipole will be modified from that of the free space. It is to be noted that the emission process does not occur in the same way as that of free space and then gets modified, it is directly influenced by its

environment.

This implies that the energy extracted from an oscillating dipole at a fixed amplitude will be modified by its electromagnetic environment. In some cases, the ratio of power extracted from a dipole near to a metal surface to its free-space counterpart can be a few orders of magnitude, the extra energy is supplied by the excitation source.

Both of these effects depend on geometry and optical property of the substrate, the dipole position, its orientation and the shifted frequency (ω_R) of interest. The effect of these factors is a modification of the radiated power by a factor $M^d_{Rad}(\omega_R)$, which is called *directional radiative enhancement factor* (in the direction of the detector).

1.3.1.3 $|\mathbf{E}|^4$ approximation in SERS enhancements

If only the above mentioned effects are considered SERS EM factor for a single molecule (SM) (single molecule enhancement factor (SMEF)) can be written as

$$SMEF \approx M_{Loc}(\omega_L)M^d_{Rad}(\omega_R)$$

M_{Loc} can be found by solving EM problem under specific condition. Estimating M^d_{Rad} is difficult and it is assumed that $M^d_{Rad}(\omega) \approx M_{Loc}(\omega)$. Then SERS enhancement reduces to

$$SMEF(\omega_L, \omega_R) \approx M_{Loc}(\omega_L)M_{Loc}(\omega_R) \approx \frac{|\mathbf{E}_{Loc}(\omega_L)|^2}{|\mathbf{E}_{Inc}|^2}\frac{|\mathbf{E}_{Loc}(\omega_R)|^2}{|\mathbf{E}_{Inc}|^2}$$

This is known as $|\mathbf{E}|^4$ - approximation. If the Raman shift is small, $\omega_R \approx \omega_L$, then the approximation becomes

$$SMEF(\omega_L) \approx \frac{|\mathbf{E}_{Loc}(\omega_L)|^4}{|\mathbf{E}_{Inc}|^4}$$

1.3.1.4 Surface Selection rule

It can be shown [3] that the single molecule enhancement factor for P-polarized detection is given by

$$SMEF^P = M_{Loc}(\omega_L)\ M_{Loc}^{PW-P}(\omega_R)\ T(\hat{\alpha}_N, \mathbf{e}_{Loc}(\omega_L), \mathbf{e}_{Loc}^{PW-P}(\omega_R)),$$

where

$$T(\hat{\alpha}_N, \mathbf{e}_L, \mathbf{e}_R) = |\mathbf{e}_R \cdot \hat{\alpha}_N \cdot \mathbf{e}_L|^2$$

Here, M_{Loc}^{PW-P} is the radiation enhancement factor obtained for 'virtual' problem with plane-wave excitation coming from the detection direction with polarization along $\mathbf{e}_P$ using optical reciprocity theorem (ORT) [30], $\hat{\alpha}_N$ is the normalized Raman polarizability tensor, $\mathbf{e}_L$ and $\mathbf{e}_R$ are unit vectors denoting the polarization of 'real' local electric field and that of 'virtual' plane wave problem respectively. $T(\hat{\alpha}_N, \mathbf{e}_L, \mathbf{e}_R)$ is called *surface selection rule factor*. It couples the excitation and radiation problems through normalized Raman polarizability tensor. By definition, T is always positive, or may be zero for certain combinations of $\mathbf{e}_L$ and $\mathbf{e}_R$. It can be shown that,

$$0 \le T(\hat{\alpha}_N, \mathbf{e}_L, \mathbf{e}_R) \le \frac{15}{4} \tag{1.19}$$

This inequality shows that in most cases contribution of this factor is not significant. However, in some special cases, the combination of Raman tensor symmetry and the orientation of molecule on the surface may lead this term to to zero. These modes will then be absent from SERS. Moreover, in the intermediate case, this term is responsible for changes in the relative intensity of Raman peaks under SERS condition. Thus, comparing the normal Raman and SERS, adsorption and orientation of a molecule can be studied.

1.3.1.5 Quantitative treatment of a metallic sphere : An example

To end, we will consider a simple example of a metallic sphere to understand LSP resonance more quantitatively. Let us consider a sphere of radius a embedded in an infinite medium of dielectric constant ϵ_M. If the radius of the sphere is small compared to the wavelength of light ($\sim \lambda/20$), one can employ *electrostatic apporoximation* (ESA) [3]. In this approximation, incident field E_{Inc} is considered as a constant. The field outside the surface of sphere is given by,

$$E_{Out} = E_{Inc} + E_{P_M}$$

where E_{P_M} is (electrostatic) field created by the induced dipole P_M at the center of sphere, where

$$P_M = 3\epsilon_0\epsilon_M \frac{\epsilon(\omega) - \epsilon_M}{\epsilon(\omega) + 2\epsilon_M} \tag{1.20}$$

$\epsilon(\omega)$ is dielectric function of the metal, it is complex and can be written as

$$\epsilon(\omega) = \epsilon'(\omega) + i\epsilon''(\omega)$$

When denominator of Equation 1.20 goes to zero, it corresponds to resonance condition. Since $\epsilon''(\omega) \neq 0$, resonance condition is satisfied when $\epsilon'(\omega)$ is equal to $-2\epsilon_M$. Since

ϵ_M is real positive (for non absorbing medium), $\epsilon'(\omega) < 0$. This condition is met for metals at frequency shorter than their bulk plasmon resonance. This type of resonance is called *dipolar localized surface plasmon resonance*. In addition, if the imaginary part of $\epsilon(\omega)$ is small, the resonance will be stronger. For silver $\epsilon''(\omega)$ is comparatively smaller in the resonance region, making it to be the best candidate for SERS application.

Distance dependence

In ESA, the electric field outside a sphere can be considered as a field produced by a dipole at the center of the sphere. Thus if a molecule is at a distance d from the surface from the sphere, the electric field is proportional to $(\frac{1}{a+d})^3$ and SERS EF varies as $(\frac{1}{a+d})^{12}$. Since a is much bigger than d, distance dependence of enhancement is not as dramatic as commonly thought to be. The SERS EF decays by a factor of 10 at a distance $d \approx 0.2a$

1.3.2 The chemical enhancement

Chemical enhancement can be regarded as a modification of the Raman polarizability tensor of the adsorbate due to the formation of complex with metal. The chemical enhancement can be of three types [31, 32]

- First type occurs when the binding of adsorbate is non-covalent. Then metal causes a small change in electronic distribution of the analyte, bringing about change in polarizability, hence Raman activity of the mode.

- Second type occurs when analyte forms a covalent bond with metal either directly or through electrolyte ion. This may result in significant change in the polarizability of the analyte. Polarizability depends upon available optical transitions. Thus the overlapping of molecular orbitals, arising due to complex formation provides a way for the polarizability to be altered. It may also happen that the new electronic state is formed and this state is in resonance or close to resonance with the excitation source, it provides an additional resonance enhancement effect.

- Third type is a special case of second one, which occurs when the difference between the Fermi level (E_F) of metal and HOMO or LUMO of the anlyte equals the laser energy. In such situation, photo-driven charge transfer occurs between HOMO (LUMO) and unoccupied (occupied) states above (below) Fermi level.

1.4 Density Functional Theory

Over past few decades *density functional theory* (DFT) has emerged as an effective tool in quantum chemistry because of its computational cost comparable to that of Hartree-

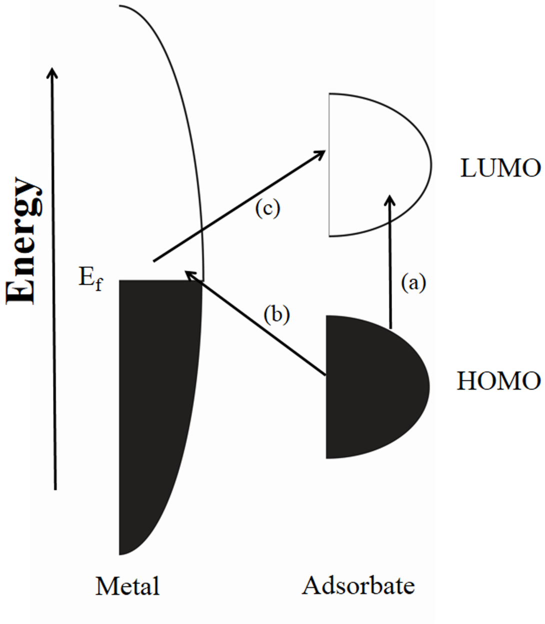

Figure 1.3: Energy level diagram for charge transfer mechanism responsible for resonance enhancement. Excitation energy can be directly in resonance with the electronic energy level of the complex ((a)), or through coupling with metal ((b) + (c)).

Fock (HF) theory, [4] yet the accuracy similar to the computationally demanding post-Hartee-Fock methods [4]. In earlier attempts of formulation of Density functional theory by Thomas [33] and independently by Fermi [34] was in the hope that energy can be written solely in terms of electron density. The first mathematical proof of this idea was given by Hohenberg and Kohn in 1964, [35] stating that the ground state electronic energy of a system is completely determined by electron density ρ. Compared to the wave function approach where the complexity increases exponentially with the number of electrons, the electron density is independent of the size of the system. The aim of the DFT technique is to find the functionals that connect the electron density with the energy. However, such orbital free model suffers from the fact that kinetic energy is poorly described.

1.4.1 The Kohn-Sham approach

The approach as suggested by Kohn and Sham[36] was to divide the kinetic energy into two parts, major contribution which is analogous to HF kinetic energy and can be calculated exactly, and a small contribution due to correlation. In Kohn-Sham theory orbitals are reintroduced, and the kinetic energy, electron-nuclear and coulomb electron-electron energies have the same expression as in HF method, an additional term called *exchange-correlation* appears. The main idea of Kohn-Sham theory is to calculate the kinetic energy by assuming a non-interacting system. In practice, electrons are interacting and the missing kinetic term is absorbed in exchange-correlation. The success of this approach lies in the fact that HF energy produces $\sim 99\ \%$ correct number, thus the remaining kinetic energy is small. Following the Kohn-Sham approach the DFT energy can be written as:

$$E_{DFT}\left[\rho\right] = T_S\left[\rho\right] + E_{ne}\left[\rho\right] + J\left[\rho\right] + E_{xc}\left[\rho\right] \tag{1.21}$$

In Equation 1.21, the first term corresponds to kinetic energy of non-interacting electrons, the second term represents the nuclear-electron attraction, the third term denotes Coulomb electron-electron repulsion and the last term is called the exchange-correlation. E_{xc} can be obtained by equating E_{DFT} with exact energy. Thus E_{xc} can be given by, [4]

$$E_{xc}\left[\rho\right] = \left(T\left[\rho\right] - T_S\left[\rho\right]\right) + \left(E_{ee}\left[\rho\right] - J\left[\rho\right]\right) \tag{1.22}$$

The first parenthesis is kinetic correlation energy whereas the second comprises of both potential correlation and exchange energy.

In Kohn-Sham theory the only approximation to be made is for the exchange-correlation functional. DFT methods differ from one another in the functional form of this exchange-correlation energy. Since its value is much less than the kinetic energy ($\sim$ 10 times smaller), this theory is less sensitive to the inaccuracies in functionals. Kohn-Sham approach is independent particle model, similar to the HF theory, but simpler than many-particle (correlation) wave function methods. After choosing a proper exchange-correlation functional the task is to determine a set of orthogonal orbitals corresponding to the minimum energy. Kohn-Sham equations can be written as

$$\mathbf{h}_{KS}\phi_i = \epsilon_i\phi_i \tag{1.23}$$

where $\mathbf{h}_{KS}$ is one electron operator given by

$$\mathbf{h}_{KS} = -\frac{1}{2}\nabla^2 + \mathbf{V}_{eff} \tag{1.24}$$

$\mathbf{V}_{eff}$ includes the nuclear-electron interaction, the electron-electron repulsion and the exchange-correlation potential and given by,

$$\mathbf{V}_{eff}(\mathbf{r}) = \mathbf{V}_{ne}(\mathbf{r}) + \int \frac{\rho(\mathbf{r}')}{|\mathbf{r} - \mathbf{r}'|} d\mathbf{r}' + \mathbf{V}_{xc}(\mathbf{r}) \tag{1.25}$$

$\mathbf{V}_{xc}$ is derivative of the exchange-correlation energy with respect to the density and is given by,

$$\mathbf{V}_{xc}(\mathbf{r}) = \frac{\delta E_{xc}\left[\rho\right]}{\delta \rho\left[\mathbf{r}\right]} \tag{1.26}$$

Since the second and third term of the Equation 1.25 itself depends upon electron density, the Kohn-Sham equation needs to be solved iteratively. An initial guess of the ground state solution is made. This initial guess defines the density (ρ), which in turn defines V_{eff}. The Kohn-Sham equation is solved with this potential and ground state solution is obtained. Density (ρ) is recalculated using the new solution and compared with the initial value. The process is continued until a convergence is achieved. Solving Kohn-Sham equation numerically is challenging and limited to small systems. In most cases, Kohn-Sham orbitals are expressed in atomic basis set,

$$\phi_i = \sum_{\alpha} c_{\alpha i} \chi_{\alpha} \tag{1.27}$$

Therefore the solution of Kohn-Sham equation corresponds to the determination of coefficient of the basis functions.

1.4.2 Exchange and correlation energy functionals

Exchange-correlation energy E_{xc} is expressed as the sum of two terms, exchange E_x and correlation E_c, where the exchange part has the foremost contribution. The exchange term occurs as a consequence of Pauli's principle which states that no two electrons can have the same state. It can be thought as a quantum correction to the classical Coulomb interaction. Furthermore, electrons try to avoid each other more than as predicted by HF wave function, and corresponds to correlation energy. The exchange term occurs between the electrons of same spin, whereas the correlation term is spin independent. In DFT these are local functionals which depend on the density at a point and its local surroundings. The exchange-correlation functionals are designed in such a way that they cancel at long distance. Another important consideration is electron self-interaction energy, the interaction of an electron on itself, which is unphysical. In DFT this is corrected in the exchange energy part. However, complete self-interaction free functionals is not possible. Although the exchange-correlation potential is unique, its exact functional form is unknown. It should have certain properties which are described elsewhere [37]. Exchange-correlation functionals have some mathematical form containing the unknown parameters. Their values are assigned either by fitting experimental data or the properties they should have as mentioned above. In practice, a blend of these two approaches is adopted. Herein, we will follow " Jacob's ladder" approach as suggested by J.P. Perdew, [38, 39] to systematically describe the functionals, where we can hope that each step up the ladder the accuracy is improved.

1.4.2.1 Local Density Approximation

Local Density Approximation (LDA) is the simplest exchange-correlation functional where the density is treated as a uniform electron gas, or slowly varying function at a given point. For a uniform electron gas, exchange energy is given by Dirac formula [40]

$$E_X^{[LDA]}[\rho] = -C_X \int \rho^{4/3}(\mathbf{r}) d\mathbf{r} \tag{1.28}$$

$$C_X = -\frac{3}{4} \cdot \left(\frac{3}{\pi}\right)^{(1/3)} \tag{1.29}$$

In general, where number of spin-up (α) and spin-down (β) electrons are not equal LDA is replaced by *Local Spin Density Approximation* (LSDA).

$$E_X^{[LSDA]}[\rho] = -2^{(1/3)} C_X \int (\rho_\alpha^{4/3} + \rho_\beta^{4/3}) d\mathbf{r} \tag{1.30}$$

Correlation energy for varying total density is determined by quantum Monte Carlo Methods [41, 42]. In DFT calculation these results have been parametrized by Vosko, Wilk, and Nusair (VWN) [43] and by Perdew and Zunger (PZ) [44] to obtain a functional form of the correlation potential. For molecules, the exchange energy is underestimated and the error surpasses the total correlation energy. The correlation energy is overestimated affecting the bond strength also to be overestimated. Despite its simplicity, it has been used extensively to describe extended systems such as metals, where the approximation of slowly varying density is close to reality.

1.4.2.2 Gradient-corrected methods

In order to describe the molecular system in a better way, non-uniformity in density of electron gas needs to be considered. This is achieved by assuming the exchange and correlation energies depending on both the electron density and derivatives. *Generalized Gradient Approximation* (GGA) includes the first derivative of the density as a variable. As in the case of LDA, GGA is also a local method, where the functionals depend upon the density and its derivative at a particular point. The inclusion of additional variable may seem to be computationally challenging, however it has been shown that Kohn-Sham equations can be solved using LSDA exchange-correlation functional, [45] gradient correction can be included as a perturbation. The gradient corrections to the exchange-correlation are added either to exchange or gradient functionals. Example of some popular GGA exchange functionals are those of Perdew and Wang [46] and Becke (B or B88) [47]. Among GGA functionals for correlation energy Lee, Yang, and Parr correlation functional is a popular one [48].

1.4.2.3 Hybrid methods

It has been seen that the LDA and GGA trend are opposite compared with HF method. This leads to the development of an approximation which combines DFT correlation and a combination of DFT and HF exchange. The general expression for such approximation takes the form:

$$E_{XC}^{hyb} = \alpha E_X^{HF} + (1-\alpha)E_X^{DFT} + E_C^{DFT} \tag{1.31}$$

where α is chosen to be 1/2, or is fitted to some experimental data. An example of such a functional is B3LYP[49, 50] which is defined as:

$$E_{XC}^{B3LYP} = (1-a)E_X^{LSDA} + aE_X^{exact} + b\triangle E_X^{B88} + (1-c)E_C^{LSDA} + cE_C^{LYP} \quad (1.32)$$

The parameters a, b, c are evaluated by fitting experimental data. Here, E_X^{exact} is the *exact exchange* energy similar to the HF theory, the only difference is HF orbitals are replaced by Kohn-Sham orbitals. Addition of exact HF exchange often found to improve better agreement with experiment. The improvement of the result may be attributed to the partial inclusion of the exact exchange, reducing the self-interaction error, as HF theory is void of any self-interaction.

1.4.3 Basis set

Molecular orbitals (MO) are generally expressed in terms of basis set. If the basis set is complete, comprising of infinite functions, it exactly represents the MO. However, for practical consideration one needs to use finite basis set, thus representing MO components along particular coordinate axis corresponding to the selected basis functions. The larger the basis set used, better is the accuracy.

1.4.3.1 Slater and Gaussian type orbitals

Two types of orbitals, Slater Type Orbitals (STO) and Gaussian Type Orbitals (GTO), are commonly used in electronic structure calculations. Although called *Atomic Orbitals* (AO), they are in general not solution to the Schrödinger equation for an atom.

STOs [51] have the functional form as

$$\chi_{\zeta,n,l,m}(r,\theta,\phi) = Y_{l,m}(\theta,\phi)r^{n-1}e^{-\zeta r} \tag{1.33}$$

where N is a normalization constant, $Y_{l,m}$ are spherical harmonics, r, θ and ϕ are spherical coordinates, and ζ is the “orbital exponent”. Although the exponential dependence of the distance between the nucleus and electrons resembles hydrogen atom orbital, STOs do not have any radial node, which is formed by linear combination of STOs. The exponential decay guarantees the rapid convergence with increasing number of functions, however the analytic solution of three- and four-centre two-electron integrals is not possible with STOs. The use of STOs is mainly limited to the atomic and diatomic systems where high accuracy is desired. GTOs [52] can be written in polar coordinates as

$$\chi_{\zeta,n,l,m}(r,\theta,\phi) = Y_{l,m}(\theta,\phi)r^{2n-2-l}e^{-\zeta r^2} \tag{1.34}$$

Since GTOs depend as e^{-r^2}, they have zero slope at the nucleus. Unlike the case of STO which has ”cusp”, the behavior of electrons near the nucleus is poorly described. Furthermore, it falls off too rapidly with the distance from the nucleus, the behavior far away from it is not properly described. These behaviors imply that compared to STOs more GTOs are required to reach the same level of accuracy. However the price paid for considering more GTO functions is compensated by the ease with which the calculations can be performed. The exponent values are usually determined by variational HF calculations on the atoms.

1.4.3.2 Contracted basis set

One of the drawbacks of the above mentioned all energy minimized basis sets is that they mainly concentrate on the energetically important inner-shell electrons. Thus an optimum basis set represents core electrons more perfectly than the valence electrons. But chemically interesting region is the ‘tail’ of the wave function which is energetically less important. Thus to describe this region one needs to use a larger basis set where most of the computational effort will be spent to describe the chemically unimportant core electrons. To overcome this issue *contracted* basis set were introduced. Instead of using a full set of basis function, called *primitive* GTOs (PGTOs), smaller set of functions are generated by combining those PGTOs with the *fixed* linear combination. The new functions are called *contracted* GTOs (CGTOs), and can be written as:

$$\chi(CGTO) = \sum_{i}^{k} a_i \chi_i(PGTO) \tag{1.35}$$

The *degree* of contraction is defined as the number of PGTOs used to construct CGTO. Contraction can be of two types: *segmented* and *general*.In a segmented contraction one primitive enters into only one contracted function, whereas in general contraction all primitives are used in all contracted functions with different constants . Contraction is especially useful for the functions describing the inner-shell as a large number of orbitals are required to describe the behavior of wave function near the nucleus. It is to be mentioned that restricting the number of variational parameters makes the orbitals less flexible and cause the energy to be raised. However, computational cost will also reduce, thus trade-off between level of accuracy and computational cost needs to be decided.

Pople style basis sets

k-nlmG basis sets These *split valence* type basis sets are designed by Pople and coworkers. Here, k is number of PGTOs that are utilized to describe core orbitals, the symbol nlm represents the number of segments the valence orbitals are split into, and also the number of functions in each segment. Basis sets with two values (nl) are called split valence and three values (nlm) are called triple split valence. The values before G (Gaussian) implies that basis set consists of s- and p- functions. Same exponents are used for s- and p- functions in the valence, thus reducing the flexibility of the basis set, while increasing the computational efficiency.

3-21G This is a split valence basis, where core orbitals are three PGTOs contracted function, inner part of the valence orbitals comprises of two PGTOs and the outer part of one PGTO.

6-31G This is a split valence basis where the core orbitals are represented by contraction of 6 PGTOs, inner part of the valence by 3 PGTOs and outer part of the valence is expressed by one PGTO.

6-311G This is a triple split valence basis where core orbitals are represented by six PGTO contracted function, and the valence orbitals are split into three functions, consisting of three, one and one PGTOs respectively.

Polarization [53] and diffuse functions [54] can be added to each of these basis sets. Polarization functions are placed after G, where diffuse functions are positioned before G. Diffuse functions are generally s- or p- functions denoted by + or ++, where + denotes one set of diffuse s- and p- functions added on the heavy atoms and ++ indicates in addition one set of diffuse s-function added to hydrogen atom as well.

1.4.3.3 Effective Core Potential

Systems involving elements in the lower part of the periodic table have a large number of core electrons which is chemically unimportant. However to describe the repulsion between core electrons correctly, large number of basis functions need to be used. Moreover, relativistic effects need to be included for the element in the lower half of the periodic table. This problem may be resolved by modeling the core electrons by appropriate function and considering only the valence electrons. The function that models the core electrons are known as *Effective Core Potential* in the chemical community [55, 56]. To model core electrons, initially good-quality all electron wave function is generated by numerical Hartee-Fock, relativistic Dirac-Hartree-Fock or density functional method. The valence orbitals then are replaced by nodeless pseudo-orbitals in such a way that they match with the all-electron solution in the outer part without any node in the core. Core electrons are replaced by a potential, expressed in terms of expansion of the proper functions of nuclear-electron distance. Relativistic effect can also be incorporated in this potential as the effect is mainly important for core electrons. Finally, the parameters are fitted so that pseudo-orbitals obtained from Schrödinger's (Dirac) equation match all-electron valence orbitals. The Hay-Wadt LANL2DZ [57–59] basis set- relativistic effective core potential (ECP) combination is an example of such method.

1.4.4 Geometry Optimization

The first step of any quantum chemical calculation is the geometry optimization of the molecule. In general, optimization is performed on an isolated molecule, considering non-interacting system in the gas phase. Initial structure is either taken from literature or obtained from *empirical force field model*. Geometry optimization starts with solving the Kohn-Sham equation self-consistently on the initial geometry. Energy and force on the molecule is calculated from the solution. If the force on the molecule is not zero a different geometry is assumed. The process of finding a local minimum in the *potential energy surface* is achieved through the *conjugate gradient* [60] method.

1.4.5 Frequency Calculations

Once the equilibrium atomic positions of the atoms are known, the electronic structure can be calculated on the optimized structure. The interaction of atoms are now known, which enables to calculate force constants. Force constants can be calculated by displacing each atoms from their equilibrium positions and recalculating the total energy of the deformed configuration. By numerical differentiation of the total energy, force constants on each atom can be calculated. This enables to construct Hessian matrix for the vibrational modes as described in Section 1.1.2. The frequency needs to be calculated at the same theoretical model and with same basis set as that used in the optimization procedure.

1.5 Application of vibrational spectroscopy in biology and chemistry

Vibrational spectroscopy has established itself to be a valuable tool for investigation of chemical and biological samples. The application of vibrational spectroscopy in biomolecules has the following advantages [11] (i) it can provide detailed structural and intermolecular interaction information, (ii) it can be applied irrespective of the size of molecule and finally (iii) it can be applied in any state (solid, liquid or gas) of the system, allowing it to probe close to the physiological condition of the system. Although both vibrational spectroscopy can be used to elucidate structural information, many biological systems are active only in the presence of water. For IR this imposes restriction of its use as water exhibits strong peaks in the region of interest[11]. Raman is free from this problem, however it suffers from the intrinsic weak signal. Ultra violet resonance Raman (UVRR) spectroscopy can enhance the signal up to 10^4 times however the high energetic photons used in these experiments may cause damage to the sample. Since in SERS the excitation source used is in the visible region, its energy is much less with enhancement few orders of magnitude more than the UVRR. Thus SERS has become an indispensable tool in biology [61–64]. Although SERS has established as an ultra sensitive technique, its use in protein is limited to the detection and characterization rather than probing structural changes. Only few attempts have been made in this direction [65–67]. In chapter 3 we have demonstrated that SERS can be used as a tool to probe protein's conformational changes both at the secondary and tertiary level for the first time. SERS also has a special property by virtue of selection rule to study the adsorption mechanism on metal surface. Several authors have investigated

SERS of pharmaceuticals to understand the adsorption process on metal surface [68]. Drug molecules interact with human organ on special center. It has been shown [69] that gold or silver metal surface can mimic biological interface. Also it is important to know whether the structure of the adsorbed molecule has undergone any change or not. In chapter 4 we have studied two molecules which interact with a well known protein p300. By comparing the spectra of normal Raman and SERS we could elucidate their interaction with the metal surface. Even though SERS has been utilized to detect analytes at a single molecular level [70–72], study of inorganic atomic ions are scarce as it is a molecular spectroscopy which can not probe single atom. Only recently several methods have been developed to detect atomic ions indirectly [73]. In chapter 5 we have developed a method to detect Cu^{2+} ion at very low concentration by utilizing SERS. In last chapter, we exploited another property of vibrational spectroscopy. Recently, a urea based catalyst was synthesized [74] whose activity was shown to increase in the presence of a weak Lewis acid. The mechanism of such enhancement in its activity could not be elucidated by X-ray crystallography as the complex could not be crystallized. Since vibrational spectroscopy does not require a sample to be in crystal form, we probed the catalyst in its free and complex form by IR and Raman spectroscopy. Applying both vibrational techniques, we could reveal the possible role of the Lewis acid in the catalytic activity which is further supported by our DFT calculations.

CHAPTER 2

Methods

In this chapter we will describe the details of the experimental and simulation methods used in the thesis namely Raman setup, synthesis of silver nano-particle used for SERS, sample preparation for infrared spectroscopy and quantum chemical calculation used to simulate and interpret the vibrational spectra.

2.1 Raman Spectrometer

Raman scattering being inherently weak, effective suppression of elastically scattered light and collection of inelastic light is prerequisite in every Raman spectrometer. Ever since Raman effect was discovered [6], the use of lasers as excitation source, grating monochromator, charge-coupled devices (CCDs) as detectors have made Raman spectroscopy a potent tool to study different materials including biomolecules [75–85]. Despite the fact that commercial Raman microscopes assumed a key part in the success of Raman spectroscopy, the vast majority of them are extremely costly, sophisticated and lack flexibility. To address these issues, we have built Raman spectrometers in our laboratory [86, 87] which are relatively simple to build, low-cost and produce high-throughput signal. In this thesis two spectrometers with different spectral resolution have been used and their design and working principles are described below. Figure 2.1 shows a general schematic diagram of the micro-Raman system.

In one of the spectrometer a Nikon Eclipse 50i (Nikon, Japan)microscope was cho-

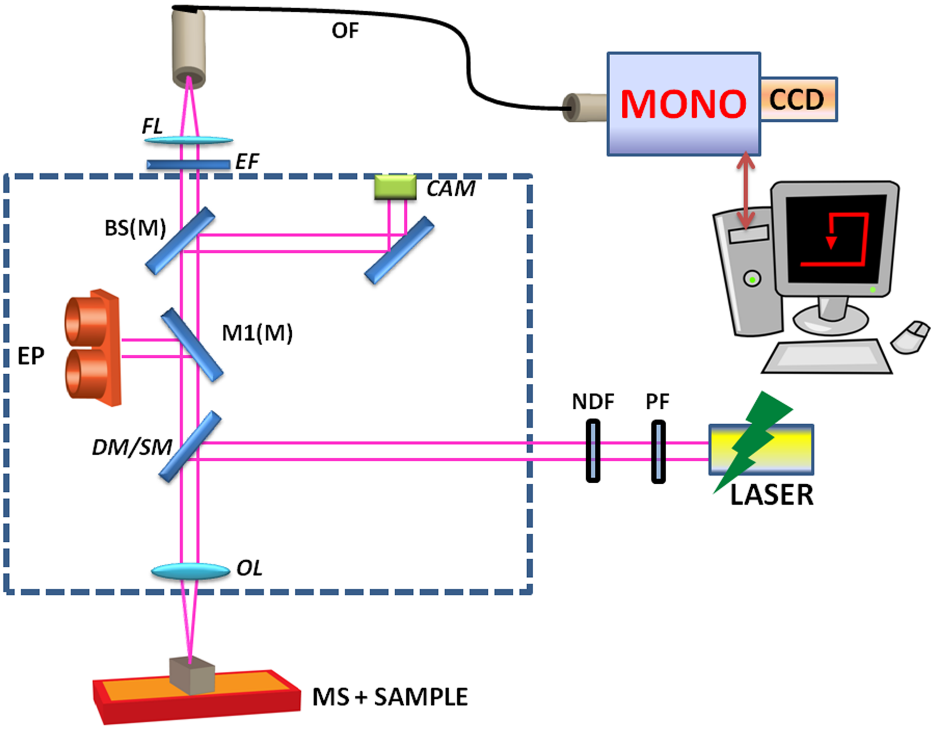

Figure 2.1: Schematic of micro - Raman spectrometer: MS- Micro stage, OL- Objective lens, DM - Dichroic mirror, SM - Special mirror, NDF-Neutral density filter PF -Plasma filter, M1 (M) - Movable mirror, BS (M)- Movable beam splitter, EP - Eyepiece, M2- mirror, CAM - Camera, EF - Edge filter, OF - Optical fiber, FL - Focusing lens, MONO - Monochromator, CCD - Charge coupled device, PC - Personal computer.

sen as the collection optics containing an epi-fluorescent attachment. A 632.8 nm He-Ne laser source (Model No. 30994, Newport,USA) was used as an excitation source, where the light passes through a band pass filter (LL01-633-12.5, Semrock, UK). The epi-fluorescent attachment, which is normally utilized for fluorescent imaging, holds the bayonet mount for putting the white light source for viewing and imaging the sample. Laser beam is passed through this mount. To align the laser along the axis of the microscope entrance, an aluminum disc with 1 mm opening in the center was used which sits securely on the epi-fluorescent lamp attachment. In a fluorescence microscope dichroic mirrors are used to regulate the incident and emission wavelength of the chromophore. If this is retained, the intensity of the Raman spectrum would drop below 200 cm^{-1}

region. In order to extent this range we have designed a special mirror (US Patent No. US8, 179, 525B2 (2012)) and fabricated by Acexon Technologies, Singapore. The mirror has a silver coating of 2 mm diameter and is centered in a ($\pm$0.1 mm) 25.2 $\times$ 35.6 mm^2 fused silica substrate of 1.1 mm thickness. The mirror has a reflection band in the range 400-900 nm, with reflectivity greater than 95 %. As the diameter of the laser beam is 1 mm it is completely reflected into the objective lens of the microscope by the 2 mm diameter mirror. An edge filter is used to suppress the Rayleigh contribution in the scattered light before it enters the optical fiber, in order to avoid fiber Raman. An objective is used to focus the light onto the optical fiber. The optical fiber is a 200 μm multi-mode, single core optical fiber with a band pass of 400 to 1000 nm. The optical fiber is f-number matched with the monochromator (Horiba JobinYvon, iHR 320). A Peltier-cooled CCD (AndoriDus) attached to the monochromator collects the signal and the whole acquisition process is controlled by the Labspec software.

In another spectrometer the collection optics is built from parts of a microscope consisting of focusing unit (LV-IM), sextuple nosepiece (C-N), double port (Y-IDP), universal epi illuminator, (LV-U EPI 2), trinocular tube (Y-TF2) and eyepiece lens (CFI 10x) brought from NIKON, Japan. The whole part is mounted to the optical table using an L-shaped metal holder (US patent No. US8, 179, 525B2 (2012)). As in the other spectrometer dichroic mirror is replaced by special mirror described earlier. Here the excitation source used is frequency doubled Nd-YAG solid state diode pumped continuous laser emitting 532 nm wavelength (model GDLM-5015 L, Photop Suwtech Inc., China). The monochromatic light emitted from the source traverses through a plasma-line filter (LL01-633-12.5, Semrock). Neutral-density filters can be placed in the path to control the power of the laser. The special mirror in the microscope reflects the incoming beam at an angle of 45°. The reflected light then falls on the sample through an infinity corrected microscope objective lens. For most of the experiments (in both spectrometer), we use the infinity corrected objective with 50X magnification (NIKON, L Plan 50X, 0.45 NA, WD 17 mm) , whose numerical aperture and working distance are 0.45 and 17 mm, respectively. The scattered light is collected using the same objective lens and passes through the edge filter (LP03-532RS-25, Semrock) to filter the Rayleigh light before reaching the optical fiber focused (as described earlier) using an objective lens (NIKON L Plan 20X, 0.33 NA, WD 24 nm). The optical fiber delivers the s scattered light to the monochromator (Jobin-Yovn, Triax 550, Instruments SA, Inc., NJ, USA) through a slit of variable width. Using a mirror based f-number matching setup customized for this monochromator. A nitrogen cooled CCD (Spectrum One) is attached to the monochromator as detector. The monochromator consists of three gratings: holographic 1800 grooves/mm, blazed reflection type 1200 grooves/mm (500 nm blaze) and 900 grooves/mm (450 nm blaze). Typically 1800 cm^{-1} grooves/mm with 100 μm slit is used providing a resolution of $\sim$ 2 cm^{-1}. Data acquisition is controlled using the Labspec software.

2.2 Substrate preparation for SERS studies

SERS substrate can be broadly divided into three class: colloidal nano-particle, metallic structures and metallic electrodes. Characteristics of a good substrate are - it can be easily prepared, is reproducible and provide large enhancement. Colloids possess all these characteristics as well as can be dispersed in a solution, hence they are the most

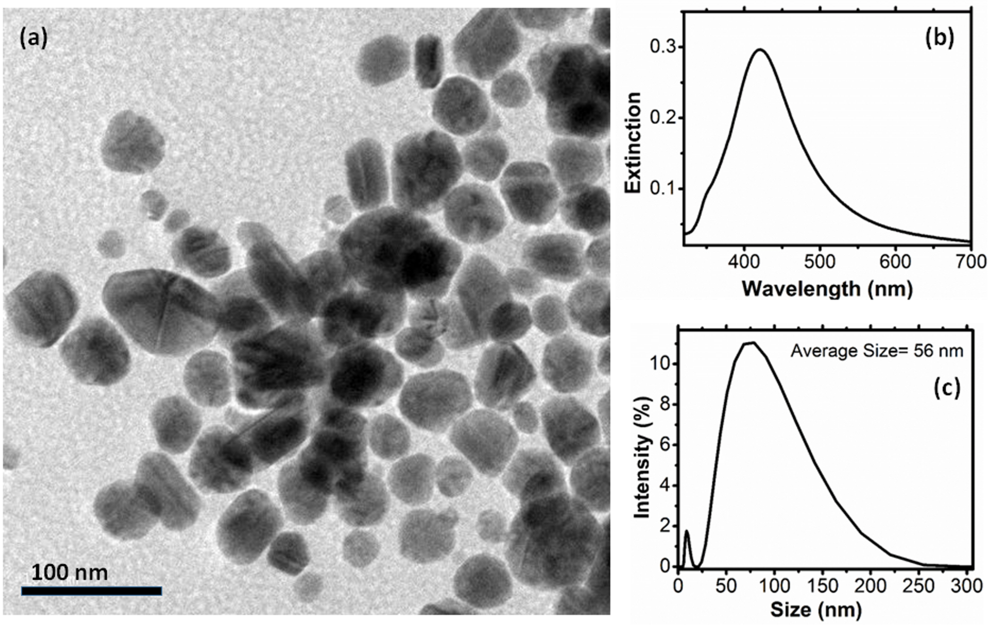

Figure 2.2: The (a) TEM image, (b) absorption spectrum and (c) DLS of silver nanoparticle used in the SERS experiment..

common choice for SERS studies. Silver and gold are the most commonly used nano-particle for SERS studies. Even though gold is more stable and is bio-compatible, silver colloids are preferred for SERS studies because of a much higher enhancement of Raman signals. The most common way of preparing silver nano-particle is by the Lee and Meisel method [88] and in our study also we followed this procedure. 90 mg of silver nitrate was dissolved in 500 mL of milliQ water and bought to boiling temperature. A solution of 10 ml of 1 % of trisodium citrate is mixed in the boiled water which acts both as a reducing and stabilizing agent. The boiling was continued for 1 hour. The resulting solution has a grey-yellowish color. The UV/Vis absorption maximum is typically at $\sim$ 415 nm (see Figure 2.2 (b)). The broadening of the peak is attributed to the poly-dispersity of the colloids, a common feature in this preparation. The average diameter of the colloids were found to be $\sim$ 60 nm as seen from dynamic light scattering study (see Figure 2.2 (c)). TEM image of the nano-particle shows the typical distribution of size of the nano-particle (see Figure 2.2)(a). From our experience we have found that weak capping agents like citrate are good for SERS studies since they can be dislodged easily by the analytes.

2.3 Infrared (IR)

FT-IR spectra of the analytes were recorded using FT-IR Bruker IFS 66V/S spectrometer in a frequency range 3500-500 cm^{-1} with 2 cm^{-1} resolution and 100 scans. For sample preparation ultrapure KBr needs to be kept in a vacuum oven at 110° C for overnight to avoid presence of water in the IR spectra. The samples were pulverized thoroughly with KBr powder by maintaining a weight proportion of around the range of 1:30 using a clean mortar-pestle. This mixture was compacted into a quite thin disc with diameter of 12 mm using a stainless steel IR die set in hydraulic press. After each sample preparation all the parts which has been used were cleaned with suitable solvent and dried to avoid contamination for next sample preparation. A point to be mentioned that less pulverization with KBr lead to the IR spectra with interference pattern because of uneven distribution of sample throughout the pellet.

2.4 DFT calculation

All the DFT calculation for geometry optimization and frequency calculation was carried out using G03 [89] or G09 [90] software with hybrid exchange-correlation functional Becke3-Lee-Yang-Parr (B3LYP) [48, 49]. Basis sets for elements in the upper half of the periodic table (C, H, N, O, S, Na) were chosen to be either 6-31G(d) or 6-31G(d,p) which include polarization function to them (except for H in 6-31G(d)). For

Cu atoms, valence electrons and electrons in the inner shell were described by basis set LANL2DZ and corresponding relativistic effective core potential respectively [58, 59]. Since the theoretical approach and basis set is incomplete, and also anharmonicity is neglected, in order to match the experimental data with theoretically calculated value, scaling factors were employed. The output of the Gaussian provides the Raman activities. To match with the experimental spectra, these are converted to Raman intensity [91–93]. The potential energy distribution (PED) calculation was performed using VEDA programme [94]. Natural bond orbital (NBO) analysis was carried out using NBO 3.1 programme [95] .

CHAPTER 3

Probing conformational changes Induced by Mg^{2+} ion in a Transactivator by SERS [‡]

.

3.1 Introduction

Vibrational spectroscopy is a powerful tool for studying bio-molecules as it provides detailed information of the molecular structure and intermolecular interactions. Moreover, the technique can be applied regardless of the state of the system allowing it to be probed close to the physiological condition. Raman and IR are two main techniques in vibrational spectroscopy. Although IR spectroscopy is a very useful technique, one of the major problems with this technique is the interference from the water bands in the region of interest [11]. However, the problem can be overcome by reducing the path length or using attenuated total reflection (ATR) method [96], but in both cases, short penetration depth is known to affect the sensitivity [97]. In contrast, the Raman spectroscopy is devoid of this problem, but the weak scattered signal poses some limitations to its use. Ultraviolet resonance Raman spectroscopy (UVRR) enhances the signal by 10^4 times over the normal Raman. However, the high energy UV photons may cause photochemical damage to the sample [98]. Surface enhanced Raman scattering (SERS) is an alternative technique which uses the plasmon resonance of noble metal nanopar-

---

[‡] Based on this work, a manuscript has been submitted. Partha P. Kundu, Tuhin Bhowmick, Ganduri Swapna, G. V. Pavan Kumar, Valakunja Nagaraja and Chandrabhas Narayana (*Communicated.*)

ticles or nanoscale surface structures to increase the Raman signal from analytes up to the order of 10^{14} [70]. Hence, SERS requires less laser power, low concentration of the sample and shorter acquisition time. The strong enhancement of the Raman signal has made it possible to study, in some cases, single-molecule through SERS, with no parallel from the other vibrational techniques mentioned above [70–72, 99]. Lower detection limits, narrow spectral bandwidths and the capacity to be used with or without optical labels have made SERS a good choice for various biological applications [23, 61–63, 100–109]. Many studies have reported label-free protein detection using SERS [65, 110–112]. In this work, we have evaluated the utility of SERS to probe conformational transitions occurring in protein upon ligand binding, using a well characterized system. C protein, a transcriptional activator, required for the activation of bacteriophage Mu late genes during the lytic cycle of the phage is used for the present analysis. The protein is dependent on Mg^{2+} for its DNA binding and transactivation [113, 114]. Although studies on conformational changes of proteins by means of Raman spectroscopy has been reported in literature [115–123], SERS has been mainly restricted as a sensitive detection method for quantitative analysis rather than structural analysis [66, 124]. To the best of our knowledge, very few attempts have been made to probe conformational changes using SERS [65–67]. Here, we have carried out a comprehensive SERS study to trace both local and overall conformational changes in this transcriptional activator C.

3.2 Experimental Details

3.2.1 Protein purification

C protein and its mutants were purified from *E. coli* BL26 (DE3) carrying plasmid pVR7 or pVNC4 by following the procedure described earlier [125]. The purified protein was dialyzed against HEPES buffer containing EDTA [10mM HEPES (pH 7.6), 50mM NaCl and 20mM EDTA] for 1hr at 4 C to chelate out the intrinsically bound Mg^{2+}. Further, dialysis was continued in HEPES buffer without EDTA for 2 hrs, with a buffer change after 1 hr. Dialyzed protein was quantified using the Bradford assay and used for SERS analysis.

3.2.1.1 ANS fluorescence

Fluorescence emission spectra were recorded on a Jobin-Yvonfluorometer FluoroMax3, thermostated at 25° C. EDTA treated C protein/ mutant D40N (1μM concentration) were incubated both in the absence and presence of 5mM Mg^{2+} for 15 minutes at 25 ° C. 100μM ANS [8-Anilino Naphthalene-1-Sulfonic acid] dye was added as extrinsic fluor to 1μM protein in Tris pH 7.5 buffer to prepare samples for emission spectra. Next, the samples were subjected to excitation at 360 nm and emission values were integrated between 400-600 nm. All the fluorescence emission spectra and fluorescence intensities were corrected for buffer, Mg^{2+} and ANS intrinsic fluorescence.

3.2.2 DNA binding

DNA binding ability of C protein in presence of nanoparticle was assessed by carrying out electrophoretic mobility shift assay (EMSA) with a 25-bp end labeleddsDNA fragment comprising the C-binding site (CBS-5′ AGATCGATTATGCCCCAATAACCAC 3 ′), The assays were carried out in $TMEG_{100}$ buffer [20mM Tris-HCl (pH 7.4), 5mM $MgCl_2$, 1mM EDTA, 10% glycerol, 100mM NaCl]. Reaction mixtures containing labeled DNA were incubated with C protein on ice for 10 min in the presence or absence of nanoparticle and the samples were analyzed on 6% non-denaturing polyacrylamide gel (30:0.8), in 0.5X TBE buffer (45mMTris-borate and 1 mM EDTA) at 4 ° C.

3.2.3 Molecular Modeling of C protein

Three dimensional structural model of C protein, was generated through homology modeling, using template coordinates from PDB Id: 1RR7, corresponding to Mor protein from Bacteriophage Mu (UniProtKB Accession Code: **P06022**), identified through a sequence homology search using Basic Local Alignment Search Tool (BLAST) at NCBI server http://blast.ncbi.nlm.nih.gov/Blast.cgi?PROGRAM=blastp&BLAST_PROGRAMS=bl ast p&PAGE_TYPE=BlastSearch &SHOW_DEFAULTS=on&LINK_LOC=blasthome, followed by a multiple sequence alignment of BLAST identified homologs through MUSCLE [126]. Energy minimization and structural optimization of thus obtained C monomer model were performed using Prime and (MM96) MacroModel modules of Schrödinger, LLC (Schrödinger, Portland, OR). The force field used was OPLS AA (2005 version). Crystal structure corresponding to the PDB id**1RR7** shows monomers assembling into homodimers using the crystallographic two fold rotation symmetry, which was utilized to generate a dimer model of C. Next, the subunit contact interface for C dimer was analyzed using the program PISA [127], which also suggests that, the model represents the biological dimer assembly of C, with a burial of 2201.7 Å^2 of the hydrophobic surface area at assembly interface. Next, the C-dimer-Mg^{2+} complex was modeled using one Mg^{2+} ion for each of the monomers. Based on the co-ordination geometry of metal ion binding sites found in the structures with PDB id: **1TIL**, **1JGT** and **2XOK** obtained from homology search, the Mg^{2+} ions were positioned to generate the initial coordinates of C-dimer- metal ion complex, which was further energy optimized trough initial Polak-Ribier Conjugate Gradient steps with 'converegence on gradiant' method, followed by Full Matrix Newton Raphson cycles, using Multiple Minimization module (Schrodinger MacroModel suite). The optimized structure was analyzed for interaction of residues at Mg^{2+} binding sites using programs Maestro 8.1 Schrödinger Inc, Pymol [128] and Accelrys DS Viewer Pro^{TM}.

3.2.4 Silver colloid preparation

The Ag solution was prepared by method of Lee and Meisel [88]. Initially, 45 mg of $AgNO_3$ was dissolved in 250 mL of water, and the solution was brought to the boil. Next, a solution of 1% sodium citrate (5 mL) was added under vigorous stirring, and boiling was continued for 60 min. The plasmon absorption maximum was located at 410 nm confirming the expected behaviour of the nanoparticles. The size of the nanoparticle was confirmed by TEM image and DLS measurement.

3.2.5 SERS measurements

SERS spectra of C protein was recorded in the 180° backscattering geometry using 632.8 nm He-Ne laser (model 30995, Research Electro Optics, Inc., U.S.A.) as a Raman excitation source. The spectrometer consists of a monochromator (Horiba JobinYvon, iHR 320) and a Peltier-cooled CCD (AndoriDus) [86]. A holographic 1800 grooves mm-1 grating was used along with the 200 μm spectrograph entrance slit setting, providing $\sim$ 3 cm^{-1} resolution. For SERS studies of protein, a 60 $\times$ infinity-corrected objective (Nikon Plan Apo, Japan, NA 0.9) was used. The laser power used at the sample was 6 mW. The average accumulation time used was 180 s. SERS spectrum shown in Figure 3.5 and Figure 3.7 were background corrected and smoothed using 5 point FFT filter technique Origin software. All analyses (band position and intensity) have been performed by first smoothing the spectra using 15 point FFT filter technique and then taking the second derivative of the spectra (not shown). C protein solution (140 ng/μl) was mixed with colloidal Ag solution in the ratio 1:10 (v/v) and kept for 5 min for adsorption of protein on the nanoparticles. A 10 μl of mixture solution was then drop-coated over a siliconized, hydrophobic glass cover slide (Hampton Research CAT NO HR3-223). The spectra were taken in the liquid form by focusing the objective inside the drop. The hydrophobic surface prevents the drop from flattening, reducing the amount of solution required, which is especially useful when the quantity of sample available is very small.

3.3 Results and Discussion

The transactivator protein C is a dimer [129], that binds dyad-symmetry element upstream and overlapping the -35 region of the target promoters [130]. Although crystal or solution structure of C protein is not reported, circular dichroism (CD) and fluorescence studies showed secondary and tertiary structural changes in C protein upon addition of Mg^{2+} [113, 114]. Hydrophobic reporter dye 1-Anilinonaphthalene-8-sulfonic acid

(ANS) used in fluorescence emission spectroscopy of the wild type C protein, exhibited a blue shift in the emission maxima with an enhancement in fluorescence intensity upon binding to the buried hydrophobic sites of the protein (Figure 3.1). Enhanced fluorescence intensity seen with the protein upon addition of Mg^{2+}, indicated gross tertiary structural changes in the protein (Figure 3.1a). Previous studies[114] also indicated a Mg^{2+} coordinating motif in the protein, consisting of an acidic residue patch, rich in Asp and Glu. Mutation in one of the key residues D40, affected Mg^{2+} binding, leading to a decreased DNA binding and reduction in the level of transcription activation. Unlike the wild type C protein, ANS signal from the mutant D40N showed no response to the addition of the metal ion (Figure 3.1b). In order to get an atomic level understanding of the structural transitions, we have employed SERS, which has all the advantages of the vibrational techniques, but with greater sensitivity. The well-established marker bands in Raman spectroscopy were used in our SERS based studies. We have also taken into account the properties of SERS that are different from normal Raman in terms of selection rule and distance dependency. Unlike normal Raman spectra, where the spec-

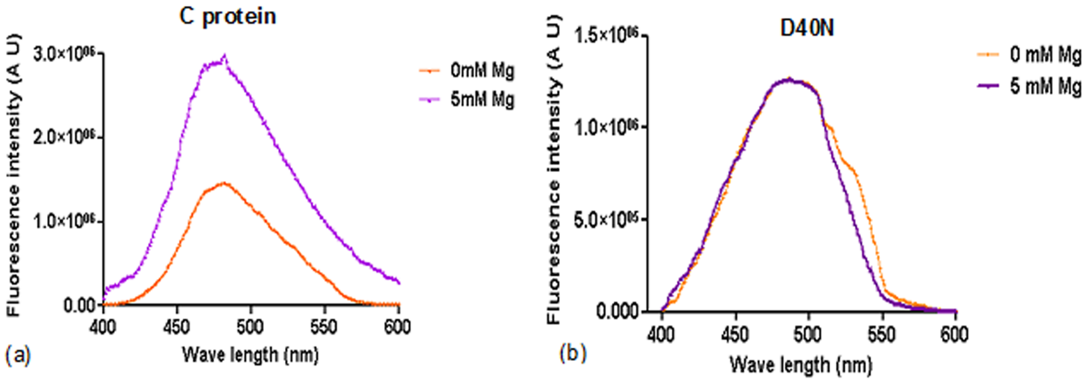

Figure 3.1: Mg^{2+} induced conformational changes in C protein. Tertiary structural changes were monitored by recording fluorescence emission spectra in the presence of extrinsic fluoro ANS as described in experimental details. Background corrected fluorescence spectra of (a) C protein and (b) mutant D40N in the absence (0 mM) and presence (5mM) of $MgCl_2$.

tral contributions arise from all the amino acids of the protein, SERS spectra, in general, is due to those amino acids which are having higher electronic polarizability, and are close to the metal surface. The contributions from amino acids located far away from the metal surface is negligible to the spectra, since the electromagnetic enhancement factor falls off rapidly with the distance of the molecule from the metal surface [131], at a rate of $(\frac{1}{r})^{12}$, where r = distance from metal surface. This seems to be a limitation of the technique, as, (a) the protein should be adsorbed onto the metal surface and (b) interpretation can be made from the signatures of the amino acids as well as amide bands of the protein close to the metal surface. Hence only those proteins can be studied where the region of interest is bound to the metal surface or close to it. This apparent limitation can be circumvented by controlling the orientation of the protein on the metal surface by fusing metal seeking short polypeptide chain to the protein at the permissible site of the protein close to the region of interest [132]. Also protein can be sandwiched between two metal surface to nullify the distance dependent effect [133]. In case of protein C, structure guided analysis of C protein dimer indicated that it could be interacting with citrate reduced silver nanoparticle through basic residues Arg 98 and Arg 108, from the two positively charged patches located at helix 4, 5 and 6 of each monomer (Figure 3.2). This mode of interaction with the Ag nanoparticle orients the two fold axis of C dimer perpendicular to the citrated surface of the nanoparticle, allowing a constellation of basic residues, namely, Arg 87, 105 and 120, which are crucial for C protein-DNA interaction [134] to remain solvent exposed and free. The proposed interaction model was further supported by electrophoretic mobility shift assay (EMSA) studies elucidating the DNA binding ability of C protein in the presence of the nanoparticle (see Figure 3.3). Notably, SERS does not enhance all the Raman active modes of a molecule. According to the surface selection rule [135, 136], SERS enhances only those modes with a component of vibrational amplitude perpendicular to the metal surface, leaving out the component parallel to the surface [137].

3.3.1 Silver colloidal nanoparticle does not interfere with the DNA binding ability of C protein

The success of employing SERS to probe the conformational changes in the protein can only be reflected when the nanoparticle used in the experiments does not interfere with the functional properties of the protein. This was assessed by analyzing the DNA binding ability of C protein in the presence of the nanoparticle. The experiment was carried out with increasing concentration of C protein in the presence or absence of silver colloidal nanoparticle, as described in experimental details. The results indicate that the presence of nanoparticle in the reaction does not affect C protein's DNA binding (Figure 3.3).

3.3.2 Band assignment of C protein

To assess the conformational changes in C protein by SERS, we relied on the band assignment carried out for proteins studied by SERS previously [112, 138–141]. As reported in earlier analyses [107, 112, 138], SERS study of C protein also showed a major spectral contribution from the aromatic amino acid residues due to the strong polarizability of the π electrons in presence of the electric field emanating from the silver surface [138, 142]. Figure 3.2 shows a schematic of the plausible orientation of the protein attached on the silver nanoparticle and the relative distances as a guide to the

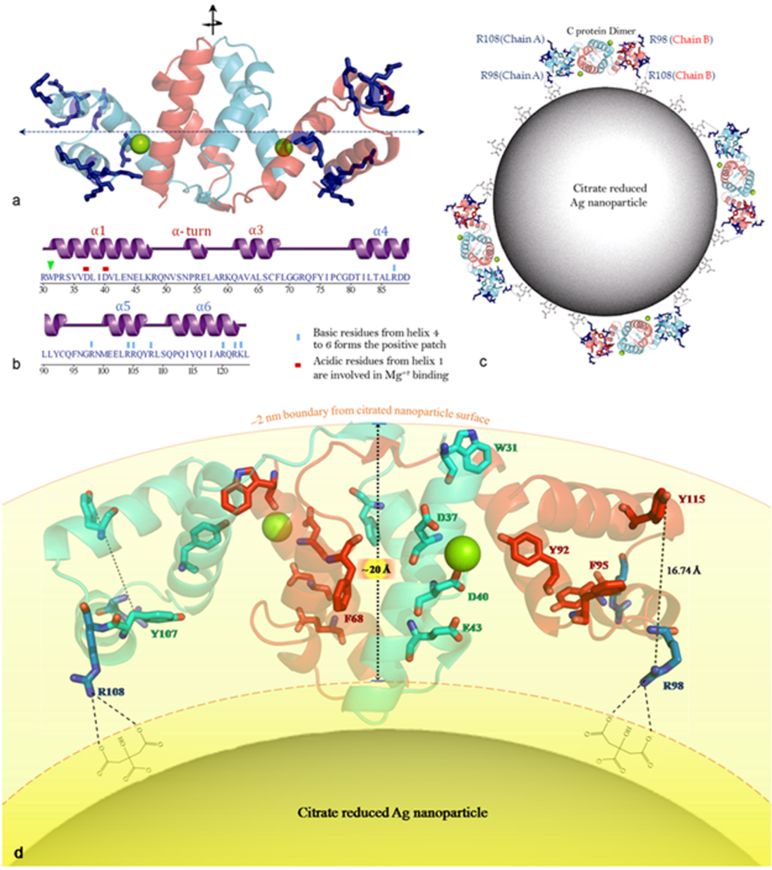

Figure 3.2: Positively charged patches on C protein surface and C's possible mode of interaction with silver nanoparticle. (a) depicts the positively charged Arg and Lys from helix 4 to helix 6 of each monomer in stick representation. The dotted line represents the long axis of C dimer, perpendicular to the 2 fold symmetry axis of dimerization. (b) The blue blocks highlights the position of positively charged patches, consisting of basic amino acid residues, such as, R87, 98, 104, 105, 108, 120, 122 and K123 from each monomer, mapped on a secondary structural representation of C protein. To elucidate the relative location of the acidic patch involved in Mg2+ ion binding, D37 and D40 from helix 1 are also marked by red blocks. The green triangle marks the position of W31 at loop-helix 1 boundary. (c) represents a possible mode of interaction of C protein dimers to the surface of citrate reduced Ag nanoparticles, using the positively charged patches described in (a). (d) The region of C protein within the vicinity ($\sim$2 nm) of the citrated silver nanoparticle surface. Various aromatic residues, such as, W31, Y92, 107, 115, F68, 95 along with acidic residues D37, 40, E43 are represented as sticks, while the R98, 108 involved in the nanoparticle surface anchorage are shown in sticks colored in dark blue.

eye to understand these assignments (Table 3.1). We have drawn an imaginary 2 nm layer over the silver nanoparticle to visualize the contributions to the SERS spectra from various moieties, provided the selection rules are satisfied for these moieties. Similar

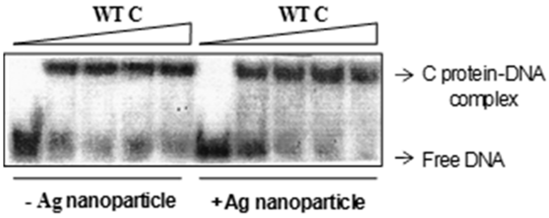

Figure 3.3: Silver colloidal nanoparticle does not perturb the DNA binding ability of C protein. A 25-bp, 5′ P^{32}labeleddsDNA comprising the minimal C-binding site was incubated with C protein with or without nanoparticle, electrophoresed on a 6% non-denaturing PAGE as described in experimental details. DNA binding efficiencies are represented in the figure.

representations have been used for assignments in the previous literature [132, 143].

Table 3.1: Assignments of Raman bands in the SER spectra of Protein C and the mutant Protein C with and without Mg^{2+}

Protein C	**Protein C + 5mM Mg^{2+}**	**Mutant Protein C)**	**Protein C + 5mM Mg^{2+}**	**SERS band Assignments**
625	625	624	624	Phe (ν_{6b})
639	639	639	639	CC skeletal stretch/ ν(C-S) / ring deformation (Phe/Tyr)
721	721	719	719	τ(C-OH)
763	764	763	767	Trp^{W19}
822	822	822	822	Tyr
848	846	844	847	Tyr
929	929	929	927	ν(C-COO$^-$)
1011	1010	1010	1010	Phe((ν_{12}))
1144	1141			Ring stretch / ν_{as}(C$_\alpha$CN)
		1175	1176	Tyr and/or Phe(ν_{9a})
1217	1212	1218	1208	Phe(ν_{7a})
1248	1248	1254	1251	Trp^{W10} and/or Amide III (random coil)
1269	1269	1269	1269	δ(CC$_\alpha$H) and/or AmideIII(α-helix)
1345	1343	1345	1345	Trp^{W7} and/or δ(CH)
1386	1389	1386	1385	ν_s(COO$^-$)
1408	1402	1405	1407	ν_s(COO$^-$)
1449	1445	1445	1445	δ(CH$_2$)

Continued on next page

Table 3.1 – *Continued from previous page*

Protein C	**Protein C + 5mM Mg^{2+}**	**Mutant Protein C)**	**Protein C + 5mM Mg^{2+}**	**SERS band Assignments**
1459	1462	1463	1462	$\delta(CH_2)$
1496	1499	1495	1502	Trp
1580	1582	1580	1582	$\nu_{as}(COO^-)$, Trp^{W2} and/or Phe
1621	1621	1618	1618	Amide I (α-helix)

Abbreviations: ν - stretching; δ - deformation; s - symmetric; as-asymmetric

3.3.3 SER Spectrum of C protein without Mg^{2+}

3.3.3.1 Amide Vibration

The amide I mode consists of the C=O stretching vibration with a small admixture of the N-H bending, while amide II is a combination of the N-H bending and C-N stretching. The amide III mode is also a mixture, but with a different sign in the combination of the coordinates. These modes are highly sensitive to the secondary structure of the protein [11]. In the absence of Mg^{2+}, we observed amide I and III vibrations of C protein. The band at 1269 cm^{-1} is assigned as amide III band, corresponding to the α-helical secondary structure of the protein. This band has an overlap with $\delta(CC_\alpha H)$ vibration (see Figure 3.5). The shoulder at 1248 cm^{-1} can be assigned as amide III band, corresponding to the part of the protein in disordered loop or random coil state. The band at 1621 cm^{-1} is assigned as amide I, which again corresponds to the α-helical regions of the protein. The appearance of this band towards the lower wavenumber range of amide band was also observed by several other proteins, such as, Lysozyme, soybean trypsin inhibitor (STI) [138], p300 [107].

SERS on deuterated C protein

In order to confirm our amide band assignment, we carried out SERS of deuterated C protein in the presence of Mg^{2+}. In normal Raman experiment this method is commonly used to assign bands, particularly for amide modes [144, 145]. The hydrogen to deuterium (H/D) exchange method replaces accessible and exchangeable hydrogens of the protein, both in the main chain amide group N-H as well as the side chain containing acidic groups like OH, NH and SH [144, 146]. In deuterated C protein we observed appearance of a band as a shoulder around 1600 cm^{-1}, which we assigned as amide I′ band due to deuterium exchange. As mentioned, amide I band is a mixture of N-H bending and C=O stretching. Because of deuterium exchange, N-D bending frequency shifts below 1000 cm^{-1} and decouples from C=O stretch. This decoupling results in a small red-shift of the mode, which is designated as amide I′ [11]. Since typically not all amide protons are exchanged with deuterium, both amide I and amide I′ exists in a deuterated protein [11]. The amide I′ band is generally red-shifted by 10-20 cm^{-1} compared to the amide I band [144, 147], as also observed in our experiment, Figure 3.4 . Given the observed magnitude of the band-shift to be around 20 cm^{-1}, we could also rule out the possibility that the band is due to Trp residue, which is known to undergo only a small red shift of 4 cm^{-1} [144]. This distinct nature of the band's sensitivity to H/D exchange confirms our assignment of amide I. Although, amide III band is also sensitive to H/D exchange and shifts to around 950 cm^{-1}, the presence of other strong bands in the region around 950 cm^{-1}, prevented us from its unambiguous detection. However, we do observe a reduction in the intensity of the amide III region around 1245 cm^{-1} upon deuteration. Our assignment is also supported from literature of both normal Raman [148] and SERS [138]. Upon deuteration some other bands change their positions and intensities. Similar changes were observed both in normal Raman [144] and SERS [112]. Due to H/D exchange the nature of mode may change [144] which may affect the observed changes of bands.

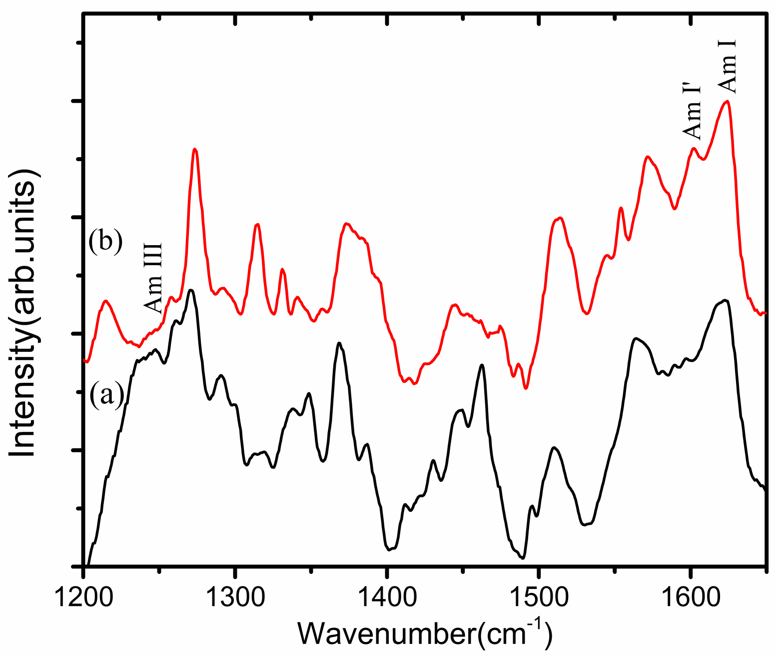

Figure 3.4: SER spectra of C protein in presence of Mg^{2+} (a) in H2O and (b) in D2O. In the deuterated C protein a band at 1600 cm^{-1} appears as a shoulder which is assigned as amide I′. A band at around 1245 cm^{-1} is diminished indicating the plausible contribution from amide III vibration.

3.3.3.2 Aromatic Side-Chain Vibration

SERS spectra of proteins are dominated by amino acids with aromatic side chain because of their affinity to the metal surface. This has been shown in the spectra of bovine serum albumin (BSA), lysozyme and cytochrome C [138, 140, 149]. In this study, we have found significant contribution from the substituted rings of Trp, Tyr and Phe. Phe ring breathing vibrations ν_{6b}, ν_{12}, ν_{7a} were observed at 625, 1011 and 1217 cm^{-1} respectively, owing to the proximity of the Phe residue to the surface. This is rather expected, as Phe 95 is located near the basic patch of the C, involved in nanoparticle adherence. The SERS bands at 763, 1248 and 1580 cm^{-1} are due to the Trp indole ring W19, W10 and W2 vibrations respectively. The appearance of these bands due to Trp (residue no. 30) is consistent with our assumption of the protein lying flat with its twofold dimerization axis perpendicular to the silver surface. The bands at 639, 822 and 848 cm^{-1} are due to Tyr residues. Tyr residues 92, 107 and 115 are located near the positive patch of the C protein, while Tyr 75 is present near the Mg^{2+} binding domain. The characteristic doublet band, which reflects the environmental conditions around different Tyr residues, is commonly used to determine the ratio of the number of Tyr residues buried to exposed in a protein in normal Raman spectrum [115, 116, 150]. These peaks represent Fermi doublet arising from a resonance between the ring breathing vibration and the overtone of the out-of-plane ring bend vibration of the para-substituted phenyl ring in Tyr [151]. Notably, in the SERS spectrum of C in the absence of Mg^{2+}, we observed these bands in the range of 822-848 cm^{-1}.

3.3.3.3 Aliphatic Side-Chain Vibration

The appearance of bands at around 929 cm^{-1} and 1386-1408 cm^{-1}, are due to the stretching vibration of $C\text{-}COO^{-}$ and symmetric stretching of COO^{-}. These bands, carrying the signature of carboxyl groups from either side chains of acidic residues such as Asp, Glu, or the carboxy-terminal of a protein, are common features observed in SERS spectra of all the proteins that get adsorbed on the silver surface [107, 138]. As evident from the Figure 3.2, several acidic residues, such as Asp 88, 89 from helix 4, Glu 101, 102 from helix 5 and Mg^{2+} interacting residues Asp 37, 40 from helix 1 of

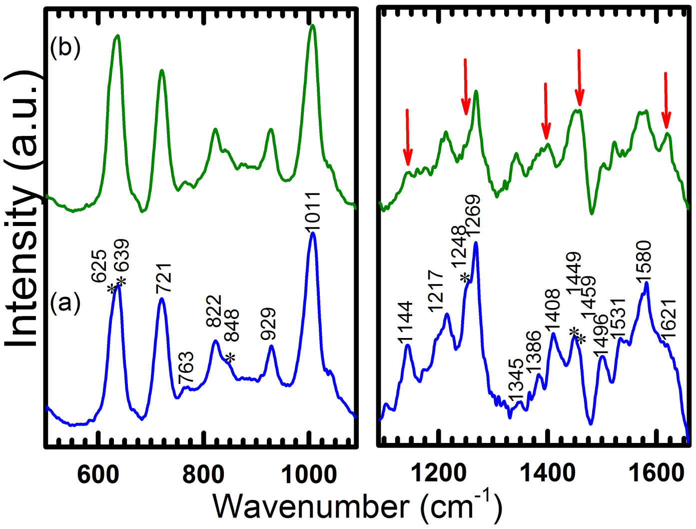

Figure 3.5: Surface enhanced Raman spectrum of C protein in (a) absence and (b) presence of Mg^{2+}. Arrows show the change in spectrum occurred after addition of Mg^{2+} indicating both secondary and tertiary structural change. Spectra are split into two panels to use different Y-axis for clarity of the second panel.

at least one monomer, as well as the terminal carboxyl of C protein lie in vicinity of the silver surface. The band at 1144 cm^{-1} is assigned to $\nu_{as}(C_{\alpha}CN)$ vibration. Deformation mode of CH_2 is also seen at 1449 and 1459 cm^{-1}.

3.3.4 Spectral changes in presence of Mg^{2+}

In case of SERS, conformational changes in the protein would also lead to differences in the alignment of the amino acid residues adsorbed to the metal surface, leading to the appearance or disappearance of some bands. To study conformational changes in transactivator protein C in the presence of the Mg^{2+} [113, 114], only the well-established normal Raman bands were used as markers. The intensity of the band at 1011 cm^{-1} Phe(ν_{12}) was used for normalizing the spectra in order to study the changes occurring in C protein spectra induced by the addition of metal ion. This band is known to be insensitive to the environmental or structural change [152–154]. Moreover, since the band has A_1 symmetry, its intensity should be independent of the change in the protein's orientation on the metal surface following the conformational transitions [135]. Addition of Mg^{2+} gives rise to an increase of amide I band intensity, but a decrease in intensity of amide III band (Table 3.1). This spectral alteration could be due to the (i) change in distance of the polypeptide backbone from the silver surface, (ii) change in the orientation of the secondary structural elements of C protein with respect to the silver surface, or (iii) Mg^{2+} induced conformational transition in C protein triggering an increase in alpha helical content. According to Dieringer et al. [155], the intensity of a peak goes down to one tenth of its initial value at a distance of about 30 Å. As demonstrated in a later section, Mg^{2+} binding induces rather a small root mean square (rms) deviation of $\sim$ 1.5 Åin overall structure. It does not cause any drastic local structural alteration in helix 5 and 6, involved in adherence to the silver surface. Therefore, it is highly unlikely that the observed spectral changes are due to the change in distance from nanoparticle surface. Since amide band corresponds to the vibration of a series of molecular oscillators. The reason (ii) is only valid if there is a large tilt of the existing α-helices, which would be a contradiction with the predictions from molecular modeling. The CD spectral changes recorded earlier [113, 114] indicated a change in helical content of C protein induced by Mg^{2+} binding, which corroborates well with the reason (iii). The increase in the intensity of the amide I band at the expense of amide III is caused by the structural transitions in the C protein, resulting in higher helical content, induced by metal binding. Similar changes in the intensities of the amide bands in SERS has been used to show the change in secondary structures in earlier studies [67, 156]. We observed a decrease in the intensity of the 1144 cm^{-1} ($\nu_{as}(C_\alpha CN)$), which can be attributed to the change in backbone conformation. The change in secondary and tertiary structural elements of C protein involves formation of a stronger hydrogen bond network, which dampens the asymmetric vibration, hence the decrease in intensity. Ferrari et al. [148] used ν (C-N)as a Raman marker band to visualize conformational changes. Among other spectral changes observed in C protein in the presence of Mg^{2+} is the shift of band corresponding to $\nu_s(COO^-)$ from 1408 cm^{-1} to 1402 cm^{-1}. The shift could be caused by the coordination of the Mg^{2+} ion with the carboxyl oxygen of (-COO^-) from the acidic residues involved in metal binding, similar to the ligand induced red shift observed by Ferrari et al. [148] Presence of Mg^{2+} increases the positional separation of the peaks between the symmetric and asymmetric COO^- vibrations, which can be attributed to the involvement of one of the O atom(s) in metal binding [157]. Similarly, the increase of 1345 cm^{-1} band corresponding to the Trp residues could be attributed to the conformational changes in C protein altering the orientation of the contributing Trp(s). Further, the band at 1459 cm^{-1}, which appears as a shoulder, increased in intensity in the presence of Mg^{2+}. This band is due to CH_2 deformation and is a signature of hydrophobic interactions [158, 159]. Therefore, this change can be ascribed to the increased hydrophobic interactions arising due to the tertiary structural transition in presence of Mg^{2+}.

Addition of $MgCl_2$ does not induce aggregation in Ag colloidal solution

In order to demonstrate that the observed changes in the SERS spectrum of C protein is not induced by the aggregation of nanoparticles upon $MgCl_2$ addition, we compared the UV-Vis spectra of Ag nanoparticle with and without $MgCl_2$. The final concentration of $MgCl_2$ was kept the same (0.5 mM) as that of the SERS experiment. Nanoparticle

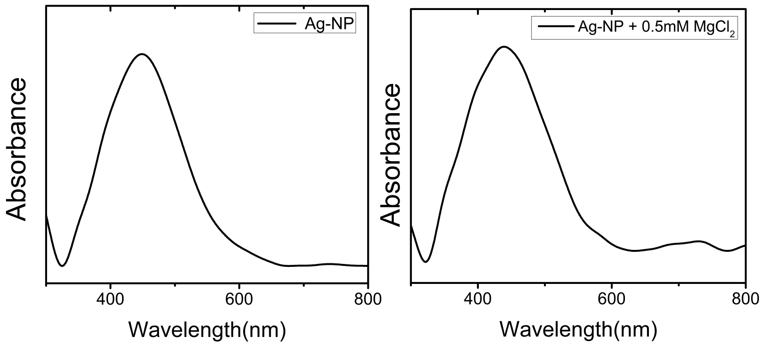

Figure 3.6: Effect of $MgCl_2$ on colloidal silver nanoparticle. As can be seen from figure addition of $MgCl_2$ does not produce any detectable aggregation of colloidal solution.

aggregation can be detected through broadening and weakening of the main transverse peak at the expense of a broad plasmon band at the longer wavelength [131, 160] of the UV-Vis absorption spectra. As can be seen from Figure 3.6, we did not perceive any significant change in the intensity and the width of the main plasmon band. The appearance of a small broad band at around 730 nm could be attributed to a minor fraction of Ag nanoparticle aggregates. Thus, the experiment demonstrates that the addition of $MgCl_2$ does not bring about any appreciable change in the distribution of nanoparticle size.

3.3.5 SER Spectrum of mutated C protein

In order to verify the above analysis, similar studies were carried out with mutant C protein D40N, compromised in Mg^{2+} binding. In the SERS spectra of the mutant, we observed very little change in the intensity of the amide I and III bands upon addition of Mg^{2+} (see arrows in Figure 3.7). Further, due to the inability of the mutant protein to bind Mg^{2+}, the band at 1405 cm^{-1} corresponding to the COO^- group did not shift appreciably. Unlike wild type C, no significant change in the intensity due to $\delta(CH_2)$ was observed. An increase in intensity of 1345 cm^{-1} can be attributed to altered orientation(s) of Trp side chain, possibly caused by non-specific and transitional interaction with metal ion.

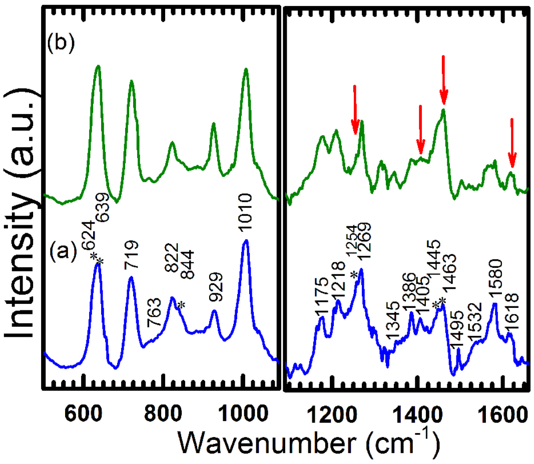

Figure 3.7: Surface enhanced Raman spectrum of mutant C protein in (a) absence and (b) presence of Mg^{2+}. Arrows are associated with peaks which showed substantial changes in wild type C protein. Spectra are split into two panels to use different Y-axis for clarity of the second panel.

3.3.6 Molecular modeling

To better understand the structural transitions occurring in the transactivator C protein detected by SERS, the spectral data were correlated with the three dimensional model of C. In the model of the C protein dimer-Mg^{2+} complex, each monomer is shown to bind one metal ion. The metal binding site of C protein is comprised of a negatively charged patch at dimeric interface, rich in acidic residues, such as, Asp 37, 40, Glu 43 from one monomer and Asp 89 from the other. The interaction of acidic residues D40 and D37 with Mg^{2+}, at the site of metal binding is elucidated in Figure 3.8. Structural superimposition of energy minimized molecular models of C dimers, generated in the absence and presence of the bound Mg^{2+} ions showed an rms deviation of about 1.5 Å (Figure 3.8). This reveals an overall structural change in C protein upon metal ion bind-

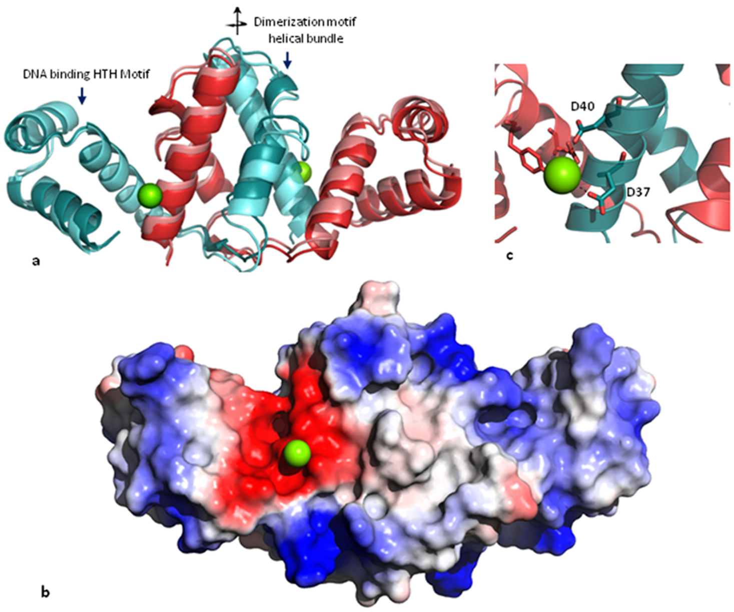

Figure 3.8: Molecular Modeling of C protein for structural elucidation of Mg^{2+} ion binding and induced conformational changes. C protein monomers assemble into dimeric form following a twofold rotational symmetry. Monomer chain A and B are displayed in teal and red respectively. (a) depicts 3D structural alignment of energy minimized C protein dimer models, in the presence and absence (displayed in lighter shades of teal and red) of Mg^{2+} ions. (b) A representation of the surface electrostatics of C-dimer, displaying the Mg^{2+} ion binding site. The binding site harbors a negatively charged patch, formed by acidic amino acids, such as D37, D40, E43 from one monomer, and D89 from other. (C) depicts the interaction of metal ion with acidic residues D37 and D40. Color codes corresponding to residue charges (Blue: positive, Red: negative).

ing, consistent with the spectral changes observed in SERS. The model also showed that the single Trp residue contributing to the band at 1345 cm^{-1} is located at a helix-loop boundary (Figure 3.2 b) and hence prone to minute structural perturbation caused even by the non-specific metal interaction(s). The inherent transient nature of the Trp environment suggests its exclusion as a marker from this study. However, the conformational change in the C-dimer is of crucial implications, as it leads to high affinity DNA binding by the protein followed by transcription activation [114, 134]. Further, our study also establishes Mg^{2+} interacting residue D40 as an important perturbation point in the whole process, as mutation of D40 to N abolishes the protein's ability to undergo allosteric transition into active state upon Mg^{2+} binding.

3.4 Conclusions

In summary, we have shown the effectiveness of the SERS to study the secondary as well as tertiary structural changes in proteins. The increase in alpha helical content and the concomitant fall in random coil observed by SERS, suggest the applicability of the method to study secondary structural transitions. The changes of SERS band intensities associated with altered orientations of aliphatic and aromatic side chains, and conformational changes in the peptide backbone indicate structural changes in C protein upon Mg^{2+} binding. The changes caused by the coordinate interactions between side chain carboxyl groups from acidic residues of C and bound Mg^{2+} are detected which act as a trigger for the allosteric transition. Application of SERS, as demonstrated here for a transcription factor thus appears to offer a new means of studying conformational changes in a diverse class of regulatory proteins. A large number of DNA transaction proteins undergo conformational changes upon ligand binding in order to carry out their regulatory functions. SERS does not require a label to be attached to the protein for detecting conformational changes. Most of the regulatory proteins are indeed found in low concentration in the cells and hence SERS could be envisioned as a useful future technique for imaging applications. As shown previously with peptides [161], our SERS based exploration of the ligand induced conformational changes in C protein also demonstrates the possibility of its application as a highly sensitive nanoscale detection method of biological or chemical stimuli in vitro. SERS, therefore stands as an attractive and powerful biophysical tool to explore various biological processes, expanding the feasibility of application into systems with minute sample availabilities.

CHAPTER 4

Raman and Surface Enhanced Raman Spectroscopic Studies of Activator Molecules of Histone Acetyl Transferase P300 †

4.1 Motivation

In the present work, we employed Raman and SERS to characterize N-(4-chloro-3-trifluoromethyl-phenyl)-2-ethoxy-benzamide (CTB) and N-(4-chloro-3-trifluro-methyl-phenyl)-2-ethoxy-6 pentadecyl-benzamide (CTPB), which are synthesized from salicylic acid and anacardic acid [108, 162]. Figure 4.1(a,b) shows the molecular structure of CTB and CTPB. These molecules were discovered by Kundu and coworkers[108, 162] and are the only known activators of the histone acetyltransferase (HAT) p300. It has to be noted that p300 is probably the most widely studied HATs. It is related to a number of diverse biological functions, such as, proliferation, cell cycle regulation, apoptosis, differentiation and DNA damage response [163–168]. It is a potent transcriptional coactivator and possesses intrinsic HAT activity. Furthermore, p300 mediated protein (both histone and non-histone) acetylation controls several important cellular functions including DNA repair, cell cycle, differentiation and establishment of retroviral pathogenesis. Since it is involved in numerous important cellular events, dysfunction of p300 may be the underlying roots of several diseases including a

---

† This work has appeared in *J. Mol. Struct.*, **999**, 10 (2011). Reproduced with permission from Elsevier.

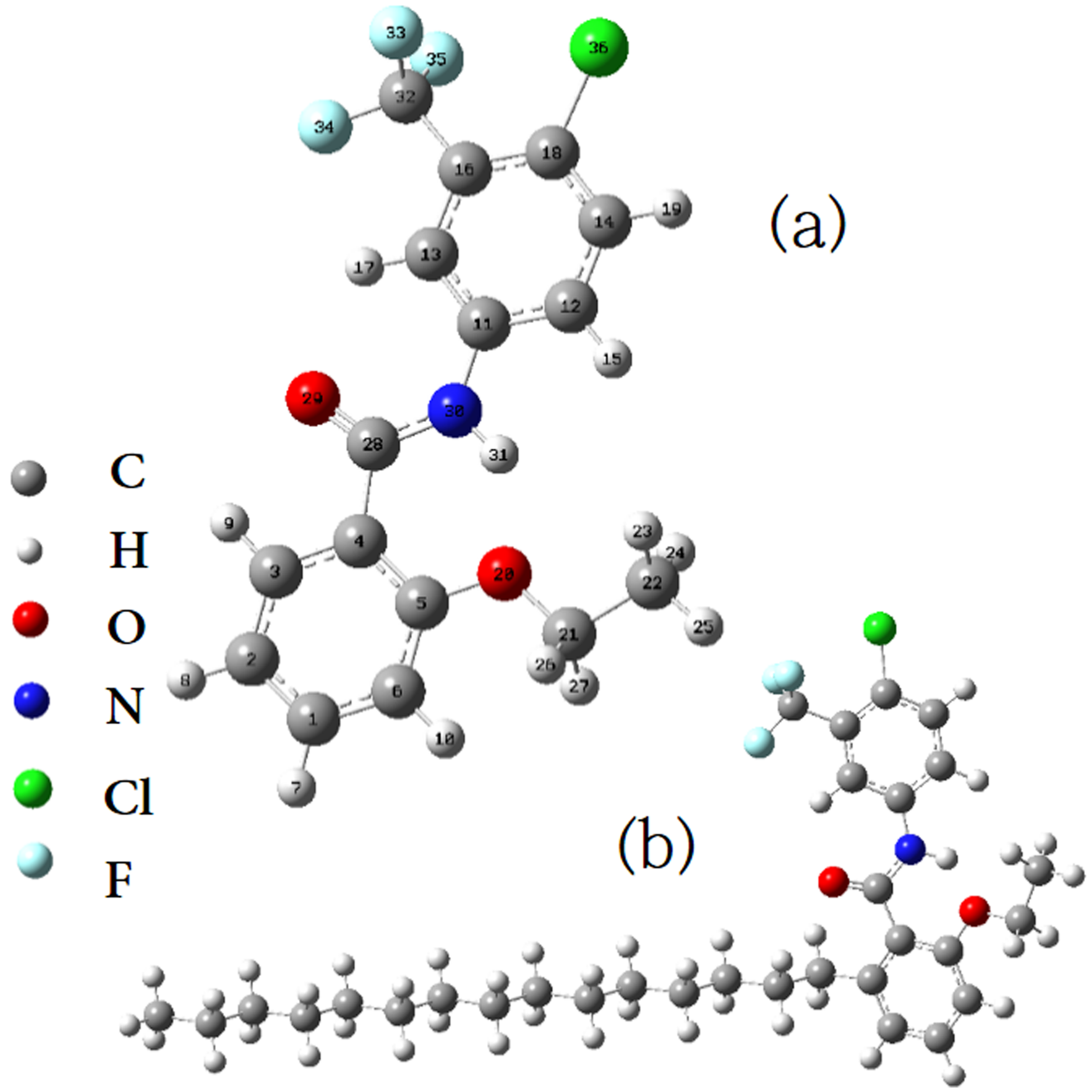

Figure 4.1: The optimized structure of (a) CTB and (b) CTPB.

few types of cancers, cardiac hypertrophy, asthma, and diabetes [163–168]. It has been shown [108] that both CTB and CTPB binds to p300 primarily through hydrogen bonding and hydrophilic, hydrophobic interactions. Therefore, the small molecule activator of p300, CTB and CTPB, are therapeutically important lead-molecules. In an attempt to understand the role of CTB and CTPB on the HAT activity of the p300 we have carried out detailed SERS studies at nano-molar concentration of p300 full length protein in physiological condition [108]. Since no structural information exists for p300, this was the first study on such large proteins using SERS. The result provided important signature in the amide regions, which could be used to look at the protein. CTB/CTPB complex in-vivo inside cellular environment. Our group is interested in deploying Raman imaging through SERS and tip enhanced Raman spectroscopy (TERS) for such studies. It is important to note that both CTB and CTPB are insoluble in water. Recently it was shown that CTPB tagged carbon nano spheres could be delivered through blood brain barrier in a mice brain and could modulate gene expression, in vivo [169].

While studying the p300 spectra with CTB/CTPB, due to the insoluble nature of CTB and CTPB we were unable to look at the contribution of CTB and CTPB in the spectra. This is important to understand the Raman spectra vis-a-vis docking studies through molecular dynamic simulation in order to gain valuable information to derivatize these molecules for better efficiency. In addition the Raman and SERS studies of insoluble molecules will be important for in-vivo Raman imaging of cell. This motivated us to perform Raman spectroscopy and SERS on CTB and CTPB, which is presented in this chapter. The Raman spectra of CTB and CTPB were also simulated using DFT and compared with the experimental values.

4.2 Methods

4.2.1 Experimental details

A detailed procedure of the synthesis of CTB and CTPB can be found elseshere [108, 162]. Silver nanoparticles were prepared by the standard Lee and Meisel method [88]. The average size of the nanoparticle was measured to be $\sim$ 45 nm. It had a plasmon band centered at 425 nm.

A custom built Raman microscope was used for all the measurements, whose details can be found elsewhere.[107] All the spectra reported here were recorded using frequency doubled Nd-YAG 532 nm laser. The power at the sample was measured to be 15 mW. The typical signal accumulation time for Raman and SERS measurements were 120s and 30s, respectively. A 100 X objective with a numerical aperture of 0.95 was used in the $180\,^\circ$ scattering geometry.

Powder samples of CTB and CTPB were used for Raman measurements. For SERS, we centrifuged 100 mL of Ag colloids at 10,000 rpm for 4 minutes. The clear supernatant was discarded and the thick blackish gray colored concentrated nanoparticles were transferred to a separate container. 2 μL of concentrated Ag nanoparticles was deposited on a clean glass slide and left for drying at room temperature. 1μL of 6 μM solution of molecule (CTB or CTPB) in methanol was drop coated over the deposited nanoparticle surface. When the solvent evaporated, we washed the slide with methanol so that any molecule not bound to the Ag by covalent bond would be washed away. As soon as methanol was evaporated we performed the SERS experiment.

4.2.2 Raman spectra calculation details

All the calculations reported herein were performed with Gaussian 03 suite of programs [89]. Ground state structure is obtained by carrying out a full geometry optimizations with DFT/6-31G (d) basis set using hybrid Becke's 3 Parameter exchange functional and Lee, Yang and Parr correlation functional (B3LYP). We have calculated Raman spectrum at the same level of theory. Since B3LYP level overestimate the calculated vibrational frequency due to neglect of anharmonicity in real system scaling factor of 0.9613[170] has been used to produce good agreement with experiment. We have not observed any imaginary frequency which suggests that the molecule is in local minimum on the potential energy surface. The assignments of the calculated wavenumbers are aided by the GAUSSVIEW program, which gives a visual presentation of vibrational modes.

The Raman activities (S_i) obtained from GAUSSIAN 03W were converted to Raman relative intensities by the following relationship[171],

$$I_i = \frac{f(\nu - \nu_0)^4 S_i}{\nu_i[1 - \exp(-\frac{hc\nu_i}{kT})]}$$

where ν_0 is the exciting frequency (in cm^{-1} units); ν_i is the vibrational wave number of the i^{th} normal mode: *h*, *c*, *k* are the universal constants; and *f* is the suitably chosen common scaling factor for all the peak intensities.

4.3 Results and discussion

The structural difference between CTB and CTPB is the presence of an additional pentadecyl chain in CTPB. Therefore, it is expected that the vibrational properties of the two molecules to be similar. Since these molecules are insoluble in water, SER spectra could not be detected using Ag hydrosol. In order to circumvent this problem we have to centrifuge Ag hydrosol and perform SERS on dry Ag substrate.

4.3.1 Geometrical parameters of CTB

To the best of our knowledge, there is no X-ray crystallographic data for CTB. Our theoretical calculation assisted by Gaussian reveals the following geometrical parameters which may assist crystallographer for further studies of CTB. C_{28}-O_{29} bond (1.2281

Å) shows typical double bond characteristic (see Figure 4.1). However both the C-N bonds, C_{28}-N_{30} (1.3766 Å) and C_{11}-N_{30} (1.4025 Å) are shorter than normal C-N bond length 1.48 Å. This reveals the effect of resonance in this part of the molecule [172]. The carbon-oxygen distance C_5-O_{28} (1.3739 Å) is in agreement with the average distance of 1.362 Å found among phenols. Our DFT calculation gives the enlargement of the angle C_5-C_4-C_{28} by 7.7 ° and reduction of angle C_3-C_5-C_{28} by 5.5 ° compared to the normal 120 °. This asymmetry in angles reveals the interaction between O_{29} and phenyl ring I. The C-C bond lengths of the two phenyl ring Ph I and Ph II are between 1.3930-1.4173 Å and 1.3888-1.4370 Å respectively. These bond lengths are somewhere between normal values for a single (1.54 Å) and double bond (1.33 Å). The C-H bond lengths lie between 1.0829-1.0867 Å (Ph I) and between 1.0789-1.0874 Å (Ph II). The angle C_6-C_5-O_{20} increases by 1.8 ° and the angle C_4-C_5-O_{20} decreases by 1.9 ° from the normal. This indicates the repulsion between benzene ring and ethoxy group. Now we will discuss the Raman spectrum of CTB, followed by the SERS spectrum.

4.3.2 Raman spectrum of CTB

The observed Raman bands (see Figure 4.2) with their relative intensities, calculated (scaled) wave numbers and assignments are given in Table 4.1.

Table 4.1: Raman shift (cm^{-1}) and assignment of vibrational modes of CTB

Calc. Raman (scaled) (cm^{-1})	**Relative intensity**	**Expt. Raman (cm^{-1})**	**SERS (cm^{-1})**	**Assignments**
3423	32	3314*m*		$\nu(N-H)$
3169	8	3183*w*		$\nu(C-H)$ Ph II

Continued on next page

Table 4.1 – *Continued from previous page*

Calc. Raman (scaled) (cm^{-1})	**Relative intensity**	**Expt. Raman (cm^{-1})**	**SERS (cm^{-1})**	**Assignments**
3102	35	3067*s*	3068*w*	$\nu(C-H)$ Ph II
3071	26	3024*w*	2975*s*	$\nu(C-H)$ Ph I
3015	28	2995*w*		$\nu_{as}(CH_3)$
2961	18	2937*m*	2929*s*	$\nu_{as}(CH_2)$
2944	27	2885*w*	2874*w*	$\nu_s(CH_3)$
2920	20	2867*w*		$\nu_s(CH_2)$
1687	99	1684*m*		Amide I
1601	168	1620*s*	1621*s*	$\nu_{8b}(C=C)$ ring Ph II, $\beta(N-H)$, $\beta(C-H)$ Ph II
1535	75	1567*m*	1567*m*	$\nu(C=C)$ ring Ph II, $\beta(N-H)$, $\beta(C-H)$ Ph II
1471	25	1483*w*	1485*vs*	$\delta_{as}(CH_3)$
1437	48	1447*m*	1420*m*	$\beta(C-H)$ Ph I
1403	63	1356*m*	1356*m*	$\nu(C=C)$ ring Ph II, $\beta(N-H)$, $\beta(C-H)$ Ph II
1318	157	1337*m*	1329*m*	$\nu_{19b}(C=C)$ ring Ph II, $\beta(N-H)$, $\beta(C-H)$ Ph II, $\nu(C-N)$
1208	214	1255*s*	1251*m*	$\beta(N-H)$, $\beta(C-H)$ Ph I & II , $\nu(C-OC_2H_5)$
1170	40	1196*w*	1153*m*	$\beta(C-H)$ Ph II
1085	22	1141*w*	1128*m*	$\beta(C-H)$ Ph II
1040	44	1073*w*		$\nu(C=C)$ ring Ph I, $\beta(C-H)$ Ph I
1004	43	1056*m*	1049*w*	$\nu_{12}(C=C)$ ring Ph II, $\beta(C-H)$ Ph II,
904	11	948*w*	936*m*	$\nu(C-OC_2H_5)$
787	15	822*w*	822*m*	$\delta(C=C)$ ring in plane Ph I, $\beta(C-OC_2H_5)$
731	16	774*w*	767*w*	$\delta_s(CF_3)$
680	20	713*w*	705*s*	$\delta(C=C)$ ring in plane Ph I & II
600	13	671*w*	651*w*	$\delta(C=C)$ ring in plane Ph I
559	7	624*w*	622*w*	$\delta(C=C)$ ring in plane Ph II , $\delta(CF_3)$

Continued on next page

Table 4.1 – *Continued from previous page*

Calc. Raman (scaled) (cm^{-1})	**Relative intensity**	**Expt. Raman (cm^{-1})**	**SERS (cm^{-1})**	**Assignments**
510	14	535w	537w	$\delta(C=C)$ ring in plane Ph I
431	19	453w	470w	$\beta(C-N-C)$, $\nu(C-Cl)$
385	12	399w		$\beta(C=O)$
364	27	380w	390w	$\beta(C-F)$
345	22	359w	361w	$\beta(O-C-C)$
295	15	300w		$\sigma(CF_2)$, $\beta(C-Cl)$
261	20	267w		$\tau(CH_3)$
161	46	175w		$\gamma(C-N-C)$, $\gamma(C-H)$ Ph I, γ ring $(C=C)$ Ph I
113	81	125w		$\gamma(C-N)$, $\tau(C_2H_5)$, γ ring $(C=C)$ Ph II
			234vs	$\nu(Ag-N)$

Abbreviations: ν - stretching; β - in plane bending; γ - out of plane bending;
δ - deformation; σ - scissoring τ - torsion
vs-very strong; s-strong; m-medium; w -weak
Subscripts : s-symmetric; as-antisymmetric

In order to investigate the performance and vibrational wave numbers of CTB, root mean square (RMS) value and correlation coefficient between calculated and observed wave numbers were calculated (see Figure 4.3). RMS values were calculated using the following expression[173]

$$RMS = \sqrt{\frac{1}{n-1}\sum_{i=1}^{n}(\nu_i^{exp} - \nu_i^{calc})^2}$$

The RMS error for Raman bands are found to be 40. Small differences between the calculated values and observed wave numbers were found. It must be due the fact that the hydrogen bonds present in the crystal strongly perturb the wavenumbers and the

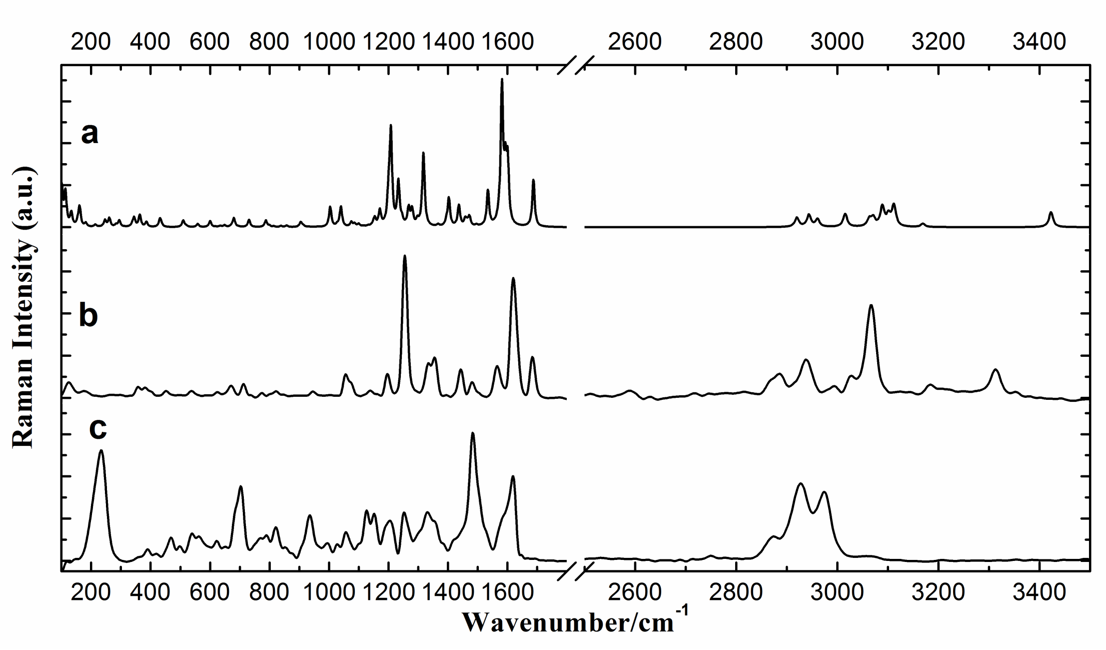

Figure 4.2: (a) Calculated Raman spectrum, (b) Raman and (c) SERS of CTB

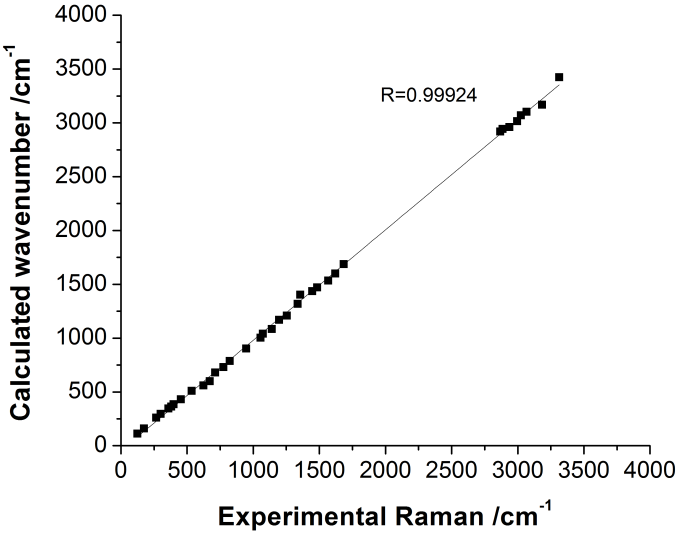

Figure 4.3: Correlation graph between experimental and calculated value.

intensities of many modes. Also, the calculation was performed in the gas phase where as the experiment has been done on solid phase.

Herein, we discuss some important vibrational modes.

4.3.2.1 Carbamoyl vibrations

The $N - H$ stretching vibration appears broadly in the region 3300-3500 cm^{-1}. In the case of CTB, we observe $N - H$ stretching frequency at 3314 cm^{-1}. This is a characteristic vibration commonly associated with secondary amide group. The calculated value for this mode is at 3423 cm^{-1}. The CNH vibrations in which N and H atoms move in opposite direction of carbon atom appear at 1581, 1535 and 1403 cm^{-1} theoretically. The corresponding experimental values are 1620, 1567 and 1483 cm^{-1} respectively.

The CNH vibrations in which N and H atoms move in the same direction of carbon atom appear at 1318 and 1208 cm^{-1} (theoretical). Experimentally those bands appear at 1337 and 1255 cm^{-1}.

The $C - N$ stretching vibration coupled to in plane bending $\beta(N - H)$ appears at 1337 cm^{-1}. Panicker et al.[174] observed the band due to stretching vibration $\nu(C-N)$ at 1314 cm^{-1} for similar molecule. This mode is not pure but contaminated by other modes.

Amide I vibrations mainly correspond to $C = O$ stretching with a small contribution from $N - H$ bending. The amide I vibration was found to be 1684 cm^{-1} in Raman spectrum of CTB. It has been previously observed that amide I modes are around 1650 to 1685 cm^{-1} for similar molecule. Our DFT calculation gives this mode at 1687 cm^{-1}. A weak band at 399 cm^{-1} is assigned as in plane bending $\beta(C = O)$. The DFT calculation predicts this mode at 385 cm^{-1}.This mode is mixed with other vibration.

4.3.2.2 Phenyl ring vibration

CTB has two substituted benzene rings (see Figure 4.1). We describe the di- and tri-substituted phenyl rings as Ph I and Ph II respectively. The modes in two phenyl ring will differ in wavenumber, and the magnitude of splitting will depend on the strength of interaction between different parts of the two rings .For some modes, the splitting is so small that they may be considered as quasi-degenerate and for other modes a significant amount of splitting is observed [175–177]. The carbon-hydrogen stretching frequency $\nu(C-H)$ lie in the region 3000-3100 cm^{-1} region. In some cases stretching modes are perturbed well above 3100 cm^{-1} [178]. In our study the theoretical values lie in the region 3071-3169 cm^{-1} are in agreement with the experimental values in the region 3024-3183 cm^{-1}.In the case of benzene there is an in plane ring deformation ν_{12}.[**?**] For mono-, meta- and 1,3,5-trisubstituted benzenes, this occurs at 1010±10 cm^{-1}. But if any substitution that involves 2-,4- or 6- position, the band become substituent sensitive and move out of the 1010 cm^{-1} region. We observe the ν_{12} mode at 1056 cm^{-1}. Phenyl compounds have characteristic bands near 1500 cm^{-1} (ν_{19a} and ν_{19b}) [178]. In benzene they are degenerate and Raman inactive. Substitution of benzene ring by an X-group removes the degeneracy and they become Raman active. We observe the ν_{19b} mode at 1337 cm^{-1} for the phenyl ring Ph II. Phenyl compounds possess two characteristic bands near 1600 cm^{-1}. These bands are assigned as ν_{8a} and ν_{8b} [178]. In pure benzene these modes are degenerate. Substitution of benzene ring by an X- group removes the degeneracy. We observe ν_{8b} mode for the phenyl ring Ph II at 1620 cm^{-1} and our calculated value is 1601 cm^{-1}.

The in plane $C-H$ bending mode $\beta(C-H)$ spatially couple with other modes and sensitive to $C - X$ substitution. These modes appear above 1000 cm^{-1} region. We observe a series of weak to medium bands in the region 1000-1600 cm^{-1}.

4.3.2.3 Carbon-halogen vibration

For $C - Cl$ vibration where chlorine is attached to the ring, there can be mixing of vibration due to lowering of the molecular symmetry and the presence of heavy atom on the periphery of the molecule [174]. Mooney [179, 180] assigned vibrations of $C - Cl$, Br and I in the wavenumber range of 1129-480 cm^{-1}. For 4-Chlorophenyl boronic acid $C - Cl$ stretching frequency is reported in the region of 724-452 cm^{-1} [181]. We observe this mode at 453 cm^{-1} (experiment) and 431 cm^{-1} (DFT). Arslan et al. [172] observed $C - Cl$ bending mode at 431, 435 and 441 cm^{-1}. For 4-Chloro phenyl boronic acid [181] these bands are assigned at 287 and 236 cm^{-1}. We observe this band at 300 cm^{-1} which is in agreement with the DFT calculation (295 cm^{-1}).

We observe weak bands at 624, 380 and 300 cm^{-1} which are assigned as CF_3 deformation $\delta(CF_3)$, $C - F$ bending $\beta(C - F)$ and CF_2 scissoring $\sigma(CF_2)$. The band at 724 cm^{-1} is assigned as $\delta_s(CF_3)$ which is in well agreement with the DFT calculation (731 cm^{-1}). All these assignments match well with the existing literature [182–184].

4.3.2.4 Vibration of ethoxy group

In ethoxy group $C-H$ stretching vibration occurs in the region 2860 to 2995 cm^{-1}. The antisymmetric $C - H$ stretching [178] is found between 2930 and 2995 cm^{-1} where as symmetric stretching occurs in between 2860 and 2930 cm^{-1}. In methyl groups there are three bands, two of which are degenerate. We assign the bands at 2995 cm^{-1} and 2885 cm^{-1} as $\nu_{antis}(CH_3)$ and $\nu_s(CH_3)$ respectively. DFT calculation gives those bands at 3015 and 2944 cm^{-1} respectively. For methylene group the bands at 2937 and 2867 cm^{-1} are assigned as $\nu_{antis}(CH_2)$ and $\nu_s(CH_2)$ mode. Methyl antisymmetric deformation occurs at 1483 cm^{-1} which is in agreement with its calculated value (1471 cm^{-1}). We observe stretching mode $\nu(C - OC_2H_5)$ at 1255 and 948 cm^{-1}. Bending mode $\beta(C - OC_2H_5)$ occurs at 822 cm^{-1}. Our DFT calculation predicts these modes at 1208, 904 and 787 cm^{-1} respectively. The torsional mode of ethyl and methyl groups is expected at low wavenumber region. We observe them at 125 and 267 cm^{-1} which is in well agreement with the existing literature [185].

4.3.3 SERS of CTB

The SERS spectrum of CTB does not exhibit the $N - H$ stretch because, the hydrogen is deprotonated and $Ag - N$ bond is formed in the presence of Ag surface. In such a case, one expects the $Ag - N$ vibration to evolve in the SERS spectrum. We observe a very strong band at 234 cm^{-1} in SERS spectrum associated with $Ag - N$ stretching. This clearly indicates the bond formation between the Ag and N. This is a characteristic feature of SERS spectra when Ag interacts with molecules containing nitrogen atom [186, 187]. This also suggests that there is a strong chemical enhancement component in the SERS spectrum, wherein the metal-molecule composite lead to $Ag - N$ bond formation, thereby enhancing the Raman spectrum of a adsorbed molecule [188].

We observe $C - H$ stretching vibrations of phenyl rings at 3068 and 2975 cm^{-1}, which suggests that phenyl ring may be approximately perpendicular to the silver surface, possibly in a tilted position. The presence of in-plane bending modes $\beta(C - H)$ of the of the aromatic ring at 1621, 1567, 1420, 1356, 1329, 1251, 1153, 1128 and

1049 cm^{-1} supports the tilted position of the rings with respect to the silver surface. The presence of the ring stretching mode at 1621, 1567, 1356 and 1329 cm^{-1} and the in-plane ring deformation mode 1049, 822, 705, 651 and 573 cm^{-1} suggests the tilted position of the rings. We observe very strong band at 1485 cm^{-1} due to antisymmetric deformation of methyl group. This should be related to the closeness of the methyl group to the metal surface. The bands at 2929 and 2874 cm^{-1} due to $\nu_{as}(CH_2)$ and $\nu_s(CH_3)$ supports this fact. Also these bands are red shifted compared to the normal Raman spectrum. This suggests the interaction of this group with metal surface.

4.3.4 Raman and SERS of CTPB

Normal, simulated and SERS of CTPB is depicted in Figure 4.4. Since CTB and CTPB have similar structure, except for the extra alkyl chain, we expect the spectra to be similar. The detail band assignments, relative intensity of experimental and calculated Raman bands are given in Table 4.2. The performance of our DFT result is shown in the correlation graph (see Figure 4.5). The RMS value for CTPB was calculated to be 45.1.

Table 4.2: Raman shift (cm^{-1})and assignment of vibrational modes of CTPB

Calc. Raman (scaled) (cm^{-1})	**Relative intensity**	**Expt. Raman (cm^{-1})**	**SERS (cm^{-1})**	**Assignments**
3457	22	3262w		$\nu(N-H)$
3114	34	3089w		$\nu(C-H)$ Ph I
3080	43	3065w		$\nu(C-H)$ Ph I
3063	29	3031w	3003w	$\nu(C-H)$ Ph I
3012	28	2972w	2971s	$\nu_{as}(CH_3)$

Continued on next page

Table 4.2 – *Continued from previous page*

Calc. Raman (scaled) (cm^{-1})	**Relative intensity**	**Expt. Raman (cm^{-1})**	**SERS (cm^{-1})**	**Assignments**
2990	33	2957w	2927s	$\nu_{as}(CH_3)$
2945	42	2923m		$\nu_s(CH_3)$
2924	85	2898w		$\nu_s(CH_3)$
2914	156	2868s	2865w	$\nu_{as}(CH_2)$
2898	150	2831s		$\nu_{as}(CH_2)$
1688	111	1675s	1672w	Amide I
1599	160	1642m	1646w	$\nu_{8b}(C=C)$ ring Ph II, $\beta(N-H)$, $\beta(C-H)$ Ph II
1578	151	1613m	1595m	$\nu(C=C)$ ring Ph II, $\beta(N-H)$, $\beta(C-H)$ Ph II
1523	48	1541w	1532m	$\nu(C=C)$ ring Ph II, $\beta(N-H)$, $\beta(C-H)$ Ph II
1470	61	1489m	1481s	$\sigma(CH_2)$ (chain)
1460	148	1462m		$\sigma(CH_2)$ (chain)
1400	49	1437m	1443w	$\nu(C=C)$ ring Ph II, $\beta(N-H)$, $\beta(C-H)$ Ph II
1317	141	1351m	1387m	$\nu_{19b}(C=C)$ ring Ph II, $\beta(N-H)$, $\beta(C-H)$ Ph II
1289	120	1320m	1336m	$\tau(CH_2)$ (chain)
1220	186	1276s	1272w	$\beta(N-H)$, $\beta(C-H)$ Ph I & II , $\nu(C-OC_2H_5)$
1170	32	1207m	1205m	$\beta(C-H)$ Ph II
1108	29	1152m	1150m	$\delta(CH_2)$, $\delta(CH_3)$ chain
1004	43	1060m	1062m	$\nu_{12}(C=C)$ ring Ph II, $\beta(C-H)$ Ph II,
779	15	788w	786m	$\gamma(C-H)$ Ph I
752	15	773w	754m	$\delta(C=C)$ ring in plane Ph I
726	8	739w		$\delta(C=C)$ ring in plane Ph I, $\delta_s(CF_3)$
669	25	703m	703m	$\delta(C=C)$ ring in plane Ph I & II
647	9	672w		$\delta(C=C)$ ring in plane Ph I
586	6	638w	621m	$\gamma(N-H)$
521	15	578m	572w	$\beta(C-H)$ Ph I, $\rho(CH_2)$(chain)

Continued on next page

Table 4.2 – *Continued from previous page*

Calc. Raman (scaled) (cm^{-1})	**Relative intensity**	**Expt. Raman (cm^{-1})**	**SERS (cm^{-1})**	**Assignments**
442	12	461w	453w	$\beta(C-H)$ Ph I, $\rho(CH_2)$(chain)
425	12	426w	416w	$\nu(C-Cl)$, $\omega(CH_2)$ (chain)
405	20	393w		$\rho(CH_2)$ (chain)
348	22	355w	350w	$\rho(CH_2)$ (chain), $\beta(C{-}OC_2H_5)$
293	20	303w		$\sigma(CF_2)$, $\beta(C-Cl)$
254	13	267w		$\tau(CH_3)$
222	28	231w		$\gamma(C-H)$ Ph I, γ ring $(C=C)$ Ph I
153	15	173w		$\gamma(C-N-C)$, $\rho(CH_2)$ (chain), $\beta(C-OC_2H_5)$, $\tau(C_2H_5)$
119	110	128m		γ ring $(C=C)$ Ph II, $\gamma(C-H)$ Ph II, $\tau(C_2H_5)$
			238vs	$\nu(Ag-N)$

Abbreviations: ν - stretching; β - in plane bending; γ - out of plane bending;
δ - deformation; σ - scissoring τ - torsion
vs-very strong; s-strong; m-medium; w -weak
Subscripts : s-symmetric; as-antisymmetric

As can be seen from Table 4.2, the presence of additional alkyl chain causes either some extra peaks to appear or contributing to the peaks already existing in case of CTB. Here we will be focussing only on the major differences in CTPB, both in normal Raman and SERS, compared to CTB.

In normal Raman spectrum, the bands at 3262 cm^{-1} due to $N-H$ stretching and band at 3065 cm^{-1} due to $C-H$ stretching from the phenyl ring appeared as weak bands compared to those of the CTB. The peaks at 2868 and 2831 cm^{-1} due to stretching of methylene group become stronger. Amide I band at 1675 cm^{-1} emerge as a strong band. At 1489 and 1462 cm^{-1} we observe two medium bands which appear owing to

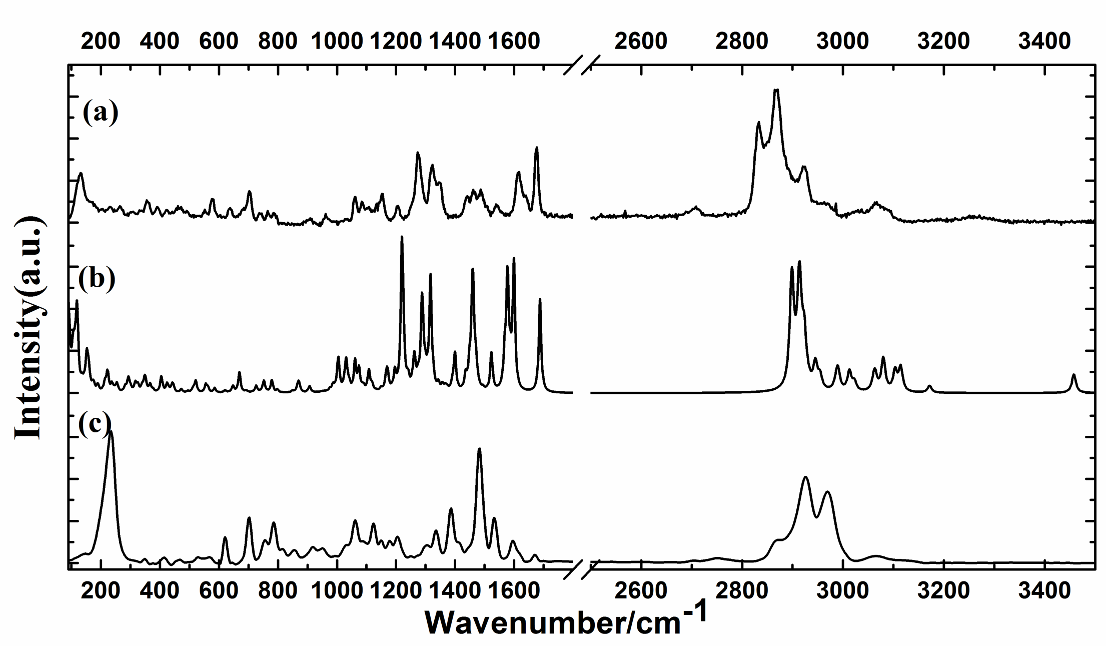

Figure 4.4: (a) Experimental Raman spectrum, (b) Calculated Raman and (c) SERS of CTPB

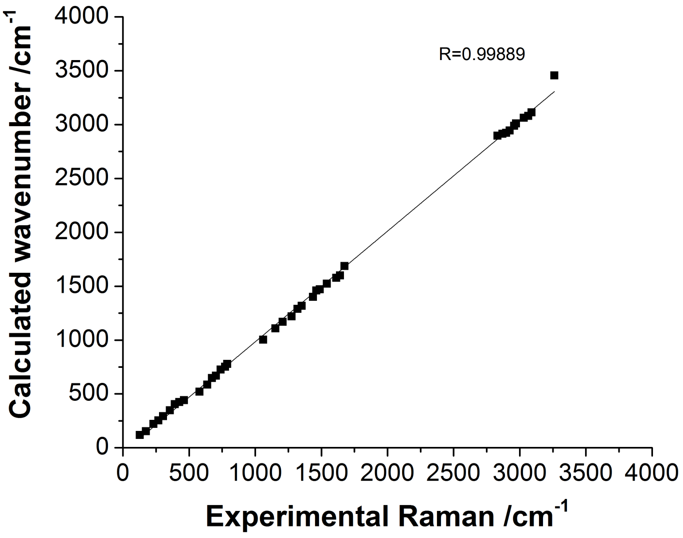

Figure 4.5: Correlation graph between experimental and calculated value.

CH_2 scissoring of the alkyl chain. We perceive another band attributable to the torsion of CH_2 from alkyl chain. A band at 1152 cm^{-1} is assigned to deformation of methylene and methyl group of the chain. Rocking of CH_2 occurs at 578, 461, 393, 355 and 173 cm^{-1} which are mixed with vibrations from other parts of the molecule. We observe a band at 426 cm^{-1} attributable to waggging of methylene group.

In SERS, one important difference we found was the appearance of weak amide I band. A strong band at 238 cm^{-1} suggests that, as in case of CTB, formation of $Ag-N$ bond upon de-protonation of $N-H$ group. Thus we conclude that, in SERS of CTPB, the $C=O$ and $N-H$ vibrations are decoupled and we get contribution from only from $C=O$ stretching. A band due to $\nu_{8b}(C=C)$ stretching due to phenyl ring appears only as a weak band in contrast to the strong band as in case of CTB. These small differences point at slight variance in orientation of CTB and CTPB on silver surface.

4.4 Conclusion

We have performed Raman and surface enhanced Raman spectroscopy on CTB and CTPB, the specific activator molecules of the HAT activity of the p300, for the first time. The molecular geometries and the wavenumbers was calculated using DFT method with 6-31G(d) basis set. The observed wavenumbers were found to be in agreement with calculated values. Based on the analysis of SERS and Raman spectrum the adsorption of CTB and CTPB to the silver surface was shown to occur through the nitrogen atom. Both the rings were oriented in a tilted position on the silver surface. Our SERS analysis would be helpful in understanding the interaction mechanism of these molecules with p300 as well as other proteins.

CHAPTER 5

Selective Detection of Cu^{2+} by SERS [§]

5.1 Introduction

Copper is third-most-abundant transition metal in the human body and plays an important role in a broad range of biological processes like redox processes, enzyme functions, pigment synthesis, antioxidant defense [189, 190]. Copper deficiency is the major factor leading to an increased risk of developing coronary heart disease [191–195]. Copper in excessive amounts can be toxic and cause oxidative stress and disorders associated with neurodegenerative diseases, including Menkes and Wilson diseases, Alzheimers disease, prion disorders, and amyotrophic lateral sclerosis [196–202]. United States Environmental Protection Agency (EPA) has set the maximum allowable limit of copper in drinking water as 1.3 milligrams per Liter (mg/L) i.e. ~ 20 μM. Therefore, it is important to develop innovative techniques for the detection of this redox-active cation in biological and environmental samples.

To date, many analytical techniques have been developed, for example, ion chromatography [203], voltametric sensors [204], atomic absorption or emission spectroscopy [205] for quantitative detection of inorganic atomic ions, which provides detection limit in the range ppm (μM) - ppb (nM). However, these methods suffer from considerable sample preparation, destructive nature and analysis time [73]. SERS could be an alternative technique which has the advantage of ultra sensitivity, requires little or

---

[§] Based on this chapter work, a manuscript is under preperation, Partha P. Kundu, D. Maity, T. Govindaraju and C. Narayana.

no sample preparation and is non-destructive. Nevertheless, since SERS is a molecular technique, it cannot be directly used to detect atomic ions, indirect way needs to be adopted. One such method is to rely on aggregation of plasmonic nanoparticles in the presence of specific ion by a receptor and signal is acquired from a highly active Raman reporter attached to the nanoparticle in the 'hot spots' created by such an aggregation [206–208]. One major drawback of such approach is the number of hot-spots created with such uncontrollable aggregates may a yield different signal intensity under similar experimental conditions [73, 209]. This makes this method qualitative or at best semi-quantitative. To circumvent such problem, an alternative is to find a highly SERS active molecule which acts both as a sensor and a Raman reporter and undergoes changes in geometrical and electronic parameter leading to the change in its spectrum.

Since the Raman reporter is directly involved in the binding process, it can act as an internal standard and making quantitative detection possible [73]. Several authors have reported different organic ligands to detect a wide variety of cations [210–213]. Recently, Sarkar *et al.* [214] demonstrated an effective way of $\mathrm{Cu}^{(II)}$ detection down to 15 μM. The sensitivity of these methods depends upon the SERS activity of the molecule used to interact with the ions. Generally, a highly Raman active molecule is also a good SERS scatterer. The molecule with a bigger size, containing extended π systems are easily polarizable and a good candidate for SERS. In the present study, we have chosen julolidine - carbonohydrazone (compound **1**) as our Raman active probe, which has all the characteristics of being a good Raman scatterer. Previously it was shown [215] that this novel compound can detect Cu^{2+} by absorption spectroscopy selectively down to 20 μM when 10 μM ligand was used. The binding of the Cu^{2+} ion is accompanied by a shift of the absorbance peak in the near infrared (NIR) region. The ability of absorbance spectroscopy to provide structural changes upon Cu^{2+} binding is limited. Raman on the other hand is very sensitive to the mode of binding and protonation state [216]. This motivates us to compare the Raman spectra of this compound in its free and Cu^{2+} bound form which provides first experimental evidence of the binding mechanism. Our findings are further supported by the use of DFT calculations. Finally, we developed a method based on SERS to improve the limit of detection (LOD) such so as to detect Cu^{2+} ion in the drinking water below the maximum permissible amount as set by EPA. Our study can be helpful to track the distribution of Cu^{2+} in living cells.

5.2 Methods

5.2.1 Computational Methods

All density functional theory (DFT) calculations were carried out by Gaussian 09 software [90]. Geometry optimization was performed using hybrid exchange-correlation functional Becke3-Lee-Yang-Parr (B3LYP) [48, 49]. Basis sets of C, H, N and O atoms were chosen to be 6-31G(d,p) which include polarization function to them. It was shown [215] by Job's plot and mass spectrometry analysis that Cu^{2+} binds to the compound **1** in a 1:2 stoichiometric ratio. Accordingly, we considered two Cu^{2+} in the complex with **1**. We have considered coordination of water molecules to the Cu ions. According to MALDI/TOF-MS it looses two H^+ in the complex form. Consequently, we considered deprotonation of the hydroxyl functional groups in the complex form. Valence electrons and electrons in the inner shell of Cu atoms were described by basis set LANL2DZ and corresponding relativistic effective core potential respectively

[58, 59]. It was shown [215] for the complex the lowest energy corresponds to a triplet state (S_Z=1, two Cu (II) cation with d^9 electron configuration (S_Z=1/2)). In open shell system unrestricted DFT method is required for electronic structure calculation. Since in UHF wave function spin contamination may occur, the expectation value of total spin $\mathbf{S}^2$ must be inspected to validate the theoretical results. The final calculated value of $< \mathbf{S}^2 >$ for the complex is 2.0387, close to the value of 2, the expectation value for the triplet ground state wave function with no spin contamination, thus verifies the validity of our theoretical results. The harmonic Raman frequencies were computed on the optimized structures using the same level of theory. Since the theoretical approach and basis set is incomplete, and also anharmonicity is neglected, in order to match the experimental data with theoretically calculated value, scaling factors were employed. For compound **1** the scaling factor used was 0.961 [217] and for the complex with metal scaling factors were calculated by minimizing the RMS deviation from the experimental values. Different scaling factors for different region were used to better match with the experiment, 0.9 for 1000-1300 cm^{-1}, 0.96 for 1300-1500 cm^{-1} and 1.0 for 1500-1700 cm^{-1}. The output of the Gaussian provides the Raman activities. To match with the experimental spectra, these are converted to Raman intensity [91–93]. The potential energy distribution (PED) calculation was carried out by VEDA program [94].

5.2.2 Raman Spectroscopy

All Raman and SERS spectra were recorded using two different spectrometers, both with 180° backscattering geometry. One of the spectrometer consists of a monochromator (Horiba Jobin Yvon, iHR 320), a Peltier-cooled CCD (Andor iDus) and a 632.8

nm He-Ne laser (model 30995, Research Electro Optics, Inc., U.S.A.) as an excitation source. Compound **1** was measured in this spectrometer. The other spectrometer comprises of frequency doubled Nd-YAG 532 nm laser, a SPEX TRIAX 550 monochromator and a liquid nitrogen-cooled CCD (with CCD 3000 controller, ISA Jobin Yvon). All other measurements have been done on this spectrometer. The laser power at the sample for 632.8 nm was $\sim$ 5 μW and that for 532 nm was $\sim$ 10 μW. The Typical accumulation time were 1-3 minutes. A holographic 1800 grooves mm^{-1} grating was used with the 200 μm spectrograph entrance slit setting, giving $\sim$ 2 cm^{-1} resolution. A 50 $\times$ infinity-corrected objective (Nikon L Plan, Japan, NA 0.45) was used. All the spectra was smoothened using 5 point FFT filter technique in Origin software.

5.2.3 Silver colloid preparation for SERS study

Silver colloid was prepared following the method of Lee and Meisel [88]. Briefly, 90 mg of AgNO3 was dissolved in 500 mL of water, and the solution was brought to the boiling temperature. Thereafter, a solution of 1 % sodium citrate (10 mL) was added under vigorous stirring, and boiling was continued for 60 min. The maximum of the plasmon absorption band was located around 410 nm close to the value reported in literature.

5.2.4 Raman and SERS measurement

Raman of compound **1** is measured in the powder form. For a spectrum of complex with Cu^{2+}, a 50 mM sample is made in DMSO. Thereafter, the solution is diluted with a aqueous buffer medium (50 mM, 2-(4-(2-hydroxyethyl)-1-piperazinyl) ethanesulfonic acid (HEPES)/CH$_3$CN, 6:4, v/v; pH 7.2) so that the final concentration of the compound is 2mM. Then 10 equivalent Cu^{2+} is added to the solution and kept for drying before Raman measurement. For SERS measurement a 5 μM solution is made in the same buffer. Then various metal ions were added with different concentration and kept for 5 min. This was followed by the solution is mixed with Ag sol in 1:10 v/v and dried on a hydrophobic surface [218] so that the sample is confined to a small area, increasing the density of the molecules being probed.

5.3 Results and discussion

5.3.1 Raman band assignments of compound 1

The optimized structure of the ligand **1** and the complex form is shown in Figure 5.1. The experimentally obtained and the corresponding theoretically calculated spectra of the ligand is shown in Figure 6.3. Here, we assigned the bands in the range 1100-1600 cm^{-1}, (see Table 5.1) since this is the region where pronounced peaks appear and hence the changes of these modes would be useful for detection of Cu^{2+} binding.

Two bands at 1171 and 1191 cm^{-1} are ascribed to the twisting of the caged methylene group. PED calculation shows that these modes are not pure. The band at 1171 cm^{-1} has contribution also from the (C-H) bending and (N-N) stretching . The corresponding theoretical mode appears at 1154 cm^{-1}. The band at 1191 cm^{-1} has a small contribution from (N-N) stretching and appears at 1166 cm^{-1} in calculated spectrum. These assignments are also confirmed from literature [219–223]. Recently, we also found this mode in the same range for compound containing methylene group [74, 224].

The mode at 1230 cm^{-1} occurs due to the coupling of phenyl C-O stretching with

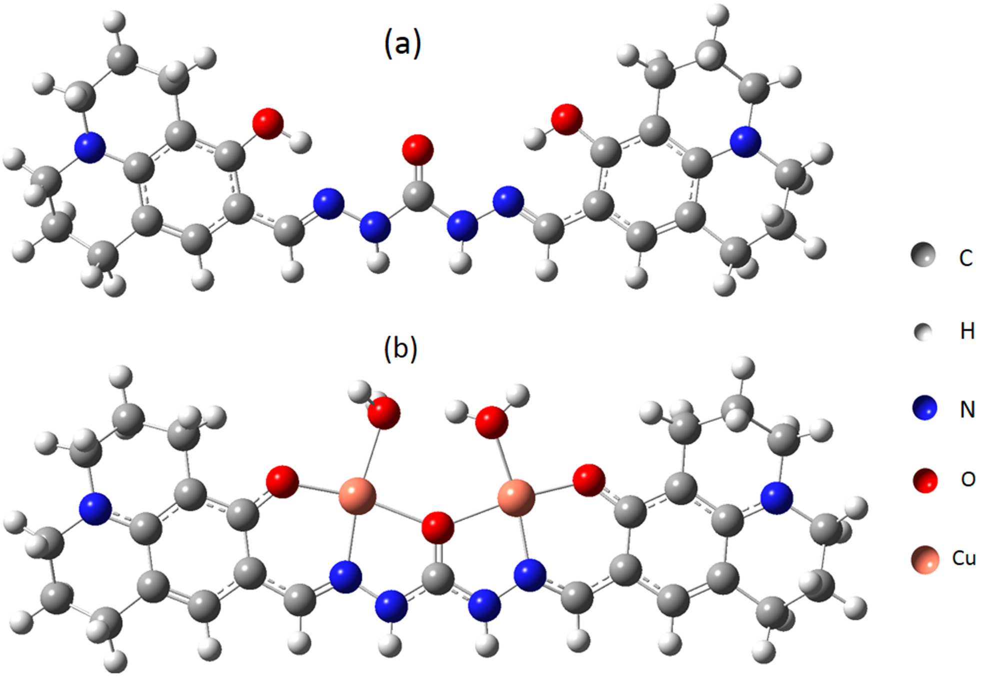

Figure 5.1: The optimized structure of julolidine - carbonohydrazone (ligand**1**) and its complex with Cu^{2+}.

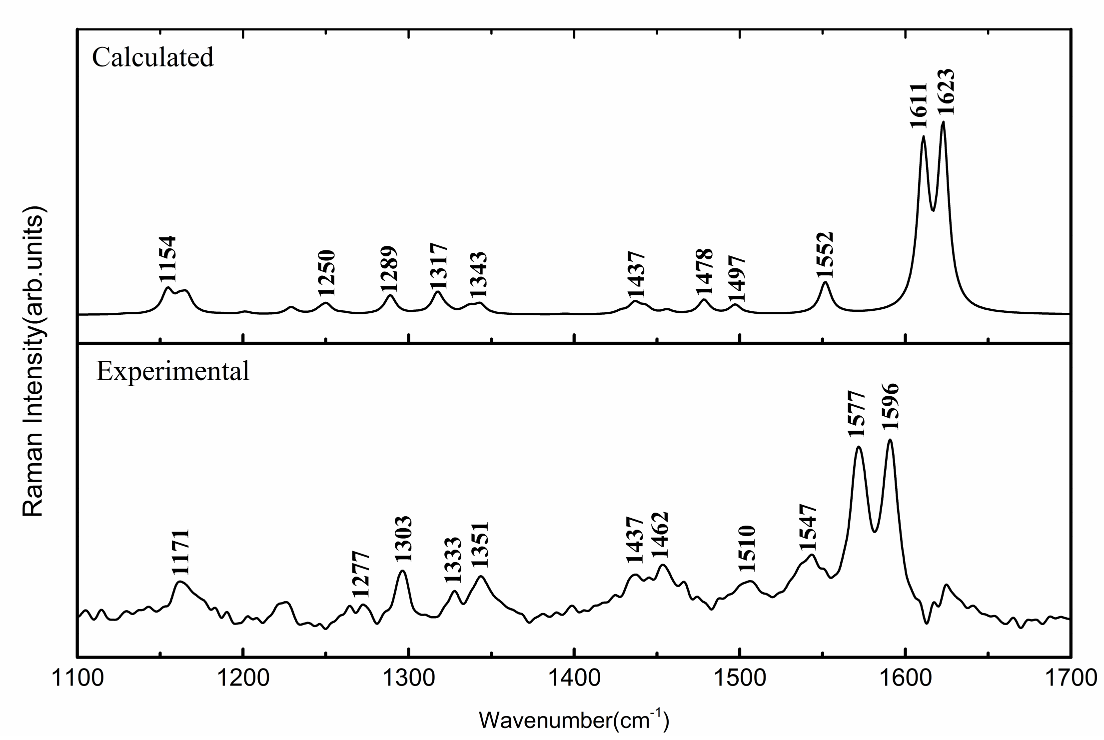

Figure 5.2: The experimental and theoretically calculated Raman spectrum of ligand **1**.

Table 5.1: Raman shift (cm^{-1}) and assignment of vibrational modes of compound **1**

Calc. Raman (scaled) cm^{-1}	Relative Intensity	Expt. Raman cm^{-1}	Assignments (PED)
1154	12	1171 m	ν(N-N) (10), τ(CH_2) (16), β(C-H) (16)
1166	9	1191 w	ν(N-N) (18), τ(CH_2) (45)
1229	4	1230 w	ν(O-C) (20), ring (C=C) (20)
1250	5	1277 w	ν(C=C) ring (15), ν(C-C) ring (10)
1289	9	1303 m	β(CH)
1317	12	1333 m	ν(C=C) ring (31)
1343	5	1351 m	ω(CH_2) (46)
1437	6	1443 m	σ(CH_2) (50)
1478	8	1462 m	σ(CH_2) (28), β(N-H) (28)
1497	5	1510 m	ν(N-C) ring (21), σ(CH_2) (27)
1552	18	1547 m	ν(C=C) ring (38), β(O-H) (17)
1611	88	1577 s	ν(C=C) ring (32), ν(C=N) (16)
1623	100	1596 s	ν(C=N) (62)

Abbreviations: ν - stretching; β - in plane bending; ω - wagging
σ - scissoring τ - twist; s-strong; m-medium; w -weak

the C=C ring stretching as observed from PED calculation. C-O stretching vibration occurs in the range 1000-1250 cm^{-1} [178]. This mode is in excellent agreement with the theoretically calculated value of 1229 cm^{-1}. Chiş *et al.* observed ν(C-O) at 1287 cm^{-1} for 2-naphthalenol [225]. Also, C=C ring vibration is seen in this region by other authors [226, 227]. The band at 1277 cm^{-1} occurs from the contribution of stretching of the C=C bond of phenyl and C-C bond of six-membered caged cyclic ring. The theoretical calculation yields this mode at 1250 cm^{-1}. A strong band at 1303 cm^{-1} is assigned to the CH deformation mode based on the DFT calculated value at 1289 cm^{-1}. A medium band at 1333 cm^{-1} is predominantly due to C=C ring stretching vibration as revealed by our PED calculation. The C=C ring vibrations around 1300 cm^{-1} were observed for many compounds [223, 228, 229]. Wagging of CH_2 appears at 1351 cm^{-1} whose theoretical predicted value is 1343 cm^{-1}. Recently, we reported this mode in the range 1330 - 1360 cm^{-1} [224] which is also supported from different research group [230]. Scissoring of the methylene group occurs at 1450 ± 10 cm^{-1} [178]. We observe a band of medium intensity at 1443 cm^{-1} which has a major contribution from CH_2 scissoring. Corresponding theoretical peak is well reproduced at 1437 cm^{-1} which is in consonance with reported value [227, 228]. PED calculation shows a small contribution of this group vibration at 1462 and 1510 cm^{-1} which couples with other modes. The 1462 cm^{-1} band has a contribution from in-plane N-H bending, well supported from literature [231–233]. The 1510 cm^{-1} has contribution from the C-N ring stretching vibration. The simulated frequencies of these modes are at 1478 and 1497 cm^{-1} respectively. A medium intensity band at 1547 cm^{-1} is mainly due to C=C ring stretching with a small contribution from O-H in-plane bending as perceived by PED calculation.

While O-H bending vibration was noticed by Chiş *et al.*, C=C ring stretching vibration was also observed previously [226, 234] in this region. Two strong bands at 1611 and 1623 cm^{-1} appeared in calculation suggest that these should be assigned to the intense bands at 1577 and 1596 cm^{-1}. According to the PED calculation the mode at 1577 cm^{-1} is mainly due to C=C ring stretching coupled with C=N stretching vibration. The prominent band at 1596 cm^{-1} arises from the C=N stretching. The assignment of C=N stretching was further confirmed from the observation by Chandran *et al.* [235].

5.3.2 Effect of Cu^{2+} on Raman spectrum

In the presence of Cu^{2+} we see a band around 620 cm^{-1} which is assigned to the Cu-O stretch and confirms the biding occurs through oxygen atoms see Figure 5.3. Here we have analyzed the spectrum of the complex form in the range 950-1650 cm^{-1} which shows prominent peaks and will be useful for marker bands of the Cu-bound form (see Figure 5.4). A detailed band assignments have been given in Table 5.2 .

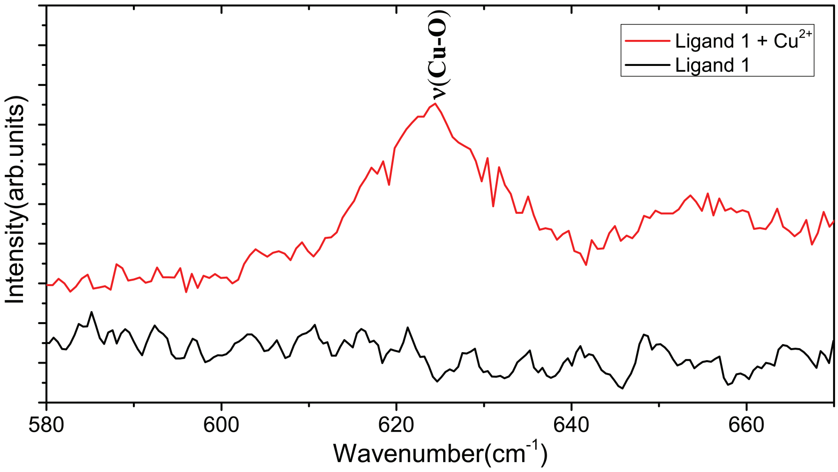

Figure 5.3: Raman spectrum of Ligand **1** in free and Cu^{2+} bound form.

In the presence of Cu^{2+} ion the spectrum changes drastically. Similar behavior was

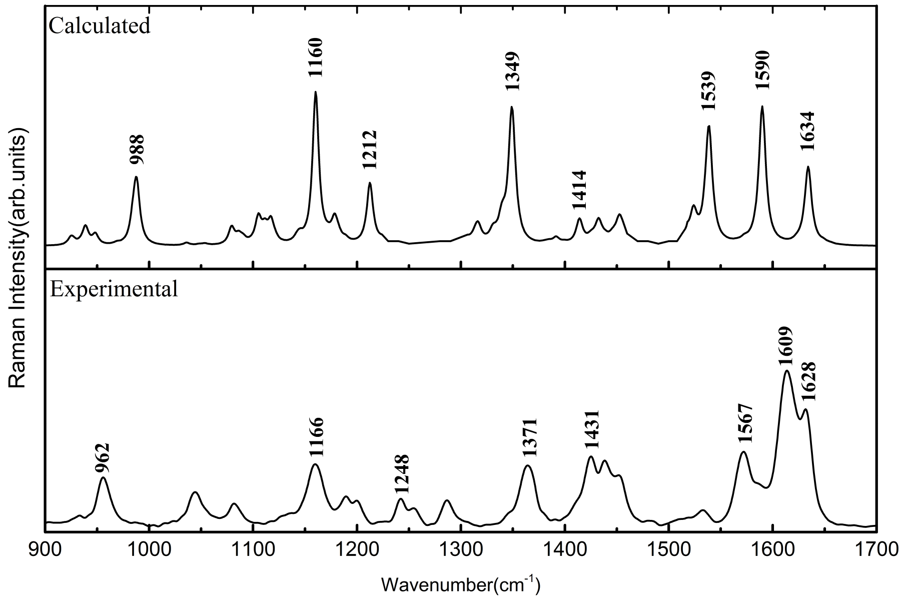

Figure 5.4: Experimental and calculated spectra of complex with Cu^{2+}.

observed for 4-Methylimidazole complexes with metal ion by Hasegawa *et al.* [216] and attributed to redistribution of various vibrations. A band of strong intensity appears at 962 cm^{-1} upon Cu^{2+} binding. According to PED calculation this band is assigned to N-N stretching. Two medium intensity bands at 1051 and 1089 cm^{-1} appear in the complex form which are ascribed to CH_2 twisting vibration. Theoretically calculated value of these modes are 1105 and 1117 cm^{-1} respectively. A strong band at 1166 cm^{-1} and medium band at 1196 cm^{-1} appears in the complex form. In the metal free form, we observe two bands in the same region. However, PED calculation reveals that the nature of the modes has changed in the complex form. The band at 1166 cm^{-1} is mainly due to in-plane N-H bending, C=O deformation and C-N stretching of urea group. The N-H bending was observed in this region by Hasegawa *et al.* [216] for Zn-bound 4-Methylimidazole. The band at 1196 cm^{-1} is due to in-plane C-H bending and CH_2 twisting. The 1196 cm^{-1} band is split into two bands probably due to intermolecular

Table 5.2: Raman shift (cm^{-1}) and assignment of vibrational modes of complex with Cu^{2+}

Calc. Raman (scaled) cm^{-1}	Relative Intensity	Expt. Raman cm^{-1}	Assignments (PED)
988	34	962 m	ν(N-N) (41)
1105	17	1051 w	τ (CH_2) (38)
1117	14	1089 w	τ (CH_2) (36)
1160	100	1166 m	ν(C=N) U (17), β(N-H) (40), β(OCN) (20)
1178	14	1196 w	β(C-H) (10), τ (CH_2)(10)
1212	39	1248 w	ν(C-N) ring (11), ω (CH_2) (24), β(C-H) (18)
1317	8	1293 w	β(C-H) , β(N-H)
1349	82	1371 m	ν(C=C) ring (16)
1414	17	1431 m	σ (CH_2) (51)
1432	14	1446 m	σ (CH_2) (66)
1452	15	1459 m	ν(C=C) ring (10), β(C-H) (15)
1524	19	1528 w	σ (CH_2) (30)
1539	78	1567 m	ν(C=C) ring (16), ν(C=C)(16)
1590	97	1609 s	ν(C=O) U (16), ν(C-N) U (16), ν(C-C)(16)
1634	56	1628 s	ν(C-N) U (40), β(N-H) (12)

Abbreviations: ν - stretching; β - in plane bending; ω - wagging
s-strong; m-medium; w -weak; σ - scissoring τ - twist; U - Urea

interaction in the solid form. The band at 1248 cm^{-1} is attributed to the wagging of CH_2 and in-plane bending of C-H. The corresponding theoretically calculated mode appears at 1212 cm^{-1}. The band at 1303 cm^{-1} in the metal free form appears at 1293 cm^{-1} upon complex formation. Apart from the C-H bending this mode has contribution from N-H bend also. The C=C ring stretching vibration which occurs at 1333 cm^{-1} in the metal free form, has blue shifted to 1371 cm^{-1} and also gain in intensity. The assignment of this band was confirmed by the study of Mrozek *et al.* [236] on metal bound benzonitrile. The mode is well reproduced in our DFT calculation at 1349 cm^{-1}. The

CH_2 scissoring appears at 1431, 1446 and 1528 cm^{-1} in the complex form. The corresponding theoretical values are 1414, 1432 and 1524 cm^{-1} respectively. The change in their position compared to the metal-free form can be explained by differences in the contribution of these vibrations to the corresponding modes as seen by PED calculation. A strong band appears at 1567 cm^{-1} is assigned to C=C and benzylic C-C stretching. C=C ring stretching vibration in the following region was reported earlier for metal bound complexes [216, 237]. This mode appears in our theoretical calculation at 1539 cm^{-1}. Two strong bands appear at 1609 and 1628 cm^{-1} which occurs mainly due to the urea group as shown by PED calculation. The contribution of urea group vibration was absent in metal-free form. A very strong mode appears at 1609 cm^{-1} upon Cu^{+2} binding. According to the PED calculation this mode is due to C=O and C-N stretching of urea group and due to C-C stretching. The assignment agrees well with the metal bound vibrations from literature [224]. It is the most prominent marker band for Cu^{+2} binding. Theoretical calculation provides this band at 1590 cm^{-1}. The strong band at 1628 cm^{-1} occurs due to C-N stretching of urea and in-plane N-H bending. Its theoretically calculated value is well reproduced at 1634 cm^{-1}. Thus, the close match of the experimentally obtained spectrum with the theoretically calculated one of the ligand in metal bound form supports the proposed Cu^{2+} binding mechanism.

5.3.3 SERS studies of compound 1 and the effect of metal binding

SER spectrum of compound 1 closely resembles that of the complex form with Cu^{2+} with some variation in the relative intensity (see Figure 5.6). This indicates the binding of compound **1** on the AgNP surface is similar to that of the Cu^{2+} ion. An appearance of strong peak around 242 cm^{-1} in the SER spectrum (see Figure 5.5), which can be assigned as Ag-O stretching vibration, further suggests that the **1** binds to the AgNP through phenolic oxygen. As the Cu^{2+} concentration increases this band decreases in intensity further support that binding of the ligand occurs through the same cite for both Cu^{2+} and silver surface.

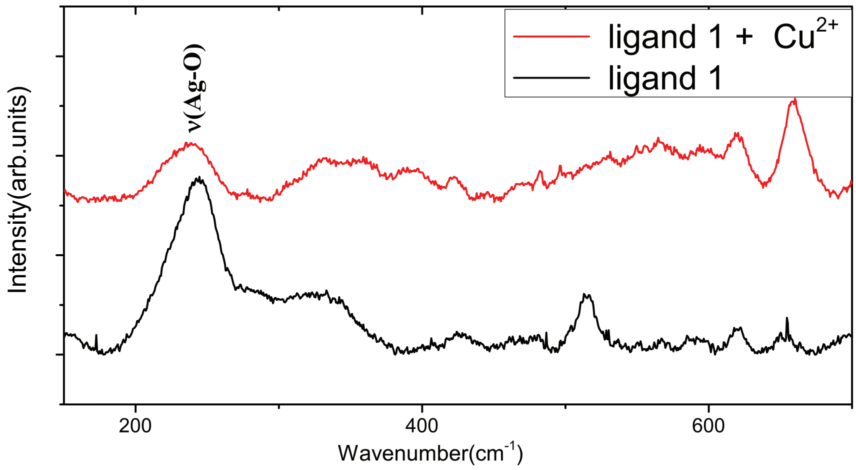

Figure 5.5: SERS spectra in the absence and presence of Cu^{2+}.

The similarities in the spectra of complex with Cu^{2+} and SERS lead us to assign the SERS band as shown in Table 5.3.

The appearance of the peaks in the SERS can be useful to predict its orientation on the surface by virtue of surface selection rule [135, 136]. The appearance of the strong band at 1629 cm^{-1} in the SER spectrum due to C=N stretching and in-plane N-H bending suggests that the molecule is upright on the silver surface. However the peak at 1052 cm^{-1} due to twisting of the methylene group indicates slightly tilted orientation on the surface. To monitor the effect of Cu^{2+} on the SER spectrum, we varied the concentration of the metal ion starting from 5 μM keeping the concentration of **1** fixed at 5 μM. We do observe sudden changes in the relative intensity of peaks in the presence of

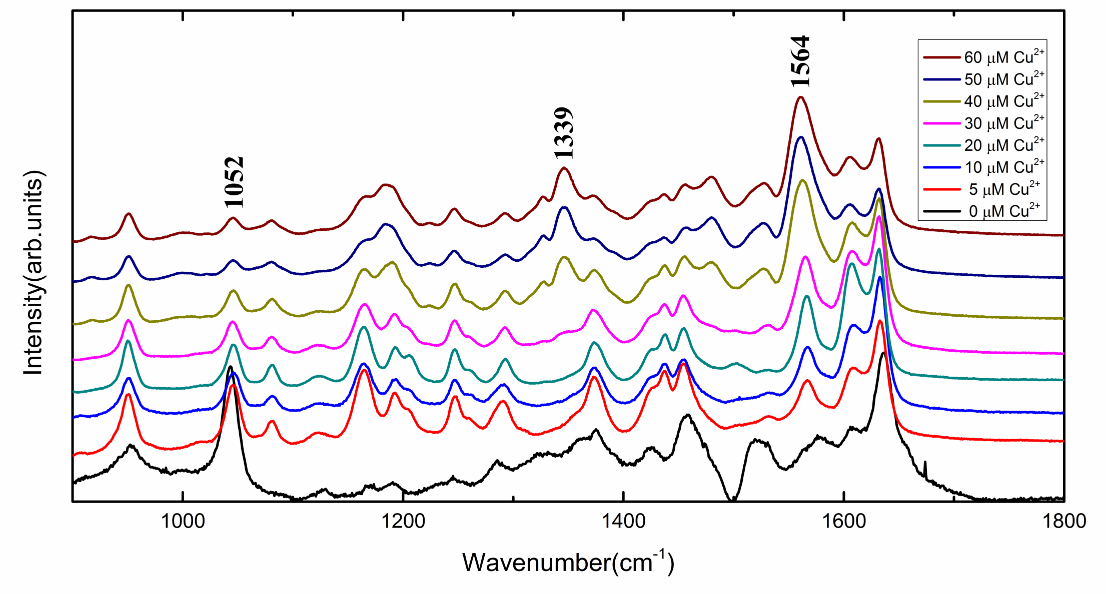

Figure 5.6: SER spectra of ligand **1** (5 μM) in the presence of different concentration of Cu^{2+} (0-60μM).

Table 5.3: Tentative band assignments of SERS of compound **1**

SERS bands (cm^{-1})	Assignments
961	ν(N-N)
1052	τ (CH_2)
1086	τ (CH_2)
1169	ν(C=N) U , β(N-H) , β(OCN)
1196	β(C-H), τ (CH_2)
1247	ν(C-N) ring, ω (CH_2), β(C-H)
1286	β(C-H) , β(N-H)
1368	ν(C=C) ring
1421	σ (CH_2)
1450	ν(C=C) ring, β(C-H)
1463	ν(C=C) ring, β(C-H)
1525	σ (CH_2)
1564	ν(C=C) ring, ν(C-C)
1604	ν(C=O) U, ν(C=N) U), ν(C-C)
1629	ν(C-N) U, β(N-H)

Abbreviations: ν - stretching; β - in plane bending; ω - wagging; σ - scissoring τ - twist; U - Urea

Cu^{2+} ion. As we increased the concentration of Cu^{2+} the variation of relative intensity continued to take place. At a concentration of 30 μM of Cu^{2+} a new peak at around 1339

cm^{-1} has emerged (see Figure 5.6). We continued to vary Cu concentration up to 60 μM, beyond that point the changes are almost unnoticeable. The variation in the spectra in the presence of Cu^{2+} ion can be attributable to the changes in both geometrical and electronic structures upon metal binding. Also the complex would be expected to be adsorbed in a different way on the AgNP surface resulting in the observed changes. Detailed analysis of the SER spectra of the complex with variable amount of Cu^{2+} ion reveals that the most notable change brought about by the metal ion is the intensity of the peak at 1564 cm^{-1}. This band is due to C=C ring stretching. Upon complexation, because of the resonance donation from oxygen and nitrogen the electron population of one of the C=C would increase, enhancing the intensity of this band. The intensity of this band kept on increasing with the amount of Cu^{2+} added hinting at a correlation between the two. To quantitatively find a relation we have chosen a band at 1052 cm^{-1} attributable to CH_2 twist as an internal standard, since this band did not change its position or shape on Cu^{2+} binding. Both the bands were fitted assuming a Lorentzian shape and the intensity ratio $\mathrm{I}_{1564}/\mathrm{I}_{1052}$ is plotted against the Cu^{2+} concentration (see Figure 5.7).

As can be seen from the figure, the intensity ratio can be used to determine the concentration level of Cu^{2+} in the range 5-50 μM. We performed the experiment with other metal ions such as Co^{2+}, Ni^{2+}, Mg^{2+}, Na^{+}, Cd^{2+}, Hg^{2+} and Ag^{+} at concentration of 40 μM each and compared with the result of Cu^{2+} at the same concentration. As can be seen from Figure 5.8 (red bars), the intensity ratio of those peaks for other metals are much less compared to Cu^{2+} response. These results corroborate well with the experiments performed earlier [215] which shows smaller changes in the absorption spectra in the presence of other metal ions compared to Cu^{2+} response.

Furthermore to show the selectivity of the ligand **1** for Cu^{2+} binding we have studied the effect of Cu^{2+} ion on the SER spectra in the presence of other metal ions. For this experiment, 8.0 equivalent of the Cu^{2+} were mixed with 8.0 equivalent of other metal ions seperately. The intensity ratio of the above mentioned peaks in the presence of various interfering metal ions did not show any significant change in the value (see Figure 5.8 (black bars)) compared to the presence of Cu^{2+} alone. These results are substantiated by the previous study [215] employing absorption spectroscopy.

This elucidates the selectivity to the Cu^{2+} binding and could be an effective method to detect Cu^{2+} ion. Thus we have developed a SERS based strategy to selectively detect and quantitatively determine the amount of Cu^{2+} ion below the maximum allowable limit set by the EPA in drinking water.

Furthermore, since the binding of **1** only with Cu^{2+} ion shifts the absorbance to

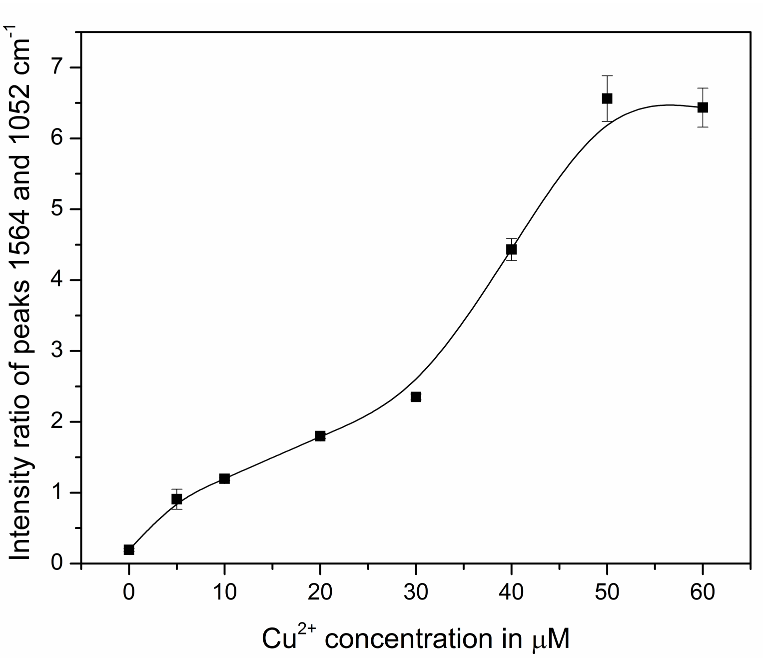

Figure 5.7: Plot of I_{1564}/I_{1052} as a function of Cu^{2+} concentration (error bars show the standard deviations calculated for 5 experiments).

the NIR region, by using an excitation frequency in that part, and choosing suitable plasmonic nanoparticle one can resonantly enhance the signal of the ligand in the Cu^{2+} bound form, thus increasing its detection and selection capability. This raises the possibility of extending the method in living cell [23, 238, 239] where the marker bands for the Cu^{2+} bound form of ligand **1** as revealed by our study will be useful to track the Cu^{2+} bound ligand. Imaging cell by NIR laser will suppress the fluorescence appearing from the components of the cell, furthermore, it will have less adverse effect on the cell with greater penetration depth. Thus the distribution of Cu^{2+} inside a living cell can be traced by NIR-SERS method with greater specificity and improved lateral resolution by two orders of magnitude smaller than the diffraction limit [131, 240].

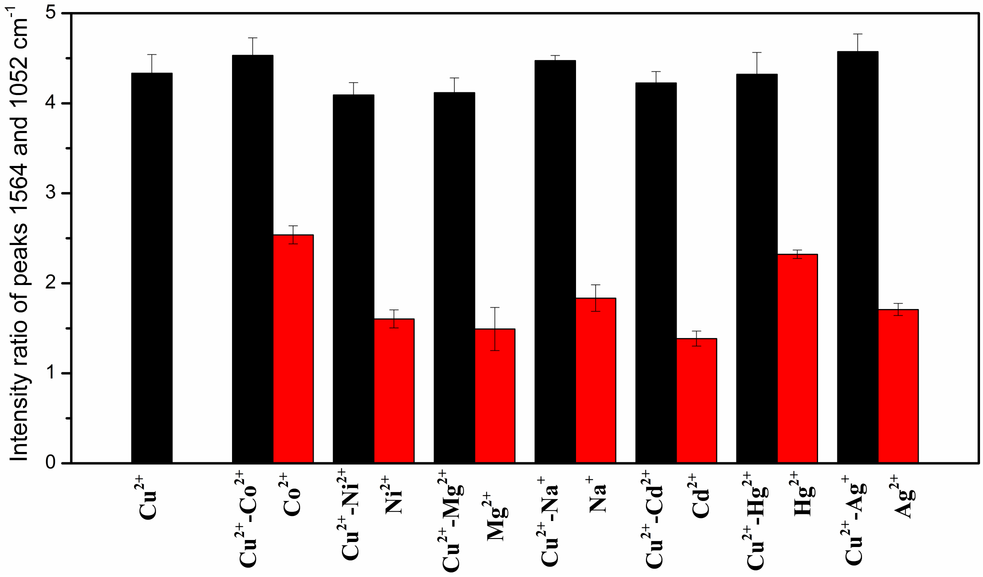

Figure 5.8: Selectivity of the Cu^{2+} detection method. Black bars represent the ratio I_{1564}/I_{1052} (concentration 5 μM) in the presence of 40 μM Cu^{2+} and other interfering metals at equimolar concentration. Red bar shows the ratio I_{1564}/I_{1052} of the other metals alone. Error bars show standard deviation.

Disadvantage of SERS

Although SERS has many advantages over other methods, one should keep in mind some of its limitations. First of all, in order to achieve high enhancement the sample needs tobe adsorbed onto the SERS-substrate whixh is not always possible. Secondly, the analyte may be photodegraded under the laser exposure and Raman modes are not seen. In addition, Raman is an expensive tool.

5.4 Conclusions

In summary, we have reported the Raman spectra of compound **1** in its free and Cu^{2+} bound form for the first time. The assignments of the vibrational bands have been carried out with the aid of DFT calculation. A good agreement between the experimentally obtained spectra with the theoretically calculated ones shows first direct evidence of the mechanism of Cu^{2+} binding predicted previously. The marker bands for the complex formation have been identified. The close match of the spectrum between the complex form and SER assists in tentative assignment of the SER bands of the compound. Furthermore, we have developed a SERS-based technique for selective detection and quantitative determination of Cu^{2+} ion up to a value less than the maximum admissible limit as suggested by EPA. Since this ligand has the characteristic absorbance in the NIR region only in the presence of Cu^{2+} ion, by using NIR-SERS one can resonantly enhance the Cu^{2+} bound ligands exclusively, thus increasing the selectivity further. Moreover, since the penetration depth of the NIR excitation is high, and the other molecules present in cell do not possess any absorption in that region, which opens up the possibility for imaging of Cu^{2+} in the living cell.

CHAPTER 6

Raman, IR and DFT studies of mechanism of Sodium binding to urea catalyst §

6.1 Introduction

Lately, hydrogen-bond catalysis has been developed as a substitute to Lewis acid catalyzed reactions. Many catalysts including several peptides have been reported to trigger Lewis basic reactants [241–247]. It is well realized that acidity of the hydrogen bond donor assumes a paramount part in determining the turn over frequency and the selectivity of the catalyst [248–250]. Furthermore the conformation of the catalyst also plays a role in regulating the selectivity [251–256]. A novel bis-camphorsulfonyl urea was reported by us of late as a highly acidic hydrogen bond catalyst [74]. To assess the activity of this catalyst we used it in a well studied Friedel-Crafts reaction of nitroalkenes [257–264]. It turned out that the enantioselectivity of this reaction is governed by the presence of $NaBPh_4$ as an additive. Face selection is changed in the presence of $NaBPh_4$, which enhanced the enantioselectivity .

The addition of other alkali metal salts did not have any impact on the enantioselectivity. A rapid background reaction was noticed in the case of more Lewis acidic magnesium salt. We speculated that the $NaBPh_4$ was binding the Lewis basic sites on the catalyst and effecting a change in the conformation that lead to the observed improvement in selectivity (see Scheme 6.1). The sodium complex ended up being inad-

---

[§] Based on this chapter work, two manuscripts are under preperation, Partha P. Kundu, G. Kumari, A. Chittoory, S. Rajaram and C. Narayana.

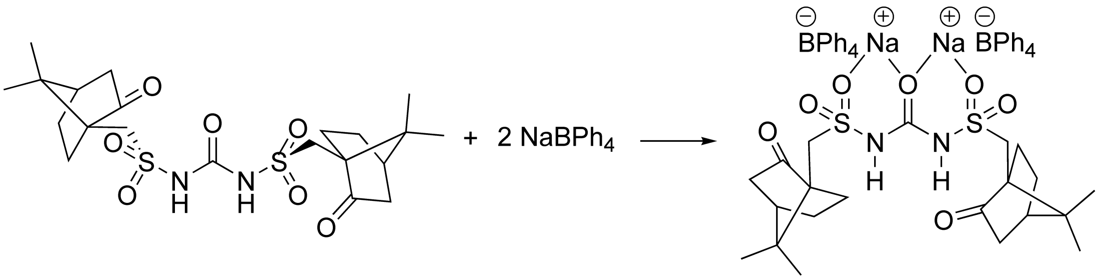

Scheme 6.1: Proposed change in conformation due to sodium binding.

equately soluble and attempts at acquiring single crystals suitable for X-ray diffraction studies failed. Since IR and Raman spectroscopy does not require a sample to be in crystal form, it is an ideal tool for understanding the location of binding in such case. So as to comprehend the part of $NaBPh_4$ in this reaction, we compared the structure of catalyst and complex by IR and Raman spectroscopy. To gain insights into the observed changes in the spectra we carried out ab initio DFT calculations of the catalyst in its free and Na^+ bound form.

6.2 Methods

6.2.1 Experimental section

All Raman measurements have been performed in the 180° backscattering geometry, using diode pumped frequency doubled Nd:YAG (model GDLM-5015 L, Photop Suwtech Inc., China) solid state laser as a excitation source. The spectrometer comprises of SPEX TRIAX 550 monochromator and a liquid nitrogen cooled charge-coupled device (CCD; Spectrum One with CCD 3000 controller, ISA Jobin Yovn). A holographic 1800 grooves mm^{-1} grating was used along with the 200 μm spectrograph entrance slit setting, providing $\sim$ 2 cm^{-1} resolution. A 50 $\times$ infinity-corrected objective (Nikon L Plan, Japan, NA 0.45) was used. The laser power used at the sample was 2 mW and the typical accumulation time was 180 s. All the spectra were background corrected and smoothed using 5 point FFT filter technique using Origin software. Lorentzian-profiles were fitted for spectral analysis. IR spectra were recorded on a Bruker IFS 66v/S spectrophotometer with KBr pellets containing the sample in the region 400 4000 cm^{-1}. Background was subtracted using OPUS software.

6.2.2 Computational methods

All the quantum chemical calculations have been performed at the density functional theory (DFT) level as employed in Gaussian 09 (G09) suite of program [90]. In order to take into account the effect of the intermolecular interaction present in solid, we have considered a dimer of the catalyst. The initial orientation of the dimer was taken from the crystal structure and subsequently geometry optimization was performed using Becke three-parameter hybrid-exchange functional [49] and Lee, Yang and Parr (B3LYP) gradient corrected correlation functional [48]. 6-31G (d,p) basis set is employed for such calculation. Harmonic vibrational frequencies were calculated on the optimized geometry using the same level of theory. The absence of any negative frequency confirms that the geometry corresponds to the local minimum at the potential energy surface. In order to compare the spectral change of the catalyst upon Na^{+} binding, we considered monomer of the solid urea catalyst. Catalyst with its free and bound form were optimized with the same level of theory as mentioned. In all the cases a dual scaling factor was used for the calculated vibrational frequencies, where frequencies below 1000 cm^{-1} were not scaled, whereas that above 1000 cm^{-1} were scaled with 0.961 [217]. The output of the Gaussian provide the Raman activities. In order to match with the experimental spectra, these are converted to Raman intensity [91–93]. The potential energy distribution (PED) calculation was performed by VEDA program [94]. Natural bonding orbital (NBO) calculation has been carried out by NBO 3.1 program [95].

6.3 Results and Discussion

6.3.1 Vibrational assignments

The optimized dimer of the urea catalyst is shown in Figure 6.1. The experimental and simulated IR and Raman spectrum are shown in Figure 6.2 and Figure 6.3 respectively. The assignments of the IR and Raman bands are given in Table 6.1 and Table 6.2 respectively.

The antisymmetric and symmetric stretching modes of SO_2 appear in the range 1300-1360 and 1130-1190 cm^{-1} respectively [265] and their positions depend on the electronegativity of the groups attached to them [219]. In IR these bands are very strong, while in case of Raman their intensity varies. [178]. In our compound, two strong bands at 1344 and 1139 cm^{-1} appeared in IR, which are assigned to ν_{as}(SO_2) and ν_s(SO_2). The calculated modes for these vibrations appear at 1293 and 1068 cm^{-1} respectively. The PED calculation shows that these modes are not pure and have contribution from other moieties. Based on our PED calculation we also observe two modes at 1282 and 1139 cm^{-1} which have small contribution from antisymmetric and symmetric stretching of SO_2. Theoretical values for these modes are at 1249 and 1083 cm^{-1} respectively. In Raman spectrum, a medium band at 1299 cm^{-1} and a weak band at 1112 cm^{-1} is assigned as antisymmetric and symmetric stretching of SO_2. The corresponding theoretically predicted values are 1249 and 1068 cm^{-1}. SO_2 stretching vibrations were reported at 1314, 1308, 1274, 1157, 1147 and 1133 cm^{-1} by Hangan et al. [266]. Chohan et al. [267] observed SO_2 stretching vibrations at 1345 and 1110 cm^{-1}. The scissoring and wagging vibration are expected in the range 570±60 and 520±40 cm^{-1} [265]. These are strong to medium in intensity. In IR we assign three modes at 512, 524 and 559 cm^{-1} to $\sigma(SO_2)$ which occur at 491, 537 and 566 cm^{-1} respectively in our theoretical calculation. In Raman this band appears at 524 cm^{-1} close to its theoretically calculated value (523 cm^{-1}). A band at 479 cm^{-1} in IR is assigned to wagging motion of SO_2 based upon our theoretically obtained value of 456 cm^{-1}. The assignments of these bands are further confirmed from literature [268, 269].

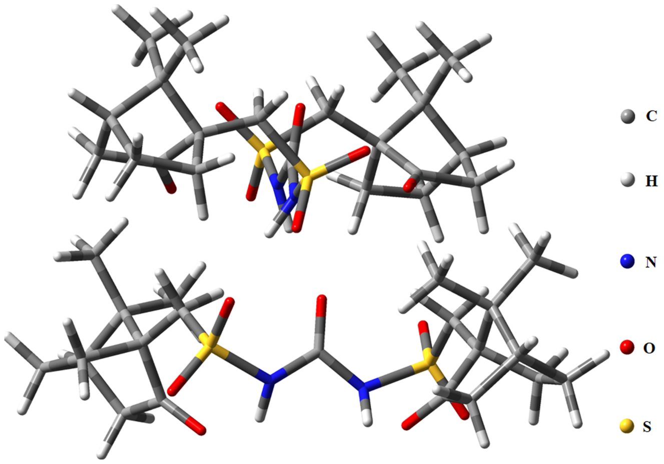

Figure 6.1: The optimized structure of urea catalyst in the dimer form.

Table 6.1: IR shift (cm^{-1}) and assignment of vibrational modes of urea catalyst

Calc. wavenumber (scaled) (cm^{-1})	IR intensity	Expt. IR (cm^{-1})	Assignments(PED)
441	61	468 w	$\Gamma(OCOS)$ (41)
456	65	479 m	$\omega(OSO)$ (10), $\Gamma(OCOS)$ (53)
491	24	512 w	$\sigma(OSO)$ (12), $\Gamma(HNCN)$ (31)
537	52	524 m	$\sigma(OSO)$ (28), $\Gamma(HNCN)$ (10)

Continued on next page

Table 6.1 – *Continued from previous page*

Calc. wavenumber (scaled) (cm^{-1})	IR intensity	Expt. IR (cm^{-1})	Assignments(PED)
566	181	559 m	$\sigma(OSO)$ (12), $\Gamma(HNCN)$ (12)
587	232	566 m	$\Gamma(HNCN)$ (58)
631	120	609 w	$\Gamma(HNCN)$ (37)
659	143	681 w	$\nu_{as}(S-N)$ (48)
711	48	730 m	$\nu(C-C)$ Cp(15)
718	75	740 w	$\beta(CCC)$ Cp (11)
763	156	767 m	$\nu(SC)$ (27), $\Gamma(ONCC)$ (30)
771	218	777 m	$\nu(SC)$ (28)
833	76	814 m	$\rho(CH_2)$ Cp
848	78	836 m	$\beta(NCO)$ (12), $\Gamma(HNCN)$ (13)
928	22	967 w	$\rho(CH_2)$ Cp
986	14	1027 w	$\rho(CH_2)$ Cp
1003	24	1051 m	$\nu(C-C)$ Cp (33)
1022	39	1068 m	$\rho(CH_2)$ Cp
1068	314	1139 s	$\nu_s(S=O)$ (76)
1083	272	1162 m	$\nu_s(S=O)$ (46)
1170	215	1200 m	$\nu_{as}(C=N)$ (26)
1177	160	1218 w	$\tau(CH_2)$
1249	98	1282 m	$\nu_{as}(S=O)$ (27), $\Gamma(HCCC)$ Cp (15)
1293	58	1344 s	$\nu_{as}(S=O)$ (37)
1378	170	1394 m	$\beta(HNC)$ (60)
1403	69	1417 w	$\beta(HNC)$ (32), $\sigma(CH_2)$ Cp (39)
1423	762	1455 m	$\nu(C-N)$ (11), $\beta(HNC)$ (55)
1442	441	1470 s	$\nu(C-N)$ (11), $\beta(HNC)$ (39)
	1633 br,m		$\beta(O-H)$ water
1698	320	1706 m	$\nu(C=O)$ U (77)
1748	285	1734 m	$\nu(C=O)$ Cp(89)
1768	259	1747 vs	$\nu(C=O)$ Cp (91)
2932	32	2886 m	$\nu_s(CH_3)$ Cp (93)
2953	21	2926 m	$\nu_s(CH_2)$ Cp ring (97)
2978	39	2944 m	$\nu(C-H)$ Cp ring (87)
2992	43	2960 m	$\nu_{as}(CH_3)$ Cp(80)
3016	21	2985 w	$\nu_{as}(CH_3)$ Cp (73)

Continued on next page

Table 6.1 – *Continued from previous page*

Calc. wavenumber (scaled) (cm^{-1})	IR intensity	Expt. IR (cm^{-1})	Assignments(PED)
3288	531	3169 br,m	$\nu(N-H)$ (97)
3355	477	3268 br,s	$\nu(N-H)$ (96)

Abbreviations: ν - stretching; β - in plane bending; Γ - torsion;
σ - scissoring τ - twist; ω - wagging; ρ -rocking
vs-very strong; s-strong; m-medium; w -weak; br - broad
Cp - Camphor; U- Urea
Subscripts : s-symmetric; as-antisymmetric

Table 6.2: Raman shift (cm^{-1}) and assignment of vibrational modes of urea catalyst

Calc. wavenumber (scaled) (cm^{-1})	Relative intensity	Expt. Raman (cm^{-1})	Assignments(PED)
104	21	113 m	$\Gamma(CSNC)$ (10)
192	23	198 m	$\Gamma(SONH)$
248	17	261 w	$\Gamma(CCCH)$ Cp
271	22	276 m	$\beta(OSC)$ (14)
289	25	290 m	$\Gamma(CNSO), \Gamma(HCCC)$ Cp
326	19	306 w	$\beta(CSN)$ (25)
348	6	326 w	$\Gamma(SNHO)$
379	11	362 w	$\Gamma(OCNS)$ (20)
400	9	399 m	$\beta(CCC)$ (27), $\Gamma(CCCC)$ (28) Cp
429	26	430 m	$\Gamma(CCCC)$ Cp (11)
472	27	484 m	$\Gamma(CCCC)$ Cp (21)
523	21	524 m	$\sigma(OSO)$ (53)
560	52	557 m	$\beta(CCC)$ Cp (15)
579	53	586 m	$\nu(CC)$ (10), $\Gamma(OCCC)$ (10) Cp
621	48	612 m	$\Gamma(HNCN)$ (14)
680	100	685 vs	$\nu(CC)$ (25) Cp

Continued on next page

Table 6.2 – *Continued from previous page*

Calc. wavenumber (scaled) (cm^{-1})	**Relative intensity**	**Expt. Raman (cm^{-1})**	**Assignments(PED)**
708	32	707 m	$\nu(CC)$ (12), $\beta(CCC)$ (10) Cp
748	42	769 s	$\nu(SC)$ (42)
791	20	786 m	$\rho(CH_2)$ Cp
831	6	837 w	$\beta(OCN)$ (15)
860	23	854 m	$\nu(CC)$ (40), $\Gamma(HCCC)$ (11) Cp
895	42	883 m	$\nu(SN)$ (30), $\beta(NCO)$ (10)
920	38	943 m	$\rho(CH_2)$, $\beta(NCO)$
953	14	972 m	$\nu(CC)$ (52) Cp
973	25	1005 m	$\nu(CC)$ (30) Cp
1001	17	1031 m	$\nu(CC)$ (30) Cp
1019	46	1053 m	$\nu(CC)$ (30) Cp
1045	13	1070 w	$\rho(CH_2)$ Cp
1068	13	1112 w	$\nu_s(SO_2)$ (76)
1076	20	1133 m	$\tau(CH_2)$ Cp
1092	41	1158 m	$\tau(CH_2)$ Cp
1112	24	1168 m	$\tau(CH_2)$ Cp
1137	20	1183 m	$\tau(CH_2)$ Cp
1181	11	1212 w	$\tau(CH_2)$ Cp
1200	32	1222 m	$\tau(CH_2)$ (54) Cp
1249	17	1299 w	$\nu_{as}(SO_2)$ (27), $\omega(CH_2)$ (15) Cp
1261	6	1306 w	$\omega(CH_2)$ (25) Cp
1290	22	1329 w	$\omega(CH_2)$ Cp
1305	15	1359 w	$\omega(CH_2)$ (21) Cp
1369	8	1380 w	$\delta_s(CH_3)$ (84) Cp
1403	24	1398 m	$\beta(HNC)$ (32), $\sigma(CH_2)$ (39) Cp
1414	30	1422 m	$\sigma(CH_2)$ (79) Cp
1440	50	1445 m	$\sigma(CH_2)$ (16), $\delta_{as}(CH_3)$ (42) Cp
1465	29	1467 m	$\delta_{as}(CH_3)$ (55) Cp
1484	19	1487 m	$\sigma(CH_2)$ (72) Cp
1698	33	1709 m	$\nu(C=O)$(77) U
1722	12	1728 w	$\nu(C=O)$(80) U

Continued on next page

Table 6.2 – *Continued from previous page*

Calc. wavenumber (scaled) (cm^{-1})	**Relative intensity**	**Expt. Raman (cm^{-1})**	**Assignments(PED)**
1768	20	1754 m	$\nu(C=O)$(91) Cp
2933	90	2923 vs	$\nu_s(CH_3)$ (90) Cp
2955	70	2936 vs	$\nu_s(CH_2)$ (90) Cp ring
2979	96	2963 vs	$\nu_s(CH_2)$ (68) Cp ring , $\nu(CH)$ (21) Cp ring
2994	53	2983 vs	$\nu_{as}(CH_2)$ (57) Cp ring
3020	25	3002 m	$\nu_{as}(CH_3)$ (63) Cp , $\nu_{as}(CH_2)$ (22) Cp ring

Abbreviations: ν - stretching; β - in plane bending; Γ - torsion;
σ - scissoring τ - twist; ω - wagging; ρ -rocking
vs-very strong; s-strong; m-medium; w -weak; br - broad
Cp - Camphor; U- Urea
Subscripts : s-symmetric; as-antisymmetric

The S-N stretching frequency appears in the region 905±70 cm^{-1} [265]. This band is generally weak in Raman [270]. On comparing our calculation which yields a band at 895 cm^{-1}, the weak band at 883 cm^{-1} is attributed to ν(S-N). In IR we observe contribution due to the ν(S-N) at 681 cm^{-1}. Alyar et al. [268] observe a small contribution from (S-N) stretching at 657 cm^{-1}. C-S stretching vibration depends upon the class of compound and their position varies in the range 590-735 cm^{-1} [178]. For methanesulfonamide derivatives in their solid form, this band appears in the 760-780 cm^{-1} region [271]. Two medium bands at 777 and 769 cm^{-1} appeared in the IR and Raman respectively are ascribed to C-S stretching bands. The position of these bands agrees well with our theoretical calculation, which predicts the respective modes at 771 and 748 cm^{-1},

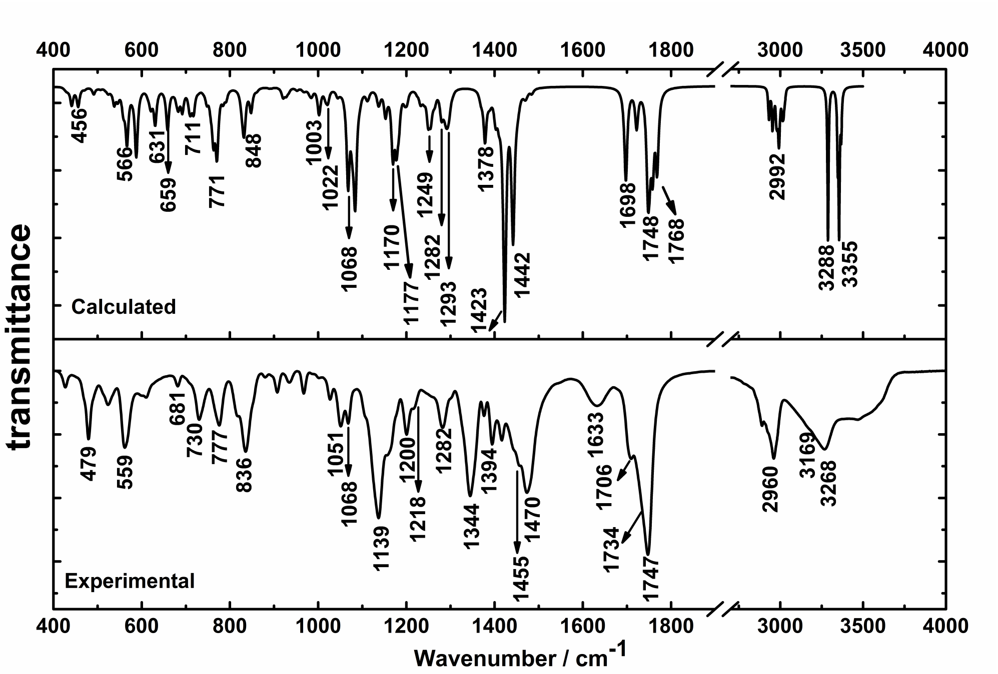

Figure 6.2: The experimental and theoretically calculated IR spectra of urea catalyst.

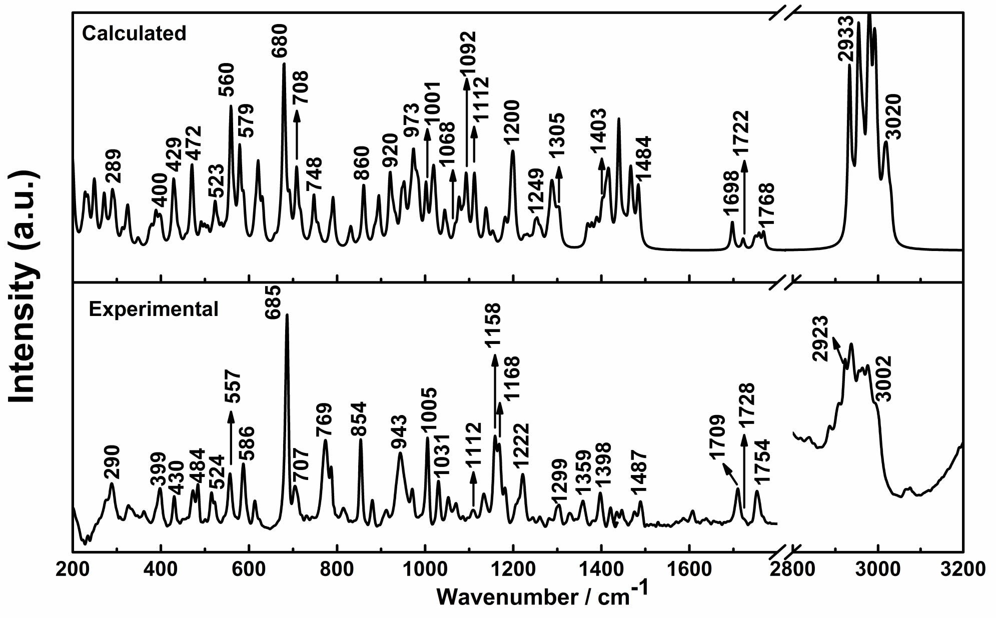

Figure 6.3: The experimental and theoretically calculated Raman spectra of urea catalyst.

and also with literature [268].

The C-N stretching mode appears as medium band at 1200 cm^{-1} in IR. Our DFT calculation predicts this band at 1170 cm^{-1}. PED calculation suggests that this mode mixes with other modes. Assignment of this vibration was also confirmed from literature [268, 269, 272–274]. Two broad bands at 3268 and 3169 cm^{-1} in IR are attributed to the N-H stretching of secondary amide. Baraldi et al. [275] observed this band at 3175 cm^{-1} and Ciurla et al. [220] assigned this band at 3236 cm^{-1} for compounds containing secondary amide. PED calculation indicates that these modes are almost pure. The in-plane N-H bend is expected to occur around 1400 cm^{-1} [231–233]. We observe this band at 1394, 1417, 1455 and 1470 cm^{-1} (IR) and at 1398 cm^{-1} (Raman). These assignments are further supported by the observation by Ciurla et al. [220] and Meganathan et al. [276]. These bands have contribution from camphor group and C-N stretching as seen from PED calculation.

Carbonyl group is often present in different classes of organic compounds. It possesses all the characteristics of producing good group frequency. It gives rise to strong band in IR owing to its large dipole moment derivative. Because of its large force constant, C=O stretching frequency appears out of the fingerprint region and does not have overlap from other modes. In organic compounds, carbonyl groups are generally bonded to the rest of the system by groups having lower frequency. This mismatch weakens the mechanical coupling, yielding almost a pure mode. The carbonyl stretching occurs in the range 1750 ± 150 cm^{-1} [178]. This mode is sensitive to the local environment, thus providing additional information about its surroundings. Our compound comprises of two different kinds of carbonyl groups, keto carbonyl of camphor ring and urea carbonyl. Thus it is important to distinguish their contribution in the spectrum. The position of these bands is governed by a number of factors such as mass of the adjacent atoms, their electronegativity, geometry and electronic structure (resonance and inductive effects) [178]. These effects may compete with each other and hence determining the position of such bands is not trivial and requires theoretical calculation. In IR spectrum we observe two strong bands at 1734 and 1747 cm^{-1} which is assigned to carbonyl stretching of camphor group. Theoretically predicted values of these modes are 1748 and 1768 cm^{-1}. In Raman, the contribution from camphor carbonyl appears at 1754 cm^{-1} as a medium band and the corresponding theoretical value is 1768 cm^{-1}. Assignment of these bands is further confirmed from literature [277, 278]. A band of medium intensity at 1706 cm^{-1} in IR is ascribed to C=O stretching of urea carbonyl, while its theoretical predicted value is at 1698 cm^{-1}. In Raman spectrum we see two bands, one at 1709 and another at 1728 cm^{-1} which are due to carbonyl stretching of urea, conforming to our DFT calculated values of 1698 and 1722 cm^{-1}. For similar compounds C=O vibration was seen to appear around 1700 cm^{-1} [220, 276]. All these modes are seen to be almost pure (contribution of 80 % or more in PED) as expected. Thus we could distinguish two different kind of C=O with the aid of our theory.

C-H stretching vibration in linear hydrocarbon compounds occurs in the range 2800-3000 cm^{-1}, with methyl group vibration in the range 2860 - 2970 cm^{-1} and methylene group vibration in the range 2840 - 2915 cm^{-1} [178]. For branched alkane, those value of wavenumbers change a little. Two bands at 2960 and 2985 cm^{-1} in IR spectrum are assigned as antisymmetric and a band at 2886 cm^{-1} is ascribed to symmetric stretching of methyl group. In Raman spectrum, we observe those modes at 3002 and 2923 cm^{-1}.

Our assignments are in well agreement with our calculation as well as literature value [232, 234, 279, 280]. The methylene symmetric stretching of C-H is observed at 2926 cm^{-1} (IR), and at 2936, 2963 cm^{-1}. In Raman spectrum, the antisymmetric stretching is observed at 2983 cm^{-1}. Rocking vibration of methylene group appears in the range 814 - 1068 cm^{-1} (IR) and 786 - 1070 cm^{-1} (Raman). In Raman we observe a series of bands in the range 1133 - 1222 cm^{-1} which are attributed to twisting of CH_2. This mode appears at 1218 cm^{-1} in IR. Wagging vibration of these groups appears in the range 1299 - 1359 cm^{-1} in Raman. Scissoring of methylene groups is observed in the 1398 - 1487 cm^{-1} range. antisymmetric and symmetric deformation of methyl group was found to be at 1467 and 1380 cm^{-1} in Raman. All these assignments are as expected [178, 219, 220, 268].

6.3.2 Effect of Na^+ binding on the optimized geometry

In order to perceive the effect of Na^+ on the structure, we considered a monomer form of the catalyst in free and Na^+ bound state. Based on our hypothesis [74], we added two Na^+ close to the oxygen of urea carbonyl and sulphonyl group and performed geometry optimization. Figure 6.4 shows the optimized structure of the catalyst and the complex. The numbering of atoms is shown in Figure 6.5. Table 6.3 summarizes the selected geometrical parameters of the catalyst in the free and Na^+ bound form.

As can be seen from Table 6.3, C=O bond length of urea carbonyl has increased (0.0328 Å) upon Na^+ binding. Metal binding shortened both the C-N bonds (0.012 - 0.015 Å) resulting in both the C-N bond length to be same. The distances of two N-H bonds of the urea group have seen to be increased ($\sim$ 0.012 Å) in the complex form.

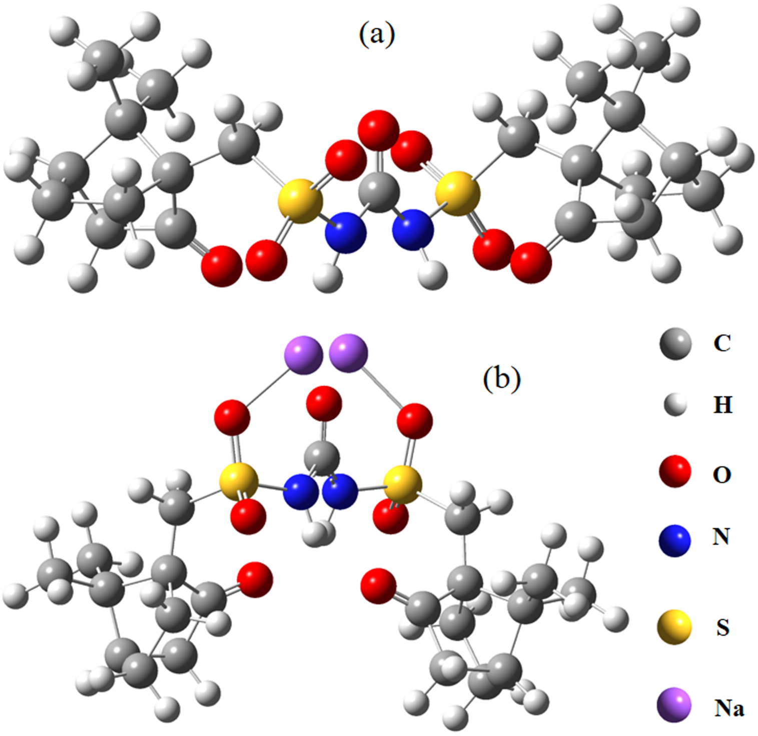

Figure 6.4: The optimized monomer structure of urea in its free (a) and Na^+ bound (b) form.

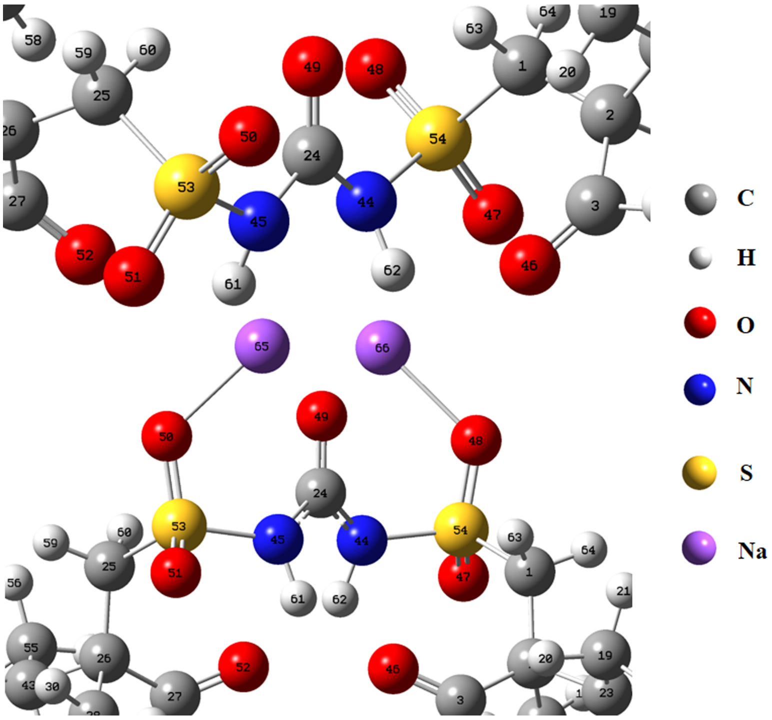

Figure 6.5: Numbering of atoms of urea in its free and metal bound form.

Table 6.3: Optimized bond lengths of the urea catalyst in its free and Na$^+$ bound form

Geometrical parameter	Urea catalyst	Complex	Difference
	Distance (Å)		
C24-O49	1.2209	1.2537	0.0328
C24-N45	1.3889	1.3769	-0.0120
C24-N44	1.3919	1.3769	-0.0150
N45-H61	1.0151	1.0268	0.0117
N44-H62	1.0154	1.0268	0.0114
S53-O50	1.4585	1.4809	0.0224
S53-O51	1.4630	1.4506	-0.0124
S54-O48	1.4588	1.4809	0.0221
S54-O47	1.4636	1.4506	-0.013
C27-O52	1.2134	1.2225	0.0091
C3-O46	1.2136	1.2225	0.0089

Na$^+$ binding to the catalyst causes the two sulphonyl groups equivalent. The S=O bond lengths of the sulphonyl bound to Na$^+$ have increased (by $\sim$ 0.022 Å) to 1.4809 Å and the free S=O bonds have decreased (by 0.012 - 0.013 Å) to 1.4506 Å. The C=O distances of the camphor group have increased by $\sim$ 0.01 Å upon metal binding.

6.3.3 Effect of Na$^+$ binding on the electronic distribution

Natural bonding orbital (NBO) analysis has been performed on urea in its free and bound form to see the change in atomic charges upon Na$^+$ binding (see Figure 6.5 for atom label).

As can be seen from Table 6.4 charges on both sulphonyl and carbonyl oxygen are decreased by $\sim$ 0.1 e and $\sim$ 0.14 e implying electron transfer from catalyst to metal. This results in decrease in charge on Na atom (see Table 6.4). The charge on the C24 atom of the urea carbonyl has increased by $\sim$ 0.02 e, where that of the sulfur atoms have decreased by $\sim$ 0.01 e. Both nitrogen atoms have gained charge ($\sim$ 0.01 e) as a result

Table 6.4: Atomic charges (e) by NBO analysis on urea catalyst and complex

	Urea catalyst	Complex	Difference
C 24	0.832	0.850	0.018
N 44	-0.923	-0.914	0.009
N 45	-0.922	-0.914	0.008
S 53	2.343	2.336	-0.007
S 54	2.346	2.336	-0.010
O 48	-0.923	-1.024	-0.101
O 49	-0.634	-0.773	-0.139
O 50	-0.926	-1.024	-0.098
Na 65		0.935	
Na 66		0.935	

of Na^+ binding. NBO analysis reveals that the occupancy of π^*(C=O) of urea increases upon Na^+ binding by $\sim$ 0.1 e. A gain in electron population in the anti-bonding orbital implies weakening of the bond [281], which is reflected in the elongation of bond length (see Table Table 6.3) and the decrease in wavenumber (see next section). The population of σ(S-O) orbital bound to Na^+ have decreased by $\sim$ 0.02 e which is in agreement with the increment of the corresponding bond lengths (Table 6.3). The decrement of C-N bond length can be attributed to the loss of electron population in the σ^* (C-N) orbital. The increase population of σ^* (N-H) orbitals causes two N-H bonds to lengthened.

6.3.4 Effect of Na^+ binding on vibrational frequencies

Figure 6.6 & Figure 6.7 shows the IR and Raman spectra of the catalyst, $NaBPh_4$, and the complex. As in the case of structure, comparison of vibrational frequency is made on the monomer of the urea catalyst in its free and bound form. Table 6.5 summarizes the calculated and observed frequencies, and assignments of modes of the urea catalyst and the complex that are sensitive to Na^+ binding.

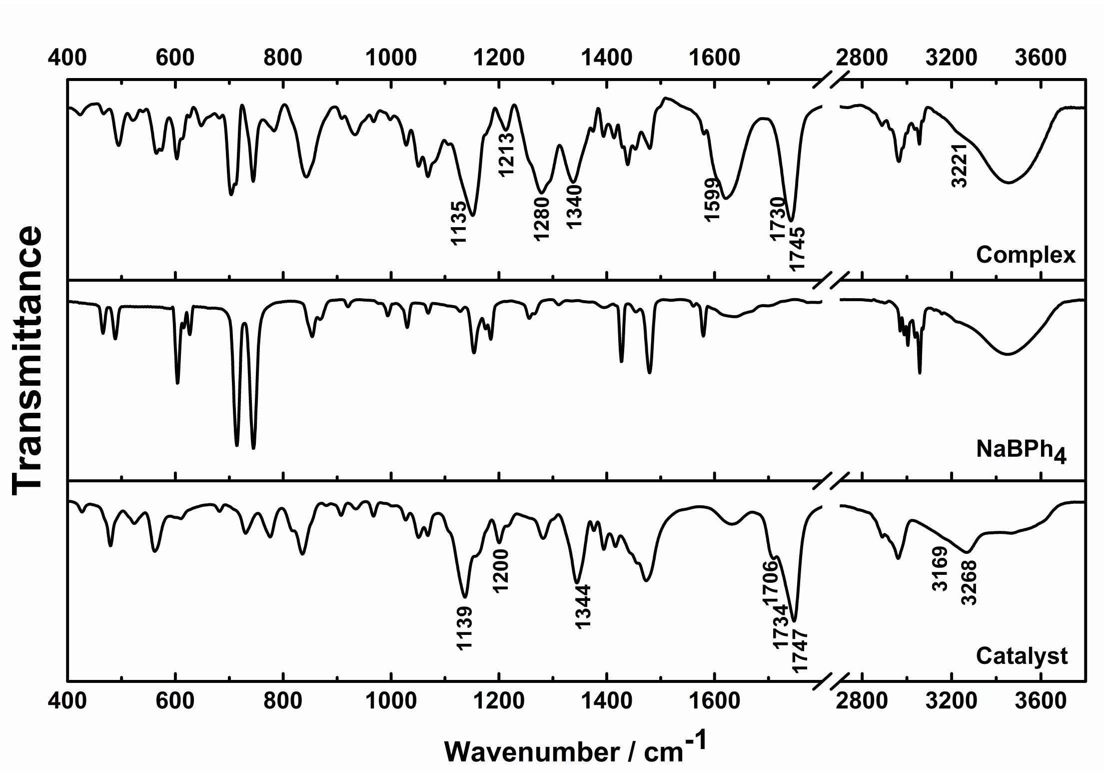

Figure 6.6: The experimental IR spectra of urea catalyst, $NaBPh_4$, and complex .

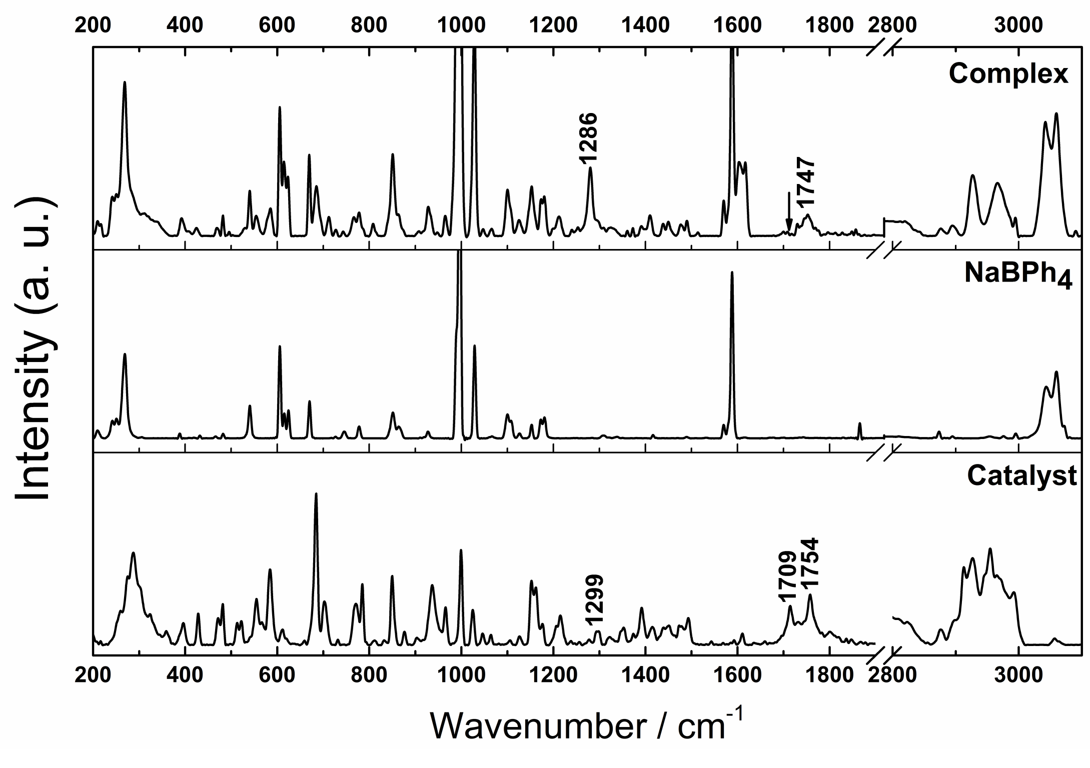

Figure 6.7: The experimental Raman spectra of urea catalyst, $NaBPh_4$, and complex .

Table 6.5: Selected vibrational frequencies (cm^{-1}) of the urea catalyst and the complex sensitive to the Na$^+$ binding

Urea catalyst		Assignments	Complex		Assignments
calculated	observed		calculated	observed	
		IR			
3452	3268	ν(N-H) (100)	3279	3221	ν(N-H) (99)
3444	3169	ν(N-H)(100)	3262	-	ν(N-H)(100)
1760	1734, 1747	ν(C=O) Cp (83)	1722	1730, 1745	ν(C=O) Cp (90)
1712	1706	ν(C=O) U (80)	1610	1599	ν(C=O) U (73), β(HNC) (18)
1303	1344	ν_{as}(S=O) (58)	1294	1340	ν_{as}(S=O) (69)
1163	1200	ν(C=N)(20)	1169	1213	ν(C-N)(27), β(HNC) (10)
1079	1139	ν_s(S=O)(33), β(HCC)(16)	1069	1135	ν_s(S=O)(77)
		Raman			
1760	1754	ν(C=O) Cp (83)	1732	1747	ν(C=O) Cp (90)
1712	1709	ν(C=O) U (80)	1610	~1600	ν(C=O) U (73), β(HNC) (18)
1290	1299	ν_{as}(S=O)(26), Γ(HCCC)(12)	1285	1286	ν_{as}(S=O)(67)

Abbreviations: ν - stretching; β - in plane bending; Γ - torsion;

Cp - Camphor; U- Urea

Subscripts : s-symmetric; as-antisymmetric

In IR spectrum N-H stretching frequency which appears at 3268 cm^{-1} has red-shifted to 3221 cm^{-1}. In calculation the shift is around 173 cm^{-1}. The disagreement in the absolute value may be due to the fact that calculated value of urea catalyst itself is overestimated. However, the trend of shift could be well reproduced in calculation and this shift is attributed to the increase in length of the N-H bond (see Table Table 6.3). Upon Na$^+$ binding a net positive charge is induced in the complex, resulting in the decrease in strength of the N-H bond [282]. The other N-H frequency which appears at 3169 cm^{-1} in urea catalyst could not be detected in the complex form because of the weak intensity. In IR, two bands at 1734 and 1747 cm^{-1} which are attributed to carbonyl stretching of camphor group shift to 1730 and 1745 cm^{-1}. Unlike in the case of dimer, calculation on monomer produces only one peak at 1760 cm^{-1} which shifts to 1722 cm^{-1} after Na$^+$ binding. In Raman, this mode shifts to 7 cm^{-1} downward, the predicted shift is 28 cm^{-1}. These shifts are in well agreement with the increase in C=O bond length (see Table Table 6.3) in the complex form. The increase in bond length can be attributed to the closeness of carbonyl group to the N-H group and forming intramolecular hydrogen bonds upon Na^+ binding. It is to be mentioned, that the shift is overestimated in our calculation. In IR, the mode assigned as ν(C=O) of urea at 1706 cm^{-1} disappeared and shifted to the O-H bending region of water in the complex. By fitting Lorentizan curves in that region for both the catalyst and complex, we could find an appearance of a new mode at around 1599 cm^{-1} which is assigned to C=O stretching of urea in the metal bound form. Surprisingly, the shift of 107 cm^{-1} is very close to the theoretically predicted value of 102 cm^{-1}. In Raman, the ν(C=O) mode of catalyst disappears in the complex form. The predicted shifted mode at 1610 cm^{-1} could not be detected in the complex spectrum because of the appearance of strong phenyl ring modes of the $NaBPh_4$ in that region. The decrease in C=O stretching frequency is reflected in the lengthening of the C=O bond distance(Table Table 6.3). C=O stretching frequency is known to be red-shifted upon metal binding and the amount of shift reflects the nature of bond (more sensitive to ionic than covalent bond) [283, 284]. SO_2 antisymmetric and symmetric stretching which appear at 1344 and 1139 cm^{-1} in IR spectrum of urea catalyst have down-shifted to 1340 and 1135 cm^{-1} in the complex form. The shift of 4 cm^{-1} of both the modes is in accordance with the predicted red-shift of 9 and 10 cm^{-1} respectively (see Table Table 6.5). In Raman spectrum, the SO_2 anti-symmetric stretch is red-shifted by 13 cm^{-1}, predicted value being 5 cm^{-1}. Symmetric SO_2 stretching is weak and falls in the region where contribution from counter-ion occurs. Thus, we could not detect any shift of this in the complex form. As can be seen from the optimized geometry of the catalyst in the Na^+ free and bound form, the S=O bond bound to Na^+ is lengthened, whereas other S=O bond is shortened (Table Table 6.3). In the bound form S=O stretching vibrations are mainly due to the contribution from the Na^+ bound S=O, as viewed by GaussView [285] visualization program. As this bond length increases upon metal binding, the decrease in wavenumber is expected. Down-shift of both SO_2 vibrations were observed in metal saccharinates compared to saccharine compounds [283].The C-N stretching vibration, has up-shifted by 13 cm^{-1} in the IR spectrum of complex which is in well agreement with the calculated value of 6 cm^{-1}. A slight decrease in C-N bond length can be accounted for this blue shift. Decrease in C-N bond length was also observed by Jovanovski et al. [286] for metal saccharinates. The observed changes in the infrared and Raman spectra upon complexation correlate with the DFT calculations. Mismatch between the theory and experimental value could most likely be due to the fact that in the calculation we considered a single molecule in gas phase. This overlooks the intermolecular interactions present in real system. The calculation could be possibly improved by the inclusion of the counter anion (tetraphenylborate), whose relative position with the catalyst is not known experimentally. As a control, we have also calculated the infrared spectra for other possible conformations (see Figure 6.8) using same level of theory. For conformation **1** the shift of C=O stretching of urea group is underestimated (shift of 79 cm^{-1} compared to the observed shift of 107 cm^{-1}). Also, the camphor C=O shifts by 57 cm^{-1} contrary to the experimental shift of only 4 cm^{-1}. This can be explained by the closeness of this group to the Na^+ in this conformation. For conformation **2** C=O stretch of urea is shifted by only 60 cm^{-1}. The shift of C=O stretching is overestimated (by 57 cm^{-1}), this time

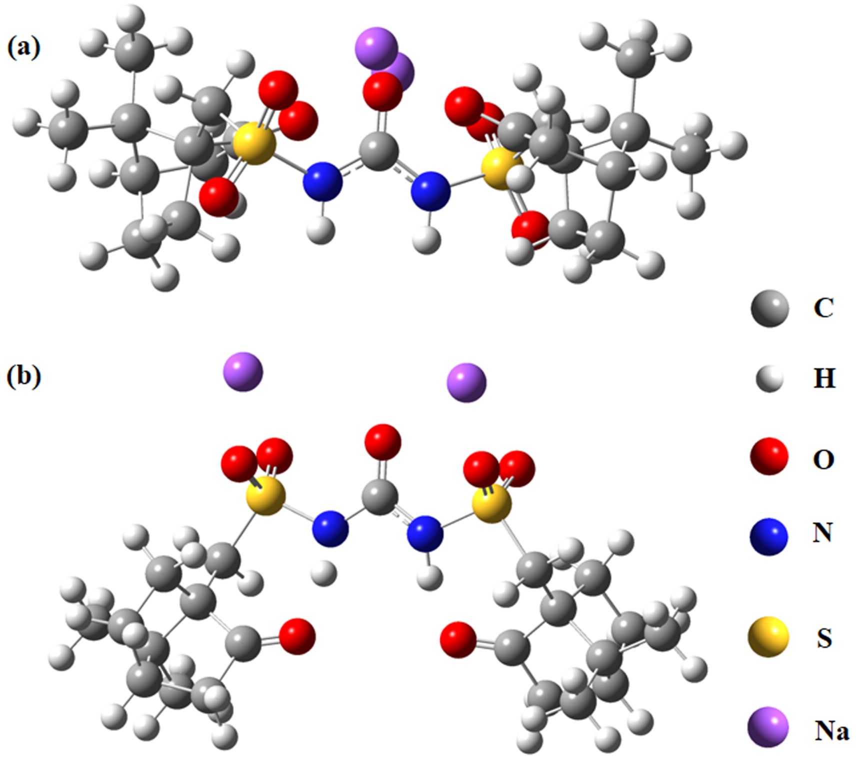

Figure 6.8: Optimized structure of two other possible conformations -conformation **1** (a) and conformation **2** (b) at B3LYP/6-31G(d,p) level.

due to the closeness of these groups to N-H. Furthermore, antisymmetric stretching of SO_2 is red-sifted by 101 m^{-1} contrary to the observed stretch of 4 cm^{-1}. A much better match was seen between the experimental and simulated spectra for the conformation shown in Figure 6.4. This substantiates our hypothesis that the sodium cation forms a complex through coordination of the oxygens on the urea carbonyl and sulfonyl groups.

6.4 Conclusions

In summary, we have assigned the bands appearing in the IR and Raman spectra with the help of DFT calculation. Considering a dimer of the urea catalyst, we obtained good agreement with the experimental value. It helps us to investigate the changes in vibrational spectra occurring in the complex form. In the complex form we observe changes happening in the stretching frequencies of sulphonyl and both keto and urea carbonyl group. We also observe changes occurring at C-N and N-H stretching frequencies. To understand those changes we have considered a monomer structure of the catalyst and its complex form and compared their calculated spectra. The trend observed in vibrational spectra could qualitatively reproduced in our calculation. The observed shifts in the spectra are also supported by the structural changes brought about by Na^+ binding. NBO calculation reveals the electronic redistribution upon Na^+ binding. Thus, our study helps in understanding the role of sodium in enhancing the enantioselectivity of the catalyst. Furthermore, the spectra in the complex form together with the assignments would serve as a reference spectra for studying binding mechanism of different substrate to this catalyst.

References

1. D.A. Long. *The Raman Effect: A Unified Treatment of the Theory of Raman Scattering by Molecules*. John Wiley & Sons Ltd, (2002).
2. Ricardo Aroca. *Surface-enhanced vibrational spectroscopy*. Wiley. com, (2006).
3. Eric Le Ru and Pablo Etchegoin. *Principles of Surface-Enhanced Raman Spectroscopy: and related plasmonic effects*. Elsevier Science, (2008).
4. Frank Jensen. *Introduction to Computational Chemistry*. Wiley, 2 edition (2006).
5. Jorge Kohanoff. *Electronic structure calculations for solids and molecules*. Cambridge University Press, (2006).
6. C.V. Raman and K.S. Krishnan. A new type of secondary radiation, *Nature* **121**, 501–502 (1928).
7. G Landsberg and L Mandelstam. A new occurrence in the light diffusion of crystals, *Naturwissenschaften* **16**, 557–558 (1928).
8. A Smekal. Naturwiss. 11, 873, (1923).
9. W. Kiefer. Recent Advances in linear and nonlinear Raman spectroscopy I, *Journal of Raman Spectroscopy* **38**, 1538–1553 (2007).
10. WW Coblentz. Investigations of infrared spectra,(Carnegie Institution of Washington, Washington, DC, 1905), *Vol. I, part* **1**, 45.
11. Friedrich Siebert and Peter Hildebrandt. *Vibrational Spectroscopy in Life Science*. Wiley-VCH Verlag GmbH & Co. KGaA, Weinheim, (2008).

12. Rajendrani Mukhopadhyay. Raman flexes its muscles, *Analytical Chemistry* **79**, 3265–3270 (2007).

13. MJ Pelletier et al. Quantitative analysis using Raman spectrometry, *Applied spectroscopy* **57**, 20A–20A (2003).

14. Wei E Huang, Mengqiu Li, Roger M Jarvis, Royston Goodacre and Steven A Banwart. Shining light on the microbial world: the application of Raman microspectroscopy, *Advances in applied microbiology* **70**, 153–186 (2010).

15. Danting Yang and Yibin Ying. Applications of raman spectroscopy in agricultural products and food analysis: a review, *Applied Spectroscopy Reviews* **46**, 539–560 (2011).

16. Lore Kiefert and Stefanos Karampelas. Use of the Raman spectrometer in gemmological laboratories: Review, *Spectrochimica Acta Part A: Molecular and Biomolecular Spectroscopy* **80**, 119–124 (2011).

17. Gwénola Sabatté, Ruth Keir, Margaret Lawlor, Murdo Black, Duncan Graham and W Ewen Smith. Comparison of surface-enhanced resonance Raman scattering and fluorescence for detection of a labeled antibody, *Analytical chemistry* **80**, 2351–2356 (2008).

18. Janina Kneipp, Harald Kneipp and Katrin Kneipp. SERSa single-molecule and nanoscale tool for bioanalytics, *Chemical Society Reviews* **37**, 1052–1060 (2008).

19. Mhairi M Harper, Kristy S McKeating and Karen Faulds. Recent developments and future directions in SERS for bioanalysis, *Physical Chemistry Chemical Physics* (2013).

20. Graeme McNay, David Eustace, W Ewen Smith, Karen Faulds and Duncan Graham. Surface-enhanced Raman scattering (SERS) and surface-enhanced resonance Raman scattering (SERRS): a review of applications, *Applied Spectroscopy* **65**, 825–837 (2011).

21. Laura Rodriguez-Lorenzo, Laura Fabris and Ramon A Alvarez-Puebla. Multiplex optical sensing with SERS. A critical review, *Analytica chimica acta* (2012).

22. Rebecca A Halvorson and Peter J Vikesland. Surface-enhanced Raman spectroscopy (SERS) for environmental analyses, *Environmental science & technology* **44**, 7749–7755 (2010).

23. Partha P. Kundu and Chandrabhas Narayana. Raman based imaging in biological application-a perspective, *J.Med.Allied.Sci.* **2**, 41–48 (2012).

24. M. Fleischmann, P.J. Hendra and A.J. McQuillan. Raman spectra of pyridine adsorbed at a silver electrode, *Chem.Phys.Lett.* **26**, 163–166 (1974).

25. David L. Jeanmaire and Richard P. Van Duyne. Surface raman spectroelectrochemistry: Part I. Heterocyclic, aromatic, and aliphatic amines adsorbed on the anodized silver electrode, *J.Electroanal.CHem* **84**, 1–20 (1977).

26. M Grant Albrecht and J Alan Creighton. Anomalously intense Raman spectra of pyridine at a silver electrode, *Journal of the American Chemical Society* **99**, 5215–5217 (1977).

27. David Pines. Collective energy losses in solids, *Reviews of Modern Physics* **28**, 184 (1956).

28. Craig F Bohren and Donald R Huffman. *Absorption and scattering of light by small particles*. Wiley. com, (2008).

29. G Mie. Articles on the optical characteristics of turbid tubes, especially colloidal metal solutions, *Ann. Phys* **25**, 377–445 (1908).

30. LD Landau and EM Lifshitz. Electrodynamics of Continuous Media, (rev. and enl., with LP Pitaevskii), (1984).

31. Andreas Otto. Surface-enhanced Raman scattering:‘classical’ and ‘chemical’ origins. in *Light scattering in solids IV*, 289–418. Springer (1984).

32. ZQ Tian. General discussions section, *Faraday Discuss* **132**, 309–319 (2006).
33. Llewellen H Thomas. The calculation of atomic fields. in *Mathematical Proceedings of the Cambridge Philosophical Society*, volume 23, 542–548. Cambridge Univ Press, (1927).
34. Enrico Fermi. A statistical method for the determination of some atomic properties and the application of this method to the theory of the periodic system of elements, *Z. Phys* **48**, 29 (1928).
35. Pierre Hohenberg and Walter Kohn. Inhomogeneous electron gas, *Physical review* **136**, B864 (1964).
36. Walter Kohn and Lu Jeu Sham. Self-consistent equations including exchange and correlation effects, *Physical Review* **140**, A1133 (1965).
37. John P Perdew, Jianmin Tao, Viktor N Staroverov and Gustavo E Scuseria. Meta-generalized gradient approximation: Explanation of a realistic nonempirical density functional, *The Journal of chemical physics* **120**, 6898 (2004).
38. Stefan Kurth, John P Perdew and Peter Blaha. Molecular and solid-state tests of density functional approximations: LSD, GGAs, and meta-GGAs, *International journal of quantum chemistry* **75**, 889–909 (1999).
39. John P Perdew, Adrienn Ruzsinszky, Jianmin Tao, Viktor N Staroverov, Gustavo E Scuseria and Gábor I Csonka. Prescription for the design and selection of density functional approximations: More constraint satisfaction with fewer fits, *The Journal of chemical physics* **123**, 062201 (2005).
40. Paul AM Dirac. Note on exchange phenomena in the Thomas atom. in *Mathematical Proceedings of the Cambridge Philosophical Society*, volume 26, 376–385. Cambridge Univ Press, (1930).
41. D Ceperley. Ground state of the fermion one-component plasma: A Monte Carlo study in two and three dimensions, *Physical Review B* **18**, 3126 (1978).

42. D. M. Ceperley and B. J. Alder. Ground State of the Electron Gas by a Stochastic Method, *Phys. Rev. Lett.* **45**, 566–569 (1980).

43. Seymour H Vosko, Ll Wilk and M Nusair. Accurate spin-dependent electron liquid correlation energies for local spin density calculations: a critical analysis, *Canadian Journal of Physics* **58**, 1200–1211 (1980).

44. John P Perdew and Alex Zunger. Self-interaction correction to density-functional approximations for many-electron systems, *Physical Review B* **23**, 5048 (1981).

45. Liangyou Fan and Tom Ziegler. The influence of self-consistency on nonlocal density functional calculations, *The Journal of chemical physics* **94**, 6057 (1991).

46. John P Perdew and Wang Yue. Accurate and simple density functional for the electronic exchange energy: Generalized gradient approximation, *Physical Review B* **33**, 8800 (1986).

47. Axel D Becke. Density-functional exchange-energy approximation with correct asymptotic behavior, *Physical Review A* **38**, 3098 (1988).

48. Chengteh Lee, Weitao Yang and Robert G. Parr. Development of the Colle-Salvetti correlation-energy formula into a functional of the electron density, *Phys. Rev. B* **37**, 785–789 (1988).

49. Axel D. Becke. Density-functional thermochemistry. III. The role of exact exchange, *The Journal of Chemical Physics* **98**, 5648–5652 (1993).

50. PJ Stephens, FJ Devlin, CF Chabalowski and Michael J Frisch. Ab initio calculation of vibrational absorption and circular dichroism spectra using density functional force fields, *The Journal of Physical Chemistry* **98**, 11623–11627 (1994).

51. John C Slater. Atomic shielding constants, *Physical Review* **36**, 57 (1930).

52. S Francis Boys. Electronic wave functions. I. A general method of calculation for

the stationary states of any molecular system, *Proceedings of the Royal Society of London. Series A. Mathematical and Physical Sciences* **200**, 542–554 (1950).

53. Michelle M Francl, William J Pietro, Warren J Hehre, J Stephen Binkley, Mark S Gordon, Douglas J DeFrees and John A Pople. Self-consistent molecular orbital methods. XXIII. A polarization-type basis set for second-row elements, *The Journal of Chemical Physics* **77**, 3654 (1982).

54. Michael J Frisch, John A Pople and J Stephen Binkley. Self-consistent molecular orbital methods 25. Supplementary functions for Gaussian basis sets, *The Journal of chemical physics* **80**, 3265 (1984).

55. Gernot Frenking, Iris Antes, Marlis Böhme, Stefan Dapprich, Andreas W Ehlers, Volker Jonas, Arndt Neuhaus, Michael Otto, Ralf Stegmann, Achim Veldkamp et al. Pseudopotential calculations of transition metal compounds: scope and limitations, *Reviews in Computational Chemistry, Volume 8* , 63–144 (1996).

56. Thomas R Cundari, Michael T Benson, M Leigh Lutz and Shaun O Sommerer. Effective core potential approaches to the chemistry of the heavier elements, *Reviews in Computational Chemistry, Volume 8* , 145–202 (1996).

57. Willard R Wadt and P Jeffrey Hay. Ab initio effective core potentials for molecular calculations. Potentials for main group elements Na to Bi, *The Journal of Chemical Physics* **82**, 284 (1985).

58. P Jeffrey Hay and Willard R Wadt. Ab initio effective core potentials for molecular calculations. Potentials for K to Au including the outermost core orbitals, *The Journal of Chemical Physics* **82**, 299–310 (1985).

59. P Jeffrey Hay and Willard R Wadt. Ab initio effective core potentials for molecular calculations. Potentials for the transition metal atoms Sc to Hg, *The Journal of Chemical Physics* **82**, 270–283 (1985).

60. Jack J Dongarra, Iain S Duff, Danny C Sorensen and Henk Van Der Vorst. *Solving linear systems on vector and shared memory computers*. Society for Industrial and Applied Mathematics, (1990).

61. Salim Abdali, Bram De Laere, Maria Poulsen, Mariam Grigorian, Eugene Lukanidin and Jörg Klingelhöfer. Toward Methodology for Detection of Cancer-Promoting S100A4 Protein Conformations in Subnanomolar Concentrations Using Raman and SERS, *J.Phys.Chem.C.* **114**, 7274–7279 (2010).

62. Aoune Barhoumi and Naomi J. Halas. Label-Free Detection of DNA Hybridization Using Surface Enhanced Raman Spectroscopy, *J.Am.Chem.Soc.* **132**, 12792–12793 (2010).

63. Michael A Ochsenkühn and Colin J Campbell. Probing biomolecular interactions using surface enhanced Raman spectroscopy: label-free protein detection using a G-quadruplex DNA aptamer, *Chem.Commun.* **46**, 2799–2801 (2010).

64. D. Graham, B.J. Mallinder and W.E. Smith. Detection and identification of labeled DNA by surface enhanced resonance Raman scattering, *Biopolymers* **57**, 85–91 (2000).

65. S. Habuchi, M. Cotlet, R. Gronheid, G. Dirix, J. Michiels, J. Vanderleyden, F.C. De Schryver and J. Hofkens. Single-molecule surface enhanced resonance Raman spectroscopy of the enhanced green fluorescent protein, *J.Am.Chem.Soc.* **125**, 8446–8447 (2003).

66. Kushagra Singhal and A.Kaan Kalkan. Surface-Enhanced Raman Scattering Captures Conformational Changes of Single Photoactive Yellow Protein Molecules under Photoexcitation, *J.Am.Chem.Soc.* **132**, 429–431 (2009).

67. Inhee Choi, Yun Huh and David Erickson. Ultra-sensitive, label-free probing of the conformational characteristics of amyloid beta aggregates with a SERS active nanofluidic device, *Microfluid.Nanofluid.* **12**, 663–669 (2012).

68. Monica Baia, Simion Astilean and Traian Iliescu. *Raman and SERS investigations of pharmaceuticals*. Springer, (2008).

69. G. Dryhurst and Jack H. Stocker. Electrochemistry of biological molecules, *Journal of The Electrochemical Society* **124**, 390C–390C (1977).

70. Dong Kwon Lim, Ki Seok Jeon, Hyung Min Kim, Jwa Min Nam and Yung Doug Suh. Nanogap-engineerable Raman-active nanodumbbells for single-molecule detection, *Nat.Mater.* **9**, 60–67 (2010).

71. X.M. Qian and S.M. Nie. Single-molecule and single-nanoparticle SERS: from fundamental mechanisms to biomedical applications, *Chem.Soc.Rev.* **37**, 912–920 (2008).

72. Louis Brus. Noble Metal Nanocrystals: Plasmon Electron Transfer Photochemistry and Single-Molecule Raman Spectroscopy, *Acc.Chem.Res.* **41**, 1742–1749 (2008).

73. Ramón A Alvarez-Puebla and Luis M Liz-Marzán. SERS detection of small inorganic molecules and ions, *Angewandte Chemie International Edition* **51**, 11214–11223 (2012).

74. Arjun Kumar Chittoory, Gayatri Kumari, Sudip Mohapatra, Partha P. Kundu, Tapas Kumar Maji, Chandrabhas Narayana and Sridhar Rajaram. Conformational Change in a Urea Catalyst Induced by Sodium Cation and its Effect on Enantioselectivity of a Friedel-Crafts Reaction.

75. George Turrell and Jacques Corset. *Raman microscopy: developments and applications*. Access Online via Elsevier, (1996).

76. Gregory D Smith and Robin JH Clark. Raman microscopy in archaeological science, *Journal of Archaeological Science* **31**, 1137–1160 (2004).

77. Philippe Colomban and Francoise Treppoz. Identification and differentiation of ancient and modern European porcelains by Raman macro-and micro-spectroscopy, *Journal of Raman Spectroscopy* **32**, 93–102 (2001).

78. Christian Matthäus, Amit Kale, Tatyana Chernenko, Vladimir Torchilin and Max Diem. New ways of imaging uptake and intracellular fate of liposomal drug carrier systems inside individual cells, based on Raman microscopy, *Molecular pharmaceutics* **5**, 287–293 (2008).

79. Jian Dong, Craig S Atwood, Vernon E Anderson, Sandra L Siedlak, Mark A Smith, George Perry and Paul R Carey. Metal binding and oxidation of amyloid-β within isolated senile plaque cores: Raman microscopic evidence, *Biochemistry* **42**, 2768–2773 (2003).

80. Notburga Gierlinger and Manfred Schwanninger. The potential of Raman microscopy and Raman imaging in plant research, *Spectroscopy: An International Journal* **21**, 69–89 (2007).

81. Angela Carden and Michael D Morris. Application of vibrational spectroscopy to the study of mineralized tissues (review), *Journal of biomedical optics* **5**, 259–268 (2000).

82. Jaap A Bergwerff, Tom Visser, G Leliveld, Brenda D Rossenaar, de Krijn P Jong and Bert M Weckhuysen. Envisaging the physicochemical processes during the preparation of supported catalysts: Raman microscopy on the impregnation of Mo onto Al2O3 extrudates, *Journal of the American Chemical Society* **126**, 14548–14556 (2004).

83. Michael Bowden and Derek J Gardiner. Stress and structural images of microindented silicon by Raman microscopy, *Applied spectroscopy* **51**, 1405–1409 (1997).

84. Eugenii U Donev, Rene Lopez, Leonard C Feldman and Richard F Haglund Jr.

Confocal Raman Microscopy across the Metal- Insulator Transition of Single Vanadium Dioxide Nanoparticles, *Nano letters* **9**, 702–706 (2009).

85. David N Batchelder, Chunwei Cheng and G David Pitt. Molecular imaging by Raman microscopy, *Advanced Materials* **3**, 566–568 (1991).

86. GV Pavan Kumar and Chandrahhas Narayana. Adapting a fluorescence microscope to perform surface enhanced, *Current science* **93**, 778–781 (2007).

87. G Kavitha, SRC Vivek, A Govindaraj and Chandrabhas Narayana. A low-cost Raman spectrometer design used to study Raman scattering from a single-walled carbon nanotube, *Journal of Chemical Sciences* **115**, 689–694 (2003).

88. P.C. Lee and D. Meisel. Adsorption and surface-enhanced Raman of dyes on silver and gold sols, *J.Phys.Chem.* **86**, 3391–3395 (1982).

89. Frisch, M. J. *et al.* Gaussian 03 Revision C.02. Gaussian Inc. Wallingford CT 2004.

90. Frisch, M. J. *et al.* Gaussian 09 Revision D.01. Gaussian Inc. Wallingford CT 2009.

91. PL Polavarapu. Ab initio vibrational Raman and Raman optical activity spectra, *Journal of Physical Chemistry* **94**, 8106–8112 (1990).

92. V Krishnakumar, Gábor Keresztury, Tom Sundius and R Ramasamy. Simulation of IR and Raman spectra based on scaled DFT force fields: a case study of 2-(methylthio) benzonitrile, with emphasis on band assignment, *Journal of molecular structure* **702**, 9–21 (2004).

93. Stephen D Williams, Timothy J Johnson, Thomas P Gibbons and Christopher L Kitchens. Relative Raman intensities in C6H6, C6D6, and C6F6: a comparison of different computational methods, *Theoretical Chemistry Accounts* **117**, 283–290 (2007).

94. Michal H Jamróz. Vibrational energy distribution analysis VEDA 4, *Warsaw* (2004-2010).

95. E. D. Glendening, A. E. Reed, J. E. Carpenter and F. Weinhold. NBO Version 3.1.

96. David I. Ellis, Victoria L. Brewster, Warwick B. Dunn, J.William Allwood, Alexander P. Golovanov and Royston Goodacre. Fingerprinting food: current technologies for the detection of food adulteration and contamination, *Chem.Soc.Rev.* **41**, 5706–5727 (2012).

97. Ana Gonzalvez, Salvador Garrigues, Sergio Armenta and Miguel de la Guardia. Headspace-Liquid Phase Microextraction for Attenuated Total Reflection Infrared Determination of Volatile Organic Compounds at Trace Levels, *Analytical chemistry* **82**, 3045–3051 (2010).

98. Roger M. Jarvis, Alan Brooker and Royston Goodacre. Surface-Enhanced Raman Spectroscopy for Bacterial Discrimination Utilizing a Scanning Electron Microscope with a Raman Spectroscopy Interface, *Analytical Chemistry* **76**, 5198–5202 (2004). PMID: 15373461.

99. Samuel L. Kleinman, Emilie Ringe, Nicholas Valley, Kristin L. Wustholz, Eric Phillips, Karl A. Scheidt, George C. Schatz and Richard P. Van Duyne. Single-Molecule Surface-Enhanced Raman Spectroscopy of Crystal Violet Isotopologues: Theory and Experiment, *J.Am.Chem.Soc.* **133**, 4115–4122 (2011).

100. Rubn Ahijado-Guzmn, Paulino Gmez-Puertas, Ramn A. Alvarez-Puebla, Germn Rivas and Luis M. Liz-Marzn. Surface-Enhanced Raman Scattering-Based Detection of the Interactions between the Essential Cell Division FtsZ Protein and Bacterial Membrane Elements, *ACS Nano* **6**, 7514–7520 (2012).

101. Taejoon Kang, Seung Min Yoo, Ilsun Yoon, Sang Yup Lee and Bongsoo Kim. Patterned Multiplex Pathogen DNA Detection by Au Particle-on-Wire SERS Sensor, *Nano Lett.* **10**, 1189–1193 (2010).

102. Evanthia Papadopoulou and Steven E.J. Bell. Label-Free Detection of Single-Base Mismatches in DNA by Surface-Enhanced Raman Spectroscopy, *Angew.Chem., Int.Ed.* **50**, 9058–9061 (2011).

103. K. Kneipp, H. Kneipp and J. Kneipp. Surface-enhanced raman scattering in local optical fields of silver and gold nanoaggregates - From single-molecule raman spectroscopy to ultrasensitive probing in live cells, *Acc.Chem.Res.* **39**, 443–450 (2006).

104. B.D. Moore, L. Stevenson, A. Watt, S. Flitsch, N.J. Turner, C. Cassidy and D. Graham. Rapid and ultra-sensitive determination of enzyme activities using surface-enhanced resonance Raman scattering, *Nat.Biotechnol.* **22**, 1133–1138 (2004).

105. Andrew J. Bonham, Gary Braun, Ioana Pavel, Martin Moskovits and Norbert O. Reich. Detection of Sequence-Specific Protein-DNA Interactions via Surface Enhanced Resonance Raman Scattering, *J.Am.Chem.Soc.* **129**, 14572–14573 (2007).

106. D. Graham, B.J. Mallinder and W.E. Smith. Surface-enhanced resonance Raman scattering as a novel method of DNA discrimination, *Angew.Chem., Int.Edit.* **39**, 1061–1063 (2000).

107. G.V. Pavan Kumar, B.A. Ashok Reddy, M. Arif, T.K. Kundu and C. Narayana. Surface-enhanced raman scattering studies of human transcriptional coactivator p300, *J.Phys.Chem.B* **110**, 16787–16792 (2006).

108. K. Mantelingu, A.H. Kishore, K. Balasubramanyam, G.V.P. Kumar, M. Altaf, S.N. Swamy, R. Selvi, C.I. Das, C. Narayana, K.S. Rangappa and T.K. Kundu. Activation of p300 histone acetyltransferase by small molecules altering enzyme structure: Probed by surface-enhanced raman spectroscopy, *J.Phys.Chem.B* **111**, 4527–4534 (2007).

109. K. Mantelingu, B.A.A. Reddy, V. Swaminathan, A.H. Kishore, N.B. Siddappa, G.V.P. Kumar, G. Nagashankar, N. Natesh, S. Roy, P.P. Sadhale, U. Ranga, C.

Narayana and T.K. Kundu. Specific Inhibition of p300-HAT Alters Global Gene Expression and Represses HIV Replication, *Chem.Biol.* **14**, 645–657 (2007).

110. Xiao X. Han, Genin Gary Huang, Bing Zhao and Yukihiro Ozaki. Label-Free Highly Sensitive Detection of Proteins in Aqueous Solutions Using Surface-Enhanced Raman Scattering, *Anal.Chem.* **81**, 3329–3333 (2009).

111. Bing HanXiao X.; Zhao and Yukihiro Ozaki. Surface-enhanced Raman scattering for protein detection, *Anal.Bioanal.Chem.* **394**, 1719–1727 (2009).

112. G.V.P. Kumar, Ruthrotha Selvi, A.Hari Kishore, Tapas K. Kundu and Chandrabhas Narayana. Surface-Enhanced Raman Spectroscopic Studies of Coactivator-Associated Arginine Methyltransferase 1, *J.Phys.Chem B* **112**, 6703–6707 (2008).

113. Amitabha De, V Ramesh, S Mahadevan and V Nagaraja. Mg2+ mediated sequence-specific binding of transcriptional activator protein C of bacteriophage Mu to DNA, *Biochemistry* **37**, 3831–3838 (1998).

114. Ganduri Swapna, Matheswaran Saravanan and Valakunja Nagaraja. Conformational Changes Triggered by Mg2+ Mediate Transactivator Function, *Biochemistry* **48**, 2347–2354 (2009).

115. Pavel Anzenbacher, Peter Mojzes, Vladimir Baumruk and Even Amler. Changes in Na+,K+-ATPase structure induced by cation binding Approach by Raman spectroscopy, {*FEBS*} *Letters* **312**, 80 – 82 (1992).

116. IR Nabiev, KN Dzhandzhugazyan, RG Efremov and NN Modyanov. Binding of monovalent cations induces large changes in the secondary structure of Na +, K + -ATPase as probed by Raman spectroscopy, *FEBS letters* **236**, 235–239 (1988).

117. Claus Hélix Nielsen, Salim Abdali, Jens August Lundbæk and Flemming Cornelius. Raman Spectroscopy of Conformational Changes in Membrane-Bound Sodium Potassium ATPase, *Spectroscopy* **22**, 52–63 (2007).

118. Sanford A. Asher. UV resonance Raman spectroscopy for analytical, physical, and biophysical chemistry. Part 1, *Anal.Chem.* **65**, 59A–66A (1993).

119. Renee D. JiJi, Gurusamy Balakrishnan, Ying Hu and Thomas G. Spiro. Intermediacy of poly (L-proline) II and β-strand conformations in poly (L-lysine) β-sheet formation probed by temperature-jump/UV resonance Raman spectroscopy, *Biochemistry* **45**, 34–41 (2005).

120. Sanford A. Asher, Anatoli Ianoul, Guido Mix, Mary N. Boyden, Anton Karnoup, Max Diem and Reinhard Schweitzer-Stenner. Dihedral Angle Dependence of the Amide III Vibration: A Uniquely Sensitive UV Resonance Raman Secondary Structural Probe, *J.Am.Chem.Soc.* **123**, 11775–11781 (2001).

121. Zhenhuan Chi and Sanford A. Asher. UV Resonance Raman Determination of Protein Acid Denaturation:Selective Unfolding of Helical Segments of Horse Myoglobin, *Biochemistry* **37**, 2865–2872 (1998).

122. Zeeshan Ahmed, Ilir A. Beta, Aleksandr V. Mikhonin and Sanford A. Asher. UV-Resonance Raman Thermal Unfolding Study of Trp-Cage Shows That It Is Not a Simple Two-State Miniprotein, *J.Am.Chem.Soc.* **127**, 10943–10950 (2005).

123. V. Jayaraman, K.R. Rodgers, I. Mukerji and T.G. Spiro. Hemoglobin allostery: resonance Raman spectroscopy of kinetic intermediates, *Science* **269**, 1843–1848 (1995).

124. Manliang Feng and Hiroyasu Tachikawa. Surface-Enhanced Resonance Raman Spectroscopic Characterization of the Protein Native Structure, *J.Am.Chem.Soc.* **130**, 7443–7448 (2008).

125. V. Ramesh, A. De and V. Nagaraja. Engineering Hyperexpression of Bacteriophage-Mu C-Protein by Removal of Secondary Structure at the Translation Initiation Region, *Protein Eng.* **7**, 1053–1057 (1994).

126. RC Edgar. MUSCLE:multiple sequence alignment with high accuracy and high throughput, *Nucleic Acids Res.* **32**, 1792–1797 (2004).

127. Evgeny Krissinel and Kim Henrick. Inference of macromolecular assemblies from crystalline state, *Journal of molecular biology* **372**, 774–797 (2007).

128. W.L. DeLano. The PyMOL Molecular Graphics System (2002) DeLano Scientific, San Carlos, CA, USA. http://www.pymol.org, (2011).

129. V. Ramesh and V. Nagaraja. Sequence-specific DNA Binding of the Phage Mu C Protein : Footprinting Analysis Reveals Altered DNA Conformation Upon Protein Binding, *Journal of Molecular Biology* **260**, 22–33 (1996).

130. Shashwati Basak and Valakunja Nagaraja. DNA Unwinding Mechanism for the Transcriptional Activation ofmomP1 Promoter by the Transactivator Protein C of Bacteriophage Mu, *J.Bio.Chem.* **276**, 46941–46945 (2001).

131. K. Kneipp, H. Kneipp, I. Itzkan, R.R. Dasari and M.S. Feld. Surface-enhanced Raman scattering and biophysics, *Journal of Physics Condensed Matter* **14**, R597 (2002).

132. Atanu Sengupta, Corrine K. Thai, M.S.R. Sastry, James F. Matthaei, Daniel T. Schwartz, E.James Davis and François Baneyx. A Genetic Approach for Controlling the Binding and Orientation of Proteins on Nanoparticles, *Langmuir* **24**, 2000–2008 (2008).

133. C.D. Keating, K.M. Kovaleski and M.J. Natan. Protein : colloid conjugates for surface enhanced Raman scattering: Stability and control of protein orientation, *J.Phys.Chem.B* **102**, 9404–9413 (1998).

134. Bindu Diana Paul, Aditi Kanhere, Atanu Chakraborty, Manju Bansal and Valakunja Nagaraja. Identification of the domains for DNA binding and transactivation function of C protein from bacteriophage Mu, *Proteins* **52**, 272–282 (2003).

135. V.M. Hallmark and A. Campion. Selection rules for surface Raman spectroscopy: Experimental results, *J.Chem.Phys.* **84**, 2933–2941 (1986).

136. M. Moskovits. Surface selection rules, *J.Chem.Phys.* **77**, 4408–4416 (1982).

137. Q.M. Yu and G. Golden. Probing the protein orientation on charged self-assembled monolayers on gold nanohole arrays by SERS, *Langmuir* **23**, 8659–8662 (2007).

138. E. Podstawka, Y. Ozaki and L.M. Proniewicz. Adsorption of S-S containing proteins on a colloidal silver surface studied by surface-enhanced Raman spectroscopy, *Apl.Spectrosc.* **58**, 1147–1156 (2004).

139. E.S. Grabbe and R.P. Buck. Surface-enhanced raman spectroscopic investigation of human immunoglobulin G adsorbed on a silver electrode, *J.Am.Chem.Soc.* **111**, 8362–8366 (1989).

140. M.C. Chen and R.C. Lord. Laser-excited Raman spectroscopy of biomolecules. VIII. Conformational study of bovine serum albumin, *J.Am.Chem.Soc.* **98**, 990–992 (1976).

141. G.D. Chumanov, R.G. Efremov and I.R. Nabiev. Surface-enhanced Raman spectroscopy of biomolecules. Part I.-water-soluble proteins, dipeptides and amino acids, *J.Raman Spectrosc.* **21**, 43–48 (1990).

142. E. Podstawka, Y. Ozaki and L.M. Proniewicz. Part I: Surface-enhanced Raman spectroscopy investigation of amino acids and their homodipeptides adsorbed on colloidal silver, *Apl.Spectrosc.* **58**, 570–580 (2004).

143. Ioana Pavel, Evan McCarney, Adam Elkhaled, Andrew Morrill, Kevin Plaxco and Martin Moskovits. Label-Free SERS Detection of Small Proteins Modified to Act as Bifunctional Linkers, *J.Phys.Chem.C.* **112**, 4880–4883 (2008).

144. Stacy A. Overman and George J. Thomas. Amide Modes of the -Helix: Raman Spectroscopy of Filamentous Virus fd Containing Peptide 13C 13Cand 2H Labels in Coat Protein Subunits, *Biochemistry* **37**, 5654–5665 (1998).

145. Roman Tuma, Peter E. Prevelige and George J. Thomas. Mechanism of capsid maturation in a double-stranded DNA virus, *Proceedings of the National Academy of Sciences* **95**, 9885–9890 (1998).

146. A Barth and C Zscherp. What vibrations tell us about proteins., *Q Rev Biophys* **35**, 369–430– (2002).

147. A T Tu. *Spectroscopy of biological systems. Advances in spectroscopy*. Wiley, (1986).

148. Davide Ferrari, James R. Diers, David F. Bocian, Niels C. Kaarsholm and Michael F. Dunn. Raman signatures of ligand binding and allosteric conformation change in hexameric insulin, *Biopolymers* **62**, 249–260 (2001).

149. T.M. Cotton, S.G. Schultz and R.P. Van Duyne. Surface-enhanced resonance Raman scattering from cytochrome c and myoglobin adsorbed on a silver electrode, *J.Am.Chem.Soc.* **102**, 7960–7962 (1980).

150. J.L. Lippert, R.M. Lindsay and R. Schultz. Laser Raman characterization of conformational changes in sarcoplasmic reticulum induced by temperature, Ca2+, and Mg2+, *J.Bio.Chem.* **256**, 12411–12416 (1981).

151. Mwindaace N. Siamwiza, Richard C. Lord, Michael C. Chen, Tadahisa Takamatsu, Issei Harada, Hiroatsu Matsuura and Takehiko Shimanouchi. Interpretation of the doublet at 850 and 830 cm-1 in the Raman spectra of tyrosyl residues in proteins and certain model compounds, *Biochemistry* **14**, 4870–4876 (1975).

152. Eunice CY Li-Chan and Ling Qin. *The application of Raman spectroscopy to the structural analysis of food protein networks*. AOCS Press: Champaign, IL, (1998).

153. RC Lord and Nai-Teng Yu. Laser-excited Raman spectroscopy of biomolecules: I. Native lysozyme and its constituent amino acids, *Journal of molecular biology* **50**, 509–524 (1970).

154. Martin Hedegaard, Christoph Krafft, Henrik J Ditzel, Lene E Johansen, Søren Hassing and Jurgen Popp. Discriminating Isogenic Cancer Cells and Identifying Altered Unsaturated Fatty Acid Content as Associated with Metastasis Status, Using K-Means Clustering and Partial Least Squares-Discriminant Analysis of Raman Maps, *Anal.Chem.* **82**, 2797–2802 (2010).

155. Jon A. Dieringer, Adam D. McFarland, Nilam C. Shah, Douglas A. Stuart, Alyson V. Whitney, Chanda R. Yonzon, Matthew A. Young, Xiaoyu Zhang and Richard P. Van Duyne. Introductory Lecture Surface enhanced Raman spectroscopy: new materials, concepts, characterization tools, and applications, *Faraday Discuss.* **132**, 9–26 (2006).

156. He Huang, Jing Xie, Xiaoli Liu, Lin Yuan, Shasha Wang, Songxi Guo, Haoran Yu, Hong Chen, Yanliang Zhang and Xiaohu Wu. Conformational Changes of Protein Adsorbed on Tailored Flat Substrates with Different Chemistries, *ChemPhysChem* **12**, 3642–3646 (2011).

157. G.B. Deacon and R.J. Phillips. Relationships between the carbon-oxygen stretching frequencies of carboxylato complexes and the type of carboxylate coordination, *Coord.Chem.Rev.* **33**, 227–250 (1980).

158. E Li-Chan, S. Nakai and M Hirotsuka. Raman spectroscopy as a probe of protein structure in food system. in *Protein Structure- Function Relationships in Foods,* (Rickey Y Yada and R.L. Jackman, eds), 163–197. Chapman and Hall Inc, New York (1994).

159. Ana M. Herrero. Raman Spectroscopy for Monitoring Protein Structure in Muscle Food Systems, *Crit.Rev.Food Sci.Nutr.* **48**, 512–523 (2008).

160. Dian He, Bo Hu, Qiao-Feng Yao, Kan Wang and Shu-Hong Yu. Large-scale synthesis of flexible free-standing SERS substrates with high sensitivity: electrospun PVA nanofibers embedded with controlled alignment of silver nanoparticles, *ACS nano* **3**, 3993–4002 (2009).

161. Yi Chen, Eduardo R. Cruz-Chu, Jaie C. Woodard, Manas R. Gartia, Klaus Schulten and Logan Liu. Electrically Induced Conformational Change of Peptides on Metallic Nanosurfaces, *ACS Nano* **6**, 8847–8856 (2012).

162. K. Balasubramanyam, V. Swaminathan, A. Ranganathan and T.K. Kundu. Small molecule modulators of histone acetyltransferase p300, *J.Bio.Chem.* **278**, 19134–19140 (2003).

163. H.M. Chan and N.B. La Thangue. p300/CBP proteins: HATs for transcriptional bridges and scaffolds, *Journal of Cell Science* **114**, 2363–2373 (2001).

164. C. Das and T.K. Kundu. Transcriptional regulation by the acetylation of nonhistone proteins in humans - A new target for therapeutics, *IUBMB Life* **57**, 137–148 (2005).

165. R.H. Giles, D.J.M. Peters and M.H. Breuning. Conjunction dysfunction: CBP/p300 in human disease, *Trends in Genetics* **14**, 178–183 (1998).

166. V. Swaminathan, A.H. Kishore, K.K. Febitha and T.K. Kundu. Human histone chaperone nucleophosmin enhances acetylation-dependent chromatin transcription, *Molecular and Cellular Biology* **25**, 7534–7545 (2005).

167. R.A. Varier, V. Swaminathan, K. Balasubramanyam and T.K. Kundu. Implications of small molecule activators and inhibitors of histone acetyltransferases in chromatin therapy, *Biochemical Pharmacology* **68**, 1215–1220 (2004).

168. A.J. Bannister and T. Kouzarides. The CBP co-activator is a histone acetyltransferase, *Nature* **384**, 641–643 (1996).

169. B. Ruthrotha Selvi, Dinesh Jagadeesan, B. S. Suma, G. Nagashankar, M. Arif, K. Balasubramanyam, M. Eswaramoorthy and Tapas K. Kundu. Intrinsically Fluorescent Carbon Nanospheres as a Nuclear Targeting Vector: Delivery of Membrane-Impermeable Molecule to Modulate Gene Expression In Vivo, *Nano Letters* **8**, 3182–3188 (2008). PMID: 18800851.

170. James B.Foresman and AEleen Frisch. *Exploring Chemistry With Electronic Structure Methods: A Guide to Using Gaussian*. Gaussian, (1996).

171. G. Keresztury, S. Holly, G. Besenyei, J. Varga, A.Y. Wang and J.R. Durig. Vibrational-Spectra of Monothiocarbamates .2. Ir and Raman-Spectra, Vibrational Assignment, Conformational-Analysis and Ab-Initio Calculations of S-Methyl-N, N-Dimethylthiocarbamate, *Spectrochimica Acta Part A-Molecular and Biomolecular Spectroscopy* **49**, 2007–2026 (1993).

172. H. Arslan, U. Florke, N. Kulcu and G. Binzet. The molecular structure and vibrational spectra of 2-chloro-N-(diethylcarbamothioyl)benzamide by Hartree-Fock and density functional methods, *Spectrochimica Acta Part A-Molecular and Biomolecular Spectroscopy* **68**, 1347–1355 (2007).

173. V. Krishnakumar, S. Dheivamalar, R.J. Xavier and V. Balachandran. Analysis of vibrational spectra of 4-amino-2,6-dichloropyridine and 2-chloro-3,5-dinitropyridine based on density functional theory calculations, *Spectrochimica Acta Part A-Molecular and Biomolecular Spectroscopy* **65**, 147–154 (2006).

174. C.Y. Panicker, H.T. Varghese, V.S. Madhavan, S. Mathew, J. Vinsova, C. Van Alsenoy, Y.S. Mary and Y.S. Mary. FT-IR, FT-Raman, and computational calculations of 4-chloro-2-(3-chlorophenyl carbamoyl)phenyl acetate, *J.Raman Spectrosc.* **40**, 2176–2186 (2009).

175. P. Sett, N. Paul, S. Chattopadhyay and P.K. Mallick. Molecular structures in the excited states of 2-and 4-benzylpyridine, *J.Raman Spectrosc.* **30**, 277–287 (1999).

176. P. Sett, S. Chattopadhyay and P.K. Mallick. Raman excitation profiles and excited state molecular configurations of three isomeric phenyl pyridines, *Spectrochimica Acta Part A-Molecular and Biomolecular Spectroscopy* **56**, 855–875 (2000).

177. P. Sett, S. Chattopadhyay and P.K. Mallick. Normal coordinate analyses of three isomeric acetylpyridines and acetophenone, *J.Raman Spectrosc.* **31**, 177–184 (2000).

178. Dana W Mayo, Foil A Miller and Robert W Hannah. *Course notes on the interpretation of infrared and Raman spectra*. John Wiley & Sons, (2004).

179. E.F. Mooney. The infrared spectra of chloro- and bromobenzene derivatives–I : Anisoles and phenetoles, *Spectrochimica Acta* **19**, 877–887 (1963).

180. E.F. Mooney. The infra-red spectra of chloro- and bromobenzene derivatives–II. Nitrobenzenes, *Spectrochimica Acta* **20**, 1021–1032 (1964).

181. M. Kurt. DFT simulations and vibrational spectra of 4-chloro and 4-bromophenylboronic acid molecules, *J.Raman Spectrosc.* **40**, 67–75 (2009).

182. A.G. Iriarte, E.H. Cutin, M.F. Erben, S.E. Ulic, J.L. Jios and C.O. Della Vedova. Vibrational studies of N-trifluoroacetyl-phosphoramidic acid dichloride [CF3C(O)NHP(O)Cl-2] and N-trichloroacetyl-phosphoramidic acid dichloride [CCl3C(O)NHP(O)Cl-2], *Vibrational Spectroscopy* **46**, 107–114 (2008).

183. A.G. Iriarte, N.L. Robles, E.H. Cutin and C.O. Della Vedova. Vibrational spectra and theoretical calculations of [(trifluoromethyl)sulfonyl] phosphorimidic trichloride (CF3SO2N-PCl3), *J.Mol.Struct.* **888**, 7–12 (2008).

184. A. Kovacs. Vibrational analysis of 3-trifluoromethylphenol, *J.Mol.Struct.* **650**, 99–104 (2003).

185. C.Y. Panicker, H.T. Varghese, D. Philip, H.I. Nogueira and K. Castkova. Raman, IR and SERS spectra of methyl(2-methyl-4,6-dinitrophenylsulfanyl)ethanoate, *Spectrochim.Acta A Mol.Biomol.Spectrosc.* **67**, 1313–1320 (2007).

186. J. Sarkar, J. Chowdhury, M. Ghosh, Rina De and G.B. Talapatra. Adsorption of 2-aminobenzothiazole on colloidal silver particles: An experimental and theoretical surface-enhanced Raman scattering study, *J.Phys.Chem.B* **109**, 12861–12867 (2005).

187. C. Zuo and P.W. Jagodzinski. Surface-enhanced raman scattering of pyridine using different metals: Differences and explanation based on the selective formation of +-pyridyl on metal surfaces, *J.Phys.Chem.B* **109**, 1788–1793 (2005).

188. A. Campion and P. Kambhampati. Surface-enhanced Raman scattering, *Chem.Soc.Rev.* **27**, 241–250 (1998).

189. Dylan W Domaille, Emily L Que and Christopher J Chang. Synthetic fluorescent sensors for studying the cell biology of metals, *Nature Chemical Biology* **4**, 168–175 (2008).

190. Byung-Eun Kim, Tracy Nevitt and Dennis J Thiele. Mechanisms for copper acquisition, distribution and regulation, *Nature chemical biology* **4**, 176–185 (2008).

191. Darryl Y Sasaki, Deborah R Shnek, Daniel W Pack and Frances H Arnold. Metall-induzierte Dispersion von Lipid-Aggregaten; ein einfacher, selektiver und empfindlicher Fluoreszenzsensor für Metall-Ionen, *Angewandte Chemie* **107**, 994–996 (1995).

192. Deborah R Shnek, Daniel W Pack, Frances H Arnold and Darryl Y Sasaki. Metal-Induced Dispersion of Lipid Aggregates: A Simple, Selective, and Sensitive Fluorescent Metal Ion Sensor, *Angewandte Chemie International Edition in English* **34**, 905–907 (1995).

193. Alicia Torrado, Grant K Walkup and Barbara Imperiali. Exploiting polypeptide motifs for the design of selective Cu (II) ion chemosensors, *Journal of the American Chemical Society* **120**, 609–610 (1998).

194. Patrizia Grandini, Fabrizio Mancin, Paolo Tecilla, Paolo Scrimin and Umberto Tonellato. Anwendung einer Selbstorganisationsstrategie beim Design selektiver Chemosensoren für CuII-Ionen, *Angewandte Chemie* **111**, 3247–3250 (1999).

195. Patrizia Grandini, Fabrizio Mancin, Paolo Tecilla, Paolo Scrimin and Umberto Tonellato. Exploiting the Self-Assembly Strategy for the Design of Selective CuII Ion Chemosensors, *Angewandte Chemie International Edition* **38**, 3061–3064 (1999).

196. Joan Selverstone Valentine and P John Hart. Misfolded CuZnSOD and amyotrophic lateral sclerosis, *Proceedings of the National Academy of Sciences* **100**, 3617–3622 (2003).

197. Glenn L Millhauser. Copper binding in the prion protein, *Accounts of chemical research* **37**, 79–85 (2004).

198. Kevin J Barnham, Colin L Masters and Ashley I Bush. Neurodegenerative diseases and oxidative stress, *Nature Reviews Drug Discovery* **3**, 205–214 (2004).

199. Elena Gaggelli, Henryk Kozlowski, Daniela Valensin and Gianni Valensin. Copper homeostasis and neurodegenerative disorders (Alzheimer's, prion, and Parkinson's diseases and amyotrophic lateral sclerosis), *Chemical reviews* **106**, 1995–2044 (2006).

200. Scot C Leary, Paul A Cobine, Brett A Kaufman, Guy-Hellen Guercin, Andre Mattman, Jan Palaty, Gillian Lockitch, Dennis R Winge, Pierre Rustin, Rita Horvath et al. The Human Cytochrome c Oxidase Assembly Factors SCO1 and SCO2 Have Regulatory Roles in the Maintenance of Cellular Copper Homeostasis, *Cell metabolism* **5**, 9–20 (2007).

201. Stephen G Kaler. ATP7A-related copper transport diseasesemerging concepts and future trends, *Nature reviews Neurology* **7**, 15–29 (2011).

202. Kasper P Kepp. Bioinorganic chemistry of Alzheimers disease, *Chemical Reviews* **112**, 5193–5239 (2012).

203. Silvano Cavalli, Stefano Polesello and Sara Valsecchi. Chloride interference in the determination of bromate in drinking water by reagent free ion chromatography with mass spectrometry detection, *Journal of Chromatography A* **1085**, 42 – 46 (2005).

204. Edith Chow, D Brynn Hibbert and J Justin Gooding. Voltammetric detection of cadmium ions at glutathione-modified gold electrodes, *Analyst* **130**, 831–837 (2005).

205. Kenneth W Jackson and Tariq M Mahmood. Atomic absorption, atomic emission, and flame emission spectrometry, *Analytical chemistry* **66**, 252R–279R (1994).

206. Jinglian Li, Lingxin Chen, Tingting Lou and Yunqing Wang. Highly Sensitive SERS Detection of As3+ Ions in Aqueous Media using Glutathione Functionalized Silver Nanoparticles, *ACS Applied Materials & Interfaces* **3**, 3936–3941 (2011).

207. Jun Yin, Tao Wu, Jibin Song, Qian Zhang, Shiyong Liu, Rong Xu and Hongwei Duan. SERS-Active Nanoparticles for Sensitive and Selective Detection of Cadmium Ion (Cd2+), *Chemistry of Materials* **23**, 4756–4764 (2011).

208. Junling Duan, Min Yang, Yongchao Lai, Jingpeng Yuan and Jinhua Zhan. A colorimetric and surface-enhanced Raman scattering dual-signal sensor for Hg2+ based on Bismuthiol II-capped gold nanoparticles, *Analytica Chimica Acta* **723**, 88 – 93 (2012).

209. Ramn Alvarez-Puebla, Luis M. Liz-Marzn and Garca de F. Javier Abajo. Light Concentration at the Nanometer Scale, *The Journal of Physical Chemistry Letters* **1**, 2428–2434 (2010).

210. Yan Zhao, James N Newton, Jie Liu and Alexander Wei. Dithiocarbamate-Coated SERS Substrates: Sensitivity Gain by Partial Surface Passivation, *Langmuir* **25**, 13833–13839 (2009).

211. Vitor M Zamarion, Ronaldo A Timm, Koiti Araki and Henrique E Toma. Ultrasensitive SERS nanoprobes for hazardous metal ions based on trimercaptotriazine-modified gold nanoparticles, *Inorganic chemistry* **47**, 2934–2936 (2008).

212. Dionysia Tsoutsi, Jose Maria Montenegro, Fabian Dommershausen, Ulrich Koert, Luis M Liz-Marzan, Wolfgang J Parak and Ramon A Alvarez-Puebla. Quantitative surface-enhanced Raman scattering ultradetection of atomic inorganic ions: the case of chloride, *ACS nano* **5**, 7539–7546 (2011).

213. Seung Joon Lee and Martin Moskovits. Visualizing chromatographic separation of metal ions on a surface-enhanced Raman active medium, *Nano letters* **11**, 145–150 (2010).

214. Sougata Sarkar, Mukul Pradhan, Arun Kumar Sinha, Mrinmoyee Basu and Tarasankar Pal. Selective and Sensitive Recognition of Cu2+ in an Aqueous Medium: A Surface-Enhanced Raman Scattering (SERS)-Based Analysis with a Low-Cost Raman Reporter, *Chemistry-A European Journal* **18**, 6335–6342 (2012).

215. Debabrata Maity, Arun K Manna, D Karthigeyan, Tapas K Kundu, Swapan K Pati and T Govindaraju. Visible–Near-Infrared and Fluorescent Copper Sensors Based on Julolidine Conjugates: Selective Detection and Fluorescence Imaging in Living Cells, *Chemistry-A European Journal* **17**, 11152–11161 (2011).

216. Koji Hasegawa, Taka-aki Ono and Takumi Noguchi. Ab initio density functional theory calculations and vibrational analysis of zinc-bound 4-methylimidazole as a model of a histidine ligand in metalloenzymes, *The Journal of Physical Chemistry A* **106**, 3377–3390 (2002).

217. NIST Computational Chemistry Comparison and Benchmark Database (CCCBDB), NIST Standard Reference Database Number 101, Release 16a, August 2013, Editor: Johnson III, Russell D; http://cccbdb.nist.gov/.

218. Partha P Kundu, Tuhin Bhowmick, Swapna Ganduri, GV Pavan Kumar, Valakunja Nagaraja and Chandrabhas Narayana. Capturing Allosteric Transition Induced by Mg2+ ion in a Transactivator by SERS.

219. Francis R Dollish, William G Fateley and Freeman F Bentley. *Characteristic Raman frequencies of organic compounds*, volume 27. Wiley New York, (1974).

220. H. Ciurla, J. Michalski, J. Hanuza, M. Mczka, T. Talik and Z. Talik. Molecular structure, IR and Raman spectra as well as DFT chemical calculations for alkylaminoacetylureas: vibrational characteristics of dicarbonylimide bridge, *Spectrochimica Acta Part A: Molecular and Biomolecular Spectroscopy* **64**, 34 – 46 (2006).

221. SR Sheeja, Neema Ani Mangalam, MR Prathapachandra Kurup, Y Sheena Mary, K Raju, Hema Tresa Varghese and C Yohannan Panicker. Vibrational spectroscopic studies and computational study of quinoline-2-carbaldehyde benzoyl hydrazone, *Journal of Molecular Structure* **973**, 36–46 (2010).

222. Alexandr Gorski, Sylwester Gawinkowski, Roman Luboradzki, Marek Tkacz, Randolph P Thummel and Jacek Waluk. Polymorphism, Hydrogen Bond Properties, and Vibrational Structure of 1H-Pyrrolo [3, 2-h] Quinoline Dimers, *Journal of Atomic, Molecular, and Optical Physics* **2012** (2012).

223. Alexandr Gorski, Sylwester Gawinkowski, Jerzy Herbich, Oliver Krauss, Bernhard Brutschy, Randolph P Thummel and Jacek Waluk. 1 H-Pyrrolo [3, 2-h] quinoline: A Benchmark Molecule for Reliable Calculations of Vibrational Frequencies, IR Intensities, and Raman Activities, *The Journal of Physical Chemistry A* **116**, 11973–11986 (2012).

224. Partha P. Kundu, Gayatri Kumari, Arjun Kumar Chittoory, Sridhar Rajaram and Chandrabhas Narayana.

225. V CHIŞ, M Oltean, A PÎRNĂU, V MICLĂUŞ and S Filip. Spectral and theoretical studies of 2-naphthalenol: an organic nonlinear optical crystalline material, *JOURNAL OF OPTOELECTRONICS AND ADVANCED MATERIALS* **8**, 1143–1147 (2006).

226. Aysen E Ozel, Sefa Celik and Sevim Akyuz. Vibrational spectroscopic investigation of free and coordinated 5-aminoquinoline: The IR, Raman and DFT studies, *Journal of Molecular Structure* **924**, 523–530 (2009).

227. Elżbieta Górnicka, Joanna E Rode, Ewa D Raczyńska, Beata Dasiewicz and Jan Cz Dobrowolski. Experimental (FT-IR and Raman) and theoretical (DFT) studies on the vibrational dynamics in cytisine, *Vibrational spectroscopy* **36**, 105–115 (2004).

228. N Subramanian, N Sundaraganesan, S Sudha, V Aroulmoji, GD Sockalingam and M Bergamin. Experimental and theoretical investigation of the molecular and electronic structure of anticancer drug camptothecin, *Spectrochimica Acta Part A: Molecular and Biomolecular Spectroscopy* **78**, 1058–1067 (2011).

229. M Kumru, V Küçük and M Kocademir. Determination of structural and vibrational properties of 6-quinolinecarboxaldehyde using FT-IR, FT-Raman and Dispersive-Raman experimental techniques and theoretical HF and DFT (B3LYP) methods, *Spectrochimica Acta Part A: Molecular and Biomolecular Spectroscopy* **96**, 242–251 (2012).

230. IB Cozar, L Szabó, D Mare, N Leopold, L David and V Chiş. IR, Raman, SERS and DFT study of paroxetine, *Journal of Molecular Structure* **993**, 243–248 (2011).

231. Rajeshwar D Bindal, Joseph T Golab and John A Katzenellenbogen. Ab initio calculations on N-methylmethanesulfonamide and methyl methanesulfonate for

the development of force field torsional parameters and their use in the conformational analysis of some novel estrogens, *Journal of the American Chemical Society* **112**, 7861–7868 (1990).

232. NI Dodoff. Conformational and vibrational analysis N-3-pyridinylmethane sulphonamide, *The Internet J. Vibr. Spectrosc* **4** (1999).

233. Neslihan Özbek, Hikmet Katırcıoğlu, Nurcan Karacan and Tülay Baykal. Synthesis, characterization and antimicrobial activity of new aliphatic sulfonamide, *Bioorganic & medicinal chemistry* **15**, 5105–5109 (2007).

234. Partha P Kundu, GV Pavan Kumar, Kempegowda Mantelingu, Tapas K Kundu and Chandrabhas Narayana. Raman and surface enhanced Raman spectroscopic studies of specific, small molecule activator of histone acetyltransferase p300, *Journal of Molecular Structure* **999**, 10–15 (2011).

235. Asha Chandran, Y. Sheena Mary, Hema Tresa Varghese, C. Yohannan Panicker, Pavel Pazdera, G. Rajendran and N. Babu. FT-IR, FT-Raman spectroscopy and computational study of N-carbamimidoyl-4-[(E)-((2-hydroxyphenyl)methylidene]aminobenzenesulfonamide, *Journal of Molecular Structure* **992**, 77 – 83 (2011).

236. Melissa F Mrozek, Sally A Wasileski and Michael J Weaver. Periodic trends in electrode-chemisorbate bonding: Benzonitrile on platinum-group and other noble metals as probed by surface-enhanced Raman spectroscopy combined with density functional theory, *Journal of the American Chemical Society* **123**, 12817–12825 (2001).

237. K Helios, R Wysokinski, W Zierkiewicz, LM Proniewicz and D Michalska. Unusual noncovalent interaction between the chelated Cu (II) ion and the π bond in the vitamin B13 complex, cis-diammine (orotato) copper (II): theoretical and vibrational spectroscopy studies, *The Journal of Physical Chemistry B* **113**, 8158–8169 (2009).

238. Roger M Jarvis, Nicholas Law, Iqbal T Shadi, Paul OBrien, Jonathan R Lloyd and Royston Goodacre. Surface-enhanced Raman scattering from intracellular and extracellular bacterial locations, *Analytical chemistry* **80**, 6741–6746 (2008).

239. Sandeep P. Ravindranath, Kristene L. Henne, Dorothea K. Thompson and Joseph Irudayaraj. Raman Chemical Imaging of Chromate Reduction Sites in a Single Bacterium Using Intracellularly Grown Gold Nanoislands, *ACS Nano* **5**, 4729–4736 (2011).

240. Jun Ando, Katsumasa Fujita, Nicholas I. Smith and Satoshi Kawata. Dynamic SERS Imaging of Cellular Transport Pathways with Endocytosed Gold Nanoparticles, *Nano Lett.* **11**, 5344–5348 (2011).

241. Abigail G Doyle and Eric N Jacobsen. Small-molecule H-bond donors in asymmetric catalysis, *Chemical reviews* **107**, 5713–5743 (2007).

242. Mark S Taylor and Eric N Jacobsen. Asymmetric catalysis by chiral hydrogen-bond donors, *Angewandte Chemie International Edition* **45**, 1520–1543 (2006).

243. Stephen J Connon. Organocatalysis mediated by (thio) urea derivatives, *Chemistry-A European Journal* **12**, 5418–5427 (2006).

244. Petri M Pihko. Activation of carbonyl compounds by double hydrogen bonding: An emerging tool in asymmetric catalysis, *Angewandte Chemie International Edition* **43**, 2062–2064 (2004).

245. Scott J Miller. In search of peptide-based catalysts for asymmetric organic synthesis, *Accounts of chemical research* **37**, 601–610 (2004).

246. Peter R Schreiner. Metal-free organocatalysis through explicit hydrogen bonding interactions, *Chemical Society Reviews* **32**, 289–296 (2003).

247. Elizabeth R Jarvo and Scott J Miller. Amino acids and peptides as asymmetric organocatalysts, *Tetrahedron* **58**, 2481–2495 (2002).

248. Gergely Jakab, Carlo Tancon, Zhiguo Zhang, Katharina M Lippert and Peter R Schreiner. (Thio) urea Organocatalyst Equilibrium Acidities in DMSO, *Organic Letters* **14**, 1724–1727 (2012).

249. Katrina H Jensen and Matthew S Sigman. Evaluation of Catalyst Acidity and Substrate Electronic Effects in a Hydrogen Bond-Catalyzed Enantioselective Reaction, *The Journal of organic chemistry* **75**, 7194–7201 (2010).

250. Katrina H Jensen and MatthewS. Sigman. Systematically Probing the Effect of Catalyst Acidity in a Hydrogen-Bond-Catalyzed Enantioselective Reaction, *Angewandte Chemie International Edition* **46**, 4748–4750 (2007).

251. Katharina M Lippert, Kira Hof, Dennis Gerbig, David Ley, Heike Hausmann, Sabine Guenther and Peter R Schreiner. Hydrogen-Bonding Thiourea Organocatalysts: The Privileged 3, 5-Bis (trifluoromethyl) phenyl Group, *European Journal of Organic Chemistry* **2012**, 5919–5927 (2012).

252. Robert R Knowles and Eric N Jacobsen. Attractive noncovalent interactions in asymmetric catalysis: Links between enzymes and small molecule catalysts, *Proceedings of the National Academy of Sciences* **107**, 20678–20685 (2010).

253. Alexander Wittkopp and Peter R Schreiner. Metal-Free, Noncovalent Catalysis of Diels–Alder Reactions by Neutral Hydrogen Bond Donors in Organic Solvents and in Water, *Chemistry-A European Journal* **9**, 407–414 (2003).

254. Gábor Tárkányi, Péter Király, Tibor Soós and Szilárd Varga. Active Conformation in Amine–Thiourea Bifunctional Organocatalysis Preformed by Catalyst Aggregation, *Chemistry-A European Journal* **18**, 1918–1922 (2012).

255. Lucie E Zimmer, Christof Sparr and Ryan Gilmour. Fluorine conformational effects in organocatalysis: an emerging strategy for molecular design, *Angewandte Chemie International Edition* **50**, 11860–11871 (2011).

256. Thomas Bürgi and Alfons Baiker. Conformational behavior of cinchonidine in different solvents: a combined NMR and ab initio investigation, *Journal of the American Chemical Society* **120**, 12920–12926 (1998).

257. Andrew G Schafer, Joshua M Wieting and Anita E Mattson. Silanediols: a new class of hydrogen bond donor catalysts, *Organic Letters* **13**, 5228–5231 (2011).

258. Yi-Fei Sheng, Qing Gu, An-Jiang Zhang and Shu-Li You. Chiral Bronsted Acid-Catalyzed Asymmetric Friedel- Crafts Alkylation of Pyrroles with Nitroolefins, *The Journal of Organic Chemistry* **74**, 6899–6901 (2009).

259. Madhu Ganesh and Daniel Seidel. Catalytic enantioselective additions of indoles to nitroalkenes, *Journal of the American Chemical Society* **130**, 16464–16465 (2008).

260. Junji Itoh, Kohei Fuchibe and Takahiko Akiyama. Chiral phosphoric acid catalyzed enantioselective Friedel–Crafts alkylation of indoles with nitroalkenes: cooperative effect of 3 Å molecular sieves, *Angewandte Chemie International Edition* **47**, 4016–4018 (2008).

261. Eimear M Fleming, Thomas McCabe and Stephen J Connon. Novel axially chiral bis-arylthiourea-based organocatalysts for asymmetric Friedel–Crafts type reactions, *Tetrahedron letters* **47**, 7037–7042 (2006).

262. Raquel P Herrera, Valentina Sgarzani, Luca Bernardi and Alfredo Ricci. Catalytic enantioselective Friedel–Crafts alkylation of indoles with nitroalkenes by using a simple thiourea organocatalyst, *Angewandte Chemie International Edition* **44**, 6576–6579 (2005).

263. Wei Zhuang, Rita G Hazell and Karl Anker Jørgensen. Enantioselective Friedel–Crafts type addition of indoles to nitro-olefins using a chiral hydrogen-bonding catalyst–synthesis of optically active tetrahydro-β-carbolines, *Organic & biomolecular chemistry* **3**, 2566–2571 (2005).

264. Gabriella Dessole, Raquel P Herrera and Alfredo Ricci. H-bonding organocatalysed Friedel-Crafts alkylation of aromatic and heteroaromatic systems with nitroolefins, *Synlett* **2004**, 2374–2378 (2004).

265. Noel PG Roeges. *A guide to the complete interpretation of infrared spectra of organic structures*. Wiley, (1994).

266. A. Hangan, A. Bodoki, L. Oprean, G. Alzuet, M. Liu-Gonzlez and J. Borrs. Synthesis, crystallographic and spectroscopic characterization and magnetic properties of dimer and monomer ternary copper(II) complexes with sulfonamide derivatives and 1,10-phenanthroline. Nuclease activity by the oxidative mechanism, *Polyhedron* **29**, 1305 – 1313 (2010).

267. Zahid H. Chohan, Moulay H. Youssoufi, Aliasghar Jarrahpour and Taibi Ben Hadda. Identification of antibacterial and antifungal pharmacophore sites for potent bacteria and fungi inhibition: Indolenyl sulfonamide derivatives, *European Journal of Medicinal Chemistry* **45**, 1189 – 1199 (2010).

268. Hamit Alyar, Arslan Ünal, Neslihan Özbek, Saliha Alyar and Nurcan Karacan. Conformational analysis, vibrational and NMR spectroscopic study of the methanesulfonamide-N, N-1, 2-ethanediylbis, *Spectrochimica Acta Part A: Molecular and Biomolecular Spectroscopy* **91**, 39–47 (2012).

269. Asha Chandran, Y Shyma Mary, Hema Tresa Varghese, C Yohannan Panicker, Pavel Pazdera and G Rajendran. FT-IR, FT-Raman spectroscopy and computational study of (E)-4-((anthracen-9-ylmethylene) amino)-N-carbamimidoylbenzene sulfonamide, *Spectrochimica Acta Part A: Molecular and Biomolecular Spectroscopy* **79**, 1584–1592 (2011).

270. Robert Silverstein and Francis Webster. *Spectrometric identification of organic compounds*. Wiley. com, (2006).

271. Y. Tanaka and Y. Tanaka. Infrared Absorption Spectra of Organic Sulfur Compounds. II. Studies on SN Stretching Bands of Methanesulfonamide Derivatives, *Chemical & pharmaceutical bulletin* **13**, 858–861 (1965).

272. Satoshi Kudoh, Masao Takayanagi, Munetaka Nakata, Takaaki Ishibashi and Mitsuo Tasumi. Infrared-induced rotational isomerization of 1, 2-ethanediamine in argon matrices and conformational analysis by DFT calculation, *Journal of molecular structure* **479**, 41–52 (1999).

273. Yu-lin Lam and HH Huang. Rotational isomerism in 1, 2-diaminoethane, 1, 2-bis (dimethylamino) ethane and 1, 2-bis (diethylamino) ethane, *Journal of molecular structure* **412**, 141–152 (1997).

274. Batista de LAE Carvalho, LE Lourenco and MPM Marques. Conformational study of 1, 2-diaminoethane by combined ab initio MO calculations and Raman spectroscopy, *Journal of molecular structure* **482**, 639–646 (1999).

275. C Baraldi, MC Gamberini, A Tinti, F Palazzoli and V Ferioli. Vibrational study of acetazolamide polymorphism, *Journal of Molecular Structure* **918**, 88–96 (2009).

276. C Meganathan, S Sebastian, I Sivanesan, Keun Woo Lee, Byoung Ryong Jeong, Halil Oturak, S Sudha and N Sundaraganesan. Structural, vibrational (FT-IR and FT-Raman) and UV–Vis spectral analysis of 1-phenyl-3-(1, 2, 3-thiadiazol-5-yl) urea by DFT method, *Spectrochimica Acta Part A: Molecular and Biomolecular Spectroscopy* **95**, 331–340 (2012).

277. Juan Ramón Avilés Moreno, Francisco Partal Ureña and Juan Jesús López González. Chiral terpenes in different matrices: R-(+)-camphor studied by IR-Raman-VCD spectroscopies and quantum chemical calculations, *Asian Journal of Speetroscopy* **14**, 1–21 (2010).

278. Juan Ramón Avilés Moreno, Francisco Partal Ureña and Juan Jesús López González. Chiral terpenes in different phases: R-(-)-camphorquinone studied by

IR–Raman–VCD spectroscopies and theoretical calculations, *Structural Chemistry* **22**, 67–76 (2011).

279. Andrea Ienco, Carlo Mealli, Paola Paoli, Nicolay Dodoff, Ziya Kantarci and Nurcan Karacan. Structure and vibrational spectroscopy of methanesulfonic acid hydrazide: an experimental and theoretical study, *New J. Chem.* **23**, 1253–1260 (1999).

280. Neslihan Özbek, Saliha Alyar and Nurcan Karacan. Experimental and theoretical studies on methanesulfonic acid 1-methylhydrazide: Antimicrobial activities of its sulfonyl hydrazone derivatives, *Journal of Molecular Structure* **938**, 48–53 (2009).

281. Alan E Reed, Larry A Curtiss and Frank Weinhold. Intermolecular interactions from a natural bond orbital, donor-acceptor viewpoint, *Chemical Reviews* **88**, 899–926 (1988).

282. Reeshemah N Allen, MK Shukla, Jaroslav V Burda and Jerzy Leszczynski. Theoretical study of interaction of urate with Li+, Na+, K+, Be2+, Mg2+, and Ca2+ metal cations, *The Journal of Physical Chemistry A* **110**, 6139–6144 (2006).

283. Gligor Jovanovski, Slavica Tančeva and Bojan Šoptrajanov. The SO2 stretching vibrations in some metal saccharinates: spectra-structure correlations, *Spectroscopy letters* **28**, 1095–1109 (1995).

284. Panče Naumov and Gligor Jovanovski. Vibrational study and spectra-structure correlations in ammonium saccharinate: comparison with the alkali saccharinates, *Spectrochimica Acta Part A: Molecular and Biomolecular Spectroscopy* **56**, 1305–1318 (2000).

285. Roy Dennington, Todd Keith and John Millam. GaussView Version 5. Semichem Inc. Shawnee Mission KS 2009.

286. Gligor Jovanovski and Bojan Šoptrajanov. Bonding of the carbonyl group in metal saccharinates: correlation with the infrared spectra, *Journal of Molecular Structure* **174**, 467–472 (1988).